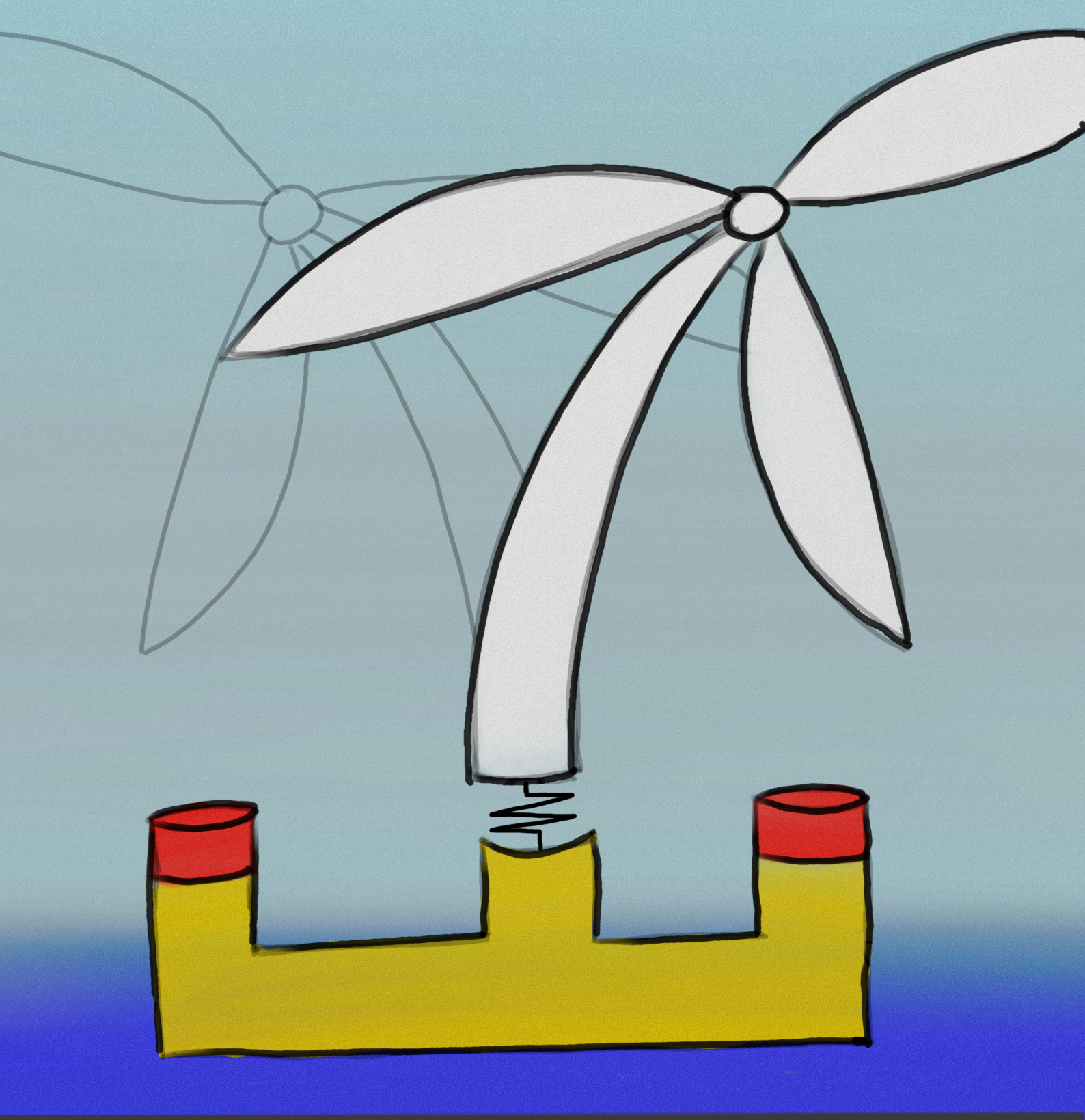

Improved Tower Structural Dynamics for a Floating Wind Turbine with a Rigid Substructure

Friedrich Jersch

July 29, 2025

NTNU
SIEMENS Gamesa RENEWABLE ENERGY
TU Delft

Offshore Wind Energy

Improved Tower Structural Dynamics for a Floating Wind Turbine with a Rigid Substructure

by

Friedrich Jersch

NTNU

123744

TU Delft

5920639

Supervisor NTNU:	M. Muskulus
Supervisor TU Delft:	O. Colomés
Supervisor Siemens Gamesa:	Q. Shen
Supervisor Siemens Gamesa:	E. Taub
Additional board examiner:	S. Watson
Additional board examiner:	W. Yu

NTNU SIEMENS Gamesa RENEWABLE ENERGY TU Delft

Abstract

Floating Offshore Wind Turbine (FOWT) unlock far-offshore wind resources in deep waters that can't be harvested under economic aspects using bottom-fixed wind turbines. Numerical modelling tools are employed to assess different FOWT designs under various environmental conditions. In order to be competitive and yet guarantee working designs, the numerical tools need to be reliable and computationally efficient. This justifies the need for assumptions simplifying the models.

One such simplification is the rigid floater assumption, where the FOWTs' substructure is assumed rigid. This reduces the computational effort but at the same time alters the results, like the tower's first natural frequency and corresponding mode shape.

Multiple approaches are used in literature to match the tower's first natural frequency of flexible and rigid floaters. This involves adjusting the tower properties, such as length or Young's modulus, or alternatively, implementing a flexible element between a rigid floater and a flexible tower. Siemens Gamesa currently makes use of the latter method by tuning the flexible elements' properties to achieve a match in the models' tower first bending natural frequency.

So far no studies have been conducted on the impact of the flexible element parameters on the tower first mode shape when tuning towards a matching tower first bending frequency. Additionally, the effect of differently correct mode shape variants on the tower dynamics is investigated. This leads to the goal of improving the tower dynamics for a FOWT with a rigid substructure.

The analysis was based on two versions of the U-Maine FOWT model. One fully flexible floater design served as a reference, whilst a fully rigid floater design was used to incorporate the different flexible element designs. Various flexible elements with distinct properties were evaluated to understand the sensitivity of the mode shape to these parameters. Subsequently, selected designs exhibiting varying degrees of accuracy of the mode shape were compared to the flexible floater design in time domain simulation. Furthermore, three separate methods of identifying the tower's first bending mode are proposed.

In the course of modelling the flexible floater design, a modelling error was made that resulted in double counting of the heave motions. Despite this error, it was concluded that for constant and turbulent wind, all flexible element designs outperform the rigid floater design. Furthermore, a close mode shape match likewise results in an increased match of bending moment and tower top rotation for high and low wind speeds. In the range of rated wind speeds, the shortest flexible element design with the worst mode shape match performs best. Comparing the tower top acceleration also indicates an overall improvement of the results, but less significant. This is expected to result from tuning towards the first tower mode rather than higher-order modes.

Generally, using any flexible element design already results in an improved mode shape match with minor differences. The impact of these discrepancies on the tower dynamics is small. Therefore, it is concluded that any flexible element, even when only tuned to match the tower's first natural frequency, is an improvement over the rigid floater design.

Contents

Figures

Tables

Acronyms

1P rotor passing frequency. 10, 12

3P blade passing frequency. 10, 12, 65, 67, 72, 114, 115

6P multiple of blade passing frequency. 10, 64, 67, 114, 115

BC Boundary Condition. 3, 4

CAD Computer-aided design. 23, 24

CAPEX Capital Expenditures. 1, 2

CoB Center of Buoyancy. 7–9, 20, 24, 25, 104

CoG Center of Gravity. 7–9, 20, 21, 24–26, 37, 42, 97, 104

DAF Dynamic Amplification Factor. 11

DLC Design Load Case. xi, xii, 45, 48, 70–73, 76, 78, 80, 85, 86, 119

DoF Degree of Freedom. vii, 4, 8, 9, 13, 16, 21, 22, 31, 34, 36, 40, 41, 97–100

EoM Equation of Motion. 10, 13

FEM Finite Element Methods. 3, 26

FOWT Floating Offshore Wind Turbine. iii, vii, 1–3, 6, 7, 10, 11, 15, 19–21, 28, 32, 39, 41, 43, 73, 82, 83, 87, 88

FRF Frequency Response Function. 11

LHS left-hand side. 10

MAC Mode Assurance Criterion. 13–15, 29, 30, 54–60, 63, 67, 69–72, 74–76, 78–80, 83, 85–87

MDOF Multiple Degrees of Freedom. 12

NTM Normal Turbulence Model. 46

OPEX Operational Expenditures. 1

PSD Power Spectral Density. 39, 47, 51, 63, 111, 112

RAO Response Amplitude Operator. vii, viii, 16, 20, 23, 34–38, 68

RNA Rotor-Nacelle Assembly. 79, 104

SDOF Single Degree of Freedom. vii, 10–12

SWL Sea Water Level. vii, 3, 4, 9, 25–29, 34, 37, 43, 82, 83, 99

TLP Tension Leg Platform. 6, 7

TSR Tip Speed Ratio. 12

Chapter 1

Introduction

1.1 Motivation

Wind energy is a key technology when it comes to reaching the goal of keeping the increase in global temperature, due to climate change, well below 2°C (IRENA, 2023). Offshore wind energy has numerous advantages over onshore wind energy that make it a crucial contributor to this goal. These advantages include stronger and more stable wind conditions, less visual and noise impact on the environment, and less limitation in the size of the components due to transportation bottlenecks (Backwell et al., 2024). The main limiting factor offshore wind energy is facing is limited amounts of available spots with favourable wind conditions in shallow water (Wu et al., 2019 and Cordle and Jonkman, 2011).

A prominent solution to this challenge are Floating Offshore Wind Turbine. The floating concepts allow for installation in deep waters without the need for an expensive substructure. Despite this advantage, Capital Expenditures (CAPEX) and Operational Expenditures (OPEX) are still high compared to offshore bottom-fixed wind turbines in shallow waters (Eriksen, 2022 and Wu et al., 2019). Increasing the turbine size, such as for the currently planned wind turbines in the range of 15 MW ('V236-15.0 MW™', 2024), lowers both, CAPEX and OPEX (Jahani et al., 2022). A further increase in size of up to 20 MW is expected by 2030 (Soares-Ramos et al., 2020). This increase in size comes with an increase in flexibility of the components, like the tower, blades and floater (Jahani et al., 2022).

Designs of FOWT are modelled under different environmental conditions and in different states using numerical simulation tools (Ran et al., 2023). For these simulations to be accurate, it is paramount to capture the dynamics of the FOWT correctly, as to avoid excitations (Liu and Ishihara, 2020). Additionally, to a high accuracy, computational time is an important factor since this is the driving factor for the cost. In order to reduce the simulation time, simplifications are made. One widely used assumption in the numerical modelling of FOWT is to model the floater as a rigid body (Sizova et al., 2022).

This simplification becomes more critical with increasing floater size and likewise increasing flexibility (Ran et al., 2023). Hence, the influence of floater flexibility on tower dynamics needs to be understood. Different studies investigated the impact of floater flexibility on the rigid body motions and also the impact on the tower natural frequency. Fewer studies have been performed on the influence of floater flexibility on the tower mode shape. The preliminary review of this thesis investigated this matter. Due to certain modelling errors, the results were being re-evaluated.

The further addition of this thesis is to look into the approach used by Siemens Gamesa of im-

plementing a flexible element between a rigid floater and a flexible floater to achieve a match in the first tower bending natural frequency. More specifically, the tower's first bending mode shape when using a flexible element with different parameters is investigated. Furthermore, the impact of a mismatch in the tower's first bending mode shape on the tower dynamics in a time domain simulation is examined. This is summarised in the research goal of **Improved Tower Structural Dynamics for a Floating Wind Turbine with a Rigid Substructure**.

Accomplishing this goal results in a more founded understanding of the accuracy and limitations when using the rigid floater assumption in combination with the flexible element. Higher trust in the results allows for more optimised designs, possibly saving material and hence saving CAPEX.

In advance to this thesis, a pre-thesis was written at NTNU. The goal of the pre-thesis was to gain a general understanding of the theory, through an extensive research review, and to perform analysis with the modelling software OrcaFlex to get more used to it.

A first modelling goal was to implement the flexible floater design successfully in OrcaFlex and already identify, as well as compare the tower first bending natural frequency between rigid and flexible floater. Results were found and discussed. However, due to modelling mistakes the results were reassessed and included as results in this thesis. Nevertheless, it must be noted that the main modelling of the flexible floater as explained in subsection 3.1.1 and subsection 3.1.3 was done in the pre-thesis. The further adjustments were performed in the course of the thesis.

Another objective of the pre-thesis was to define a general approach of identifying the tower's first bending mode shape of a FOWT using the *modal analysis* tool in OrcaFlex. This task was not completed, and will hence be addressed again in the thesis.

1.2 Literature Review

To establish a foundation for this study, existing research on the dynamics of FOWT, particularly the role of floater flexibility, is examined. Key findings from these studies are highlighted, with a focus on their implications for tower dynamics. This helps getting an overview of the topic, identifying gaps in the literature and defining clear research goals.

A general study on the influence of different boundary conditions for the tower of a FOWT is performed in Sizova et al., 2022. The results of a fixed tower show unsatisfactory results and show the need for a more realistic modelling approach. In the next step, the tower is connected to a steel cylinder with different Young's modulus configurations, which is clamped at the bottom. A change in natural frequency is seen, which indicates the impact of the local stiffness at the tower connection on the tower's first bending natural frequency.

Ran et al., 2023 investigates the hydroelastic response of a 10 MW spar wind turbine in the modelling tool SIMA. In this study four different models are compared. Two rigid floater cases and two flexible floater cases. Each floater design is once modelled with hydrodynamic loads captured through the Morison equation and, on the other hand, modelled with potential flow theory. One important assumption is that the Rotor-Nacelle Assembly (RNA) is considered rigid. The tower's first bending natural frequency for the flexible model was found to be 0.389 Hz compared to 0.4 Hz for the rigid floater design. This indicates an increase in the tower's first bending natural frequency when assuming the floater as rigid.

Similar findings are made in Iijima et al., 2016. A weakly coupled connection between DYNABEAM and FAST is used to model three different designs (rigid floater & rigid tower, flexible tower & rigid floater and flexible tower & flexible floater). The NREL 5 MW baseline wind turbine is used

on top of a spar floater. Again, an increase in the first tower natural bending frequency is found from 0.3125 Hz for the flexible case to 0.333 Hz for the rigid case.

Gao et al., 2024 performed a coupled numerical analysis of a TripleSpar semi-sub (10 MW DTU wind turbine) in OpenFAST. Three different models (fully rigid, flexible tower and rigid floater and fully flexible) are simulated in a decay test, as well as under environmental loads in operating conditions. An increase of 100 % tower top displacement was found when using the flexible floater design. Furthermore, the flexible floater design shows a 7 % increase in tower base bending when compared to the rigid floater design.

Yamaguchi et al., 2022 also identified an increase in tower first bending natural frequency from 0.665 Hz for a flexible floater design to 0.740 Hz when using a rigid floater design. The study was performed on the example of the 2 MW FOWT of the Fukushima Floating Offshore Demonstration Project. Two solutions are proposed to approach the mismatch in tower first bending natural frequency. The first one is to increase the tower length for the rigid floater design in order to lower the natural frequency. The second method alters the tower's Young's modulus using the following formula: $E_T = \frac{f^2_{Flexible}}{f^2_{Rigid}} \cdot E_0$, where E_0 is the original Young's modulus and $f^2_{Flexible}$ and f^2_{Rigid} are the tower's first bending natural frequency of the flexible floater design and the rigid floater design, respectively.

An extensive study on the influence of floater flexibility on the tower dynamics at the example of the DTU 10 MW wind turbine is performed using the Xue-10 semi-sub by Hsu, 2019. The flexible Finite Element Methods (FEM) model has two degrees of freedom per node (one translational and one rotational) and is simulated in Matlab. The required hydrodynamic properties are extracted from HydroD. In terms of the tower's first bending natural frequency, it was also found that the natural frequency for the rigid case (0.43 Hz) is higher than for the flexible case (0.36 Hz), matching the findings from the other studies of an increase in the tower's first bending natural frequency when using a rigid floater instead of a flexible one. The mode shapes were also investigated, and additional bending in the tower above Sea Water Level (SWL) was observed. Furthermore, the influence of the floaters' inertia on the first tower bending frequency is investigated.

Particular focus is put on Harger et al., 2023, as they use the 15 MW UMaine floater, which is also used in this thesis. Tower and floater are modelled using the FEM software ANSYS. Firstly, the influence of three different boundary conditions of the tower base, without a floater, are investigated. Using clamped-free Boundary Condition (BC) the tower's first bending frequency is the lowest with 0.304 Hz. Using a pined-free BC instead, increase the frequency to 0.883 Hz. An even higher first tower bending natural frequency of 1.02 Hz is achieved for the tower with a free-free BC. Clear differences are also identified in the mode shape for the different BCs. This indicates the impact of the choice of BC because of its influence on the tower's natural frequency and mode shape. The influence of the floater's inertia on the tower's first bending natural frequency is investigated by first neglecting the added mass and, furthermore, the floater's ballast. An increase of the frequency is observed in both cases, indicating the impact of floater mass on the system's behaviour. Furthermore, a shift in the mode shape of the tower's first mode is also observed. Both the mode shape and natural frequency shift from a pined-free case to a clamped-free case with increasing mass. Lastly, a comparison of the difference in tower first bending natural frequency and the corresponding mode shape between rigid floater and flexible floater design is done. Using a rigid floater over a flexible floater increases the tower's first bending natural frequency from 0.429 Hz to 0.462 Hz. The mode shape of the rigid floater includes more rotational and transverse displacement.

Li et al., 2023 also investigates the impact of floater flexibility on the global response of the 15 MW UMaine floater. The simulations are run in *SIMA*. Two different floaters are used: one fully

rigid floater and one floater with a flexible column, which consists of multiple nodes, each with 6 Degree of Freedom (DoF), connected by flexible beams. All the other components are assumed rigid, assuming that only the centre column influences the natural period of the tower bending mode. Furthermore, the struts connecting the centre and side columns above SWL are not considered. The rectangular pontoons connecting the centre and side columns below SWL are modelled cylindrical. It's also noted that the added mass and drag coefficient are adjusted in hindsight to match results from a benchmark floater model. Taking these assumptions into consideration, the main result of the study concerning this project work is that an increase in tower bending frequency was found when considering the tower as rigid (0.41 Hz) compared to the flexible floater (0.38 Hz).

The research review shows an increase in tower first bending natural frequency when using a rigid floater over a flexible one. This was found for all papers investigated. Furthermore, the impact on the mode shape was identified as showing more rotational and transverse motion when using a rigid floater. Using different BCs for the tower showed a change in the tower's first bending natural frequency and corresponding mode shape. The mass and added mass of the floater also show to have an influence on the tower's first bending natural frequency. An increase in mass results in a lower frequency and shift of the mode shaped towards a clamped-free BC.

1.3 Research Goal

The overall research goal addressed in this thesis is to achieve **Improved Tower Structural Dynamics for a Floating Wind Turbine with a Rigid Substructure**. This goal is divided into three phases. The first phase, Phase A, explains and discusses the setup of the two floater models. Phase B elaborates the strategy to create different flexible element designs. Lastly, Phase C clarifies the environmental conditions and results that are looked at. An overview of the research questions and plan on methods is provided in Figure 1.1.

1.3.1 Research Questions

Firstly, the different research questions are listed. They are mostly answered in chapter 4, except for two questions from Phase A that needed to be discussed in the course of building the floater models in order to achieve sufficient results.

Phase A: Flexible and Rigid Floater

A1 Question: Investigation of Added Mass in Modal Analysis.
A2 Question: Impact of Line Segmentation near SWL in OrcaFlex.
A3 Question: Compare Methods to Identify Tower Modes in the Multibody System Floating Offshore Wind Turbine.
A4 Question: Differences in Tower Natural Frequency between Fully Flexible Floater Model and Fully Rigid Floater Model.
A5 Question: Differences in Tower Mode Shape between Fully Flexible Floater Model and Fully Rigid Floater Model.

Phase B: Flexible Element Design Study

B1 Question: Influence of Flexible Element Length on the Tower Mode Shape.
B2 Question: Influence of Flexible Element Segmentation on the Tower Mode Shape.
B3 Question: Influence of Flexible Element Composition on the Tower Mode Shape.

Phase C: Effect of Tower Mode Shape Deviation

C1 Question: Influence of Tower Mode Shape Deviation on Decay Test.
C2 Question: Influence of Tower Mode Shape Deviation on Tower Bending.
C3 Question: Influence of Tower Mode Shape Deviation on Tower Acceleration.
C4 Question: Influence of Tower Mode Shape Deviation on Tower Top Rotation.

1.3.2 Research Methods

The research plan also contains the methods used in order to answer the research questions and hence follows the same phases.

Phase A: Flexible and Rigid Floater

A1 Method: Selection of a Rigid Floater Design.
A2 Method: Building a Flexible Floater in OrcaFlex.
A3 Method: Validation of Flexible Floater.
A4 Method: Floater Error Assessment.
A5 Method: Tower Mode Identification Method.

Phase B: Flexible Element Design Study

B1 Method: Implement the Flexible Element.
B2 Method: Create Variations of Designs.

Phase C: Effect of Tower Mode Shape Deviation

C1 Method: Design Load Cases.
C2 Method: Tower Dynamics.

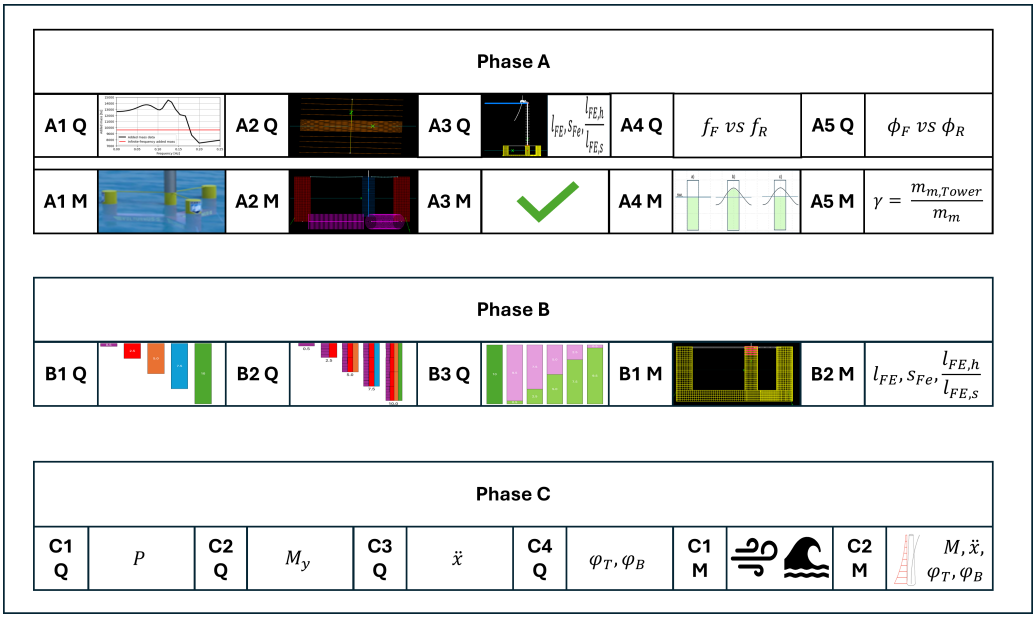

Figure 1.1: Research plan with three different phases (A, B, C) focusing on research questions (Q) and methods (M).

Chapter 2

Theoretical background

The following chapter covers the most important underlying theory applied in the thesis. First, an overview of FOWT designs is given in section 2.1 emphasising their different stability mechanisms. Following that, section 2.2 focuses on hydrostatic stiffness, and section 2.3 on the mooring line stiffness. The topic of added mass is covered in section 2.4, as it caused some difficulties in the pre-thesis during the modal analysis. Section 2.5 focuses on the dynamics of FOWT emphasising the importance of avoiding resonance, and is re-used from the pre-thesis. Subsequently, section 2.6 explains the topic of modal analysis in order to better understand how natural frequencies are identified. The decay test is introduced as an alternative to this in section 2.7. Lastly, some special aspects of OrcaFlex that are important for the project will be explained in section 2.8.

2.1 Different types of Floating Offshore Wind Turbines

FOWT are categorised into four different main designs, as illustrated in Figure 2.1. The barge floater design is characterised through a wide platform with a shallow draft. The SPAR typically has a long, cylindrically shaped floater. Semi-submersibles are characterised by having multiple floaters arranged with a certain distance to the tower connector. The Tension Leg Platform (TLP) is characterised through the use of tensioned mooring lines that pull down the floater.

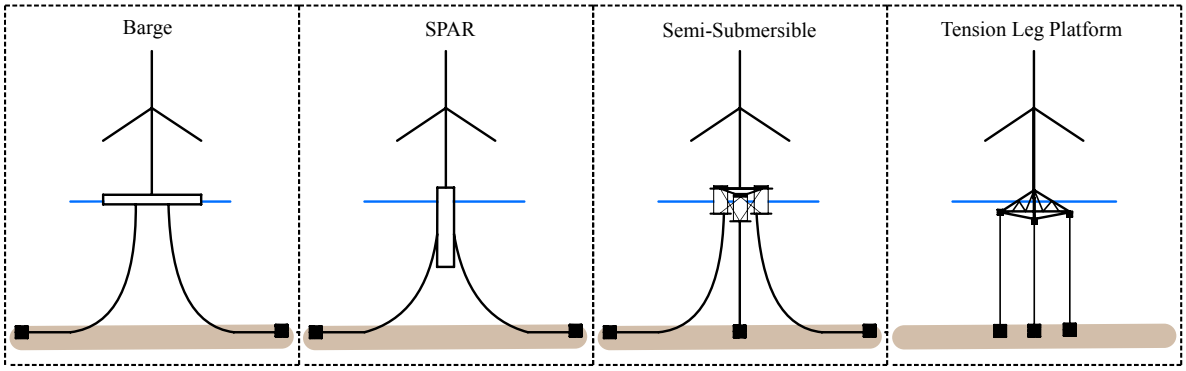

Figure 2.1: Four different main types of offshore platforms. *Source:* Adapted from Subbulakshmi et al., 2022, International Renewable Energy Agency (IRENA), 2016

All four floater designs generate stability through a combination of three main mechanisms. The stability triangle illustrated in Figure 2.2 presents each design's dependency on these stability mechanism.

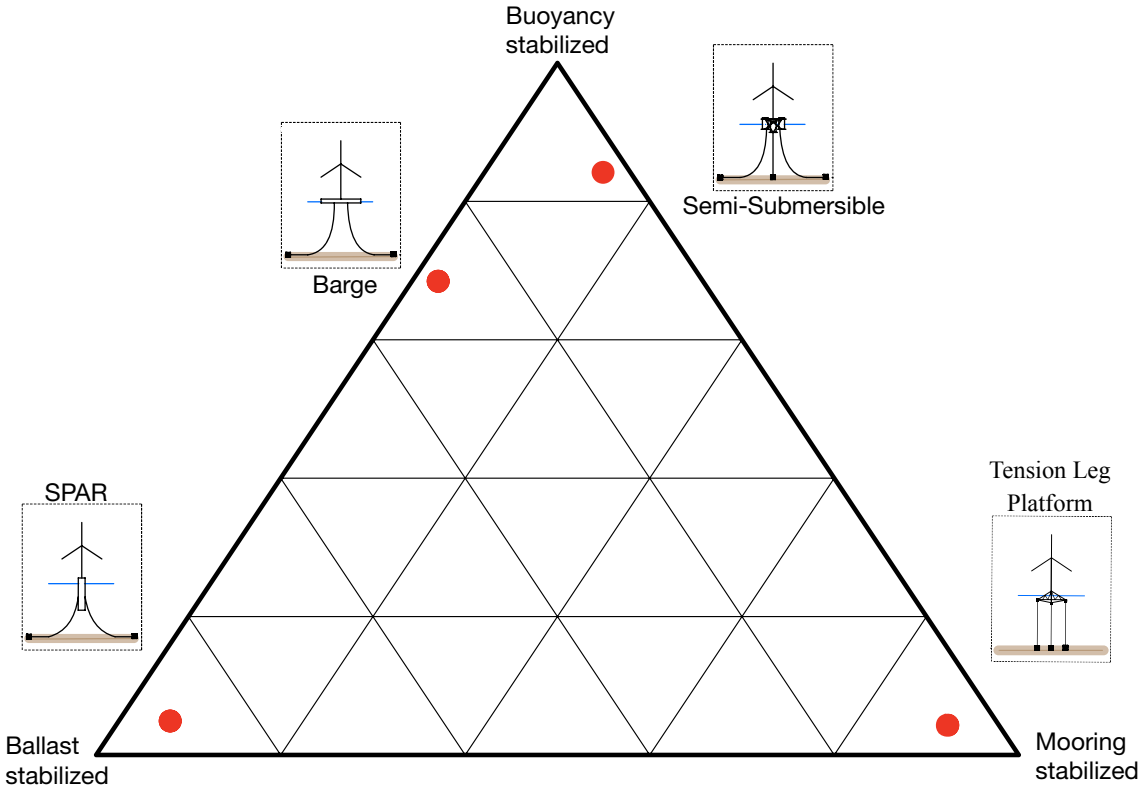

Figure 2.2: Stability triangle including four main designs of floaters. *Source:* Adapted from Subbulakshmi et al., 2022 and Borg and Collu, 2015

The three main mechanisms – ballast, buoyancy and mooring stabilised - are briefly explained with reference to Butterfield et al., 2007 and Leimeister, 2022:

- **Ballast:** Heavy ballast at the bottom of the floater is used to lower the Center of Gravity (CoG) below the Center of Buoyancy (CoB). This creates a counteracting moment to pitch and roll motions. Spar buoys depend on this stability criteria.
- **Buoyancy:** Semi-submersibles and barges depend on a big waterplane area as a restoring force. This is achieved by positioning one big or multiple small volumetric bodies away from the centre of the FOWT, creating a restoring force.
- **Mooring:** Mooring lines are used to generate stability by pulling down a big volume. The force generated through this achieves stability of the TLP designs.

The three mechanisms shown in Figure 2.2 make up the whole system stiffness ($\mathbf{K}$) of the rigid body. This can be broken down into two main categories: stiffness generated through hydrostatics ($\mathbf{K}_h$) and due to the mooring lines ($\mathbf{K}_m$). These two are explained in more detail in the following.

2.2 Hydrostatic stiffness

Hydrostatic stiffness describes the resistance of the floater against displacement due to changes in buoyancy forces acting to restore equilibrium in the heave, pitch and roll direction, as visualised in Figure 2.3a. The hydrostatic stiffness of the floater depends on the CoG, CoB, metacentric height and the size as well as the shape of the waterplane (Fossen, 2011).

In static position buoyancy and gravitational forces are in equilibrium. Enforcing a displacement in one of the three DoF heave, pitch, or roll results in a hydrostatic force. Setting the force in relation to the change in the respective displacement gives the stiffness of the floater against motion in that DoF when displaced in either heave, pitch, or roll (Al-Solihat and Nahon, 2014).

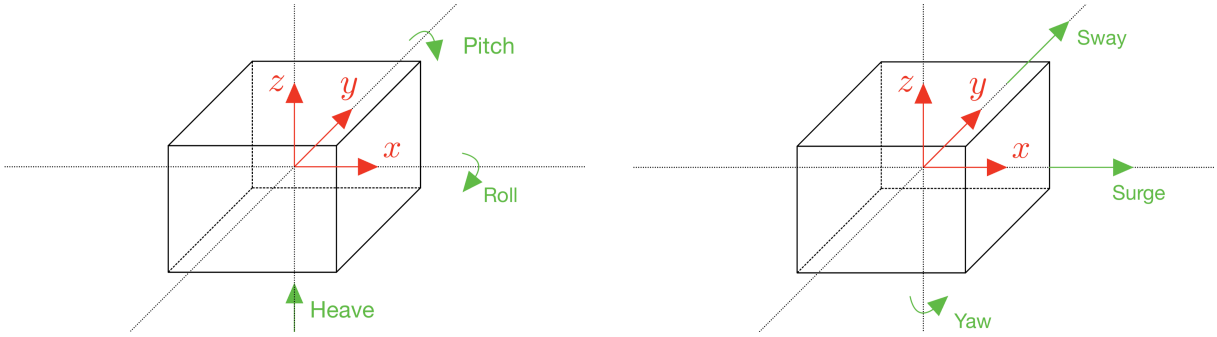

(a) Hydrostatic stiffness. **(b)** Mooring line stiffness.

Figure 2.3: DoF of a floating body and stiffness terms due to hydrostatic and mooring line stiffness.

The stiffness for each of these combinations can be described through a matrix, as shown in Equation 2.1. Small changes of displacement are assumed. This is a valid assumption, as the hydrostatic stiffness in this thesis is important around the static equilibrium position. Furthermore, the structure is assumed to be fully rigid (Al-Solihat and Nahon, 2014). The floater is symmetric in the fore-aft direction, leading to C_{43}, C_{34}, C_{53}, and C_{54} being zero (Jonkman, 2009). This yields Equation 2.1:

$$C = \begin{bmatrix} 0 & 0 & 0 & 0 & 0 & 0 \\ 0 & 0 & 0 & 0 & 0 & 0 \\ 0 & 0 & C_{33} & 0 & C_{35} & 0 \\ 0 & 0 & 0 & C_{44} & 0 & 0 \\ 0 & 0 & C_{53} & 0 & C_{55} & 0 \\ 0 & 0 & 0 & 0 & 0 & 0 \end{bmatrix} \tag{2.1}$$

, with

$$\begin{aligned} C_{33} &= \rho g A_c \\ C_{44} &= -Mgz_g + V\rho g z_b + \rho g I_{xx} + \rho g A_c y_f^2 \\ C_{55} &= -Mgz_g + V\rho g z_b + \rho g I_{yy} + \rho g A_c x_f^2 \\ C_{35} &= -\rho g A_c x_f \\ C_{35} &= -C_{53} \end{aligned}$$

This leads to the following conclusions:

- The heave restoring force depends on the floaters' cross-section at SWL (A_c).
- Roll and pitch restoring force depend on the position of the CoB (z_b), displaced volume (V), CoG (z_g), floater mass (M), second moment of area of the water plane area (I_{xx} or I_{yy}), and floaters cross-section at SWL (A_c).

The sign convention for the buoyancy and weight gives the wrong impression that buoyancy creates a stabilising term, whereas the weight is a destabilising term. This is resolved when including the sign of the position of CoG and CoB, which are typically negative.

2.3 Mooring line stiffness

The surge, sway and yaw motions do not gain their stability from the hydrostatic stiffness but through the mooring lines. These DoF are visualised in Figure 2.3b. There are two main types of mooring lines, catenary moorings and taut moorings (Brown, 2005).

Catenary mooring lines are typically heavy lines that generate restoring forces through the suspended weight of the line. In static equilibrium, part of the mooring line is resting on the seabed, whereas the other part is hanging in the water. In the case of a displacement in one of the horizontal directions (surge or sway), the mooring line end that is connected to the floater moves along with the floater. This results in two effects:

- Additional part of the mooring line lifts off, increasing the restoring force against the motion
- The angle at the connection point to the vessel flattens, increasing the amount of horizontal restoring force

These two effects cause the non-linear restoring forces of the floater against horizontal displacement.

Taut mooring systems, on the other hand, do not rely on the weight of the line but on the tension created through line stretch. Hence, lighter, more compliant material, such as fibre robes made of, for example, polyester, is used.

If the floating structure is displaced in one of the horizontal directions, the line is getting stretched. This increases the tension and hence the restoring force. Again, the angle between line and floater decreases, increasing the amount of horizontal restoring force. Due to this and the fact that the stiffness of synthetics is not constant, the restoring force is also not linear.

Next to these two types, the type of connection also influences the restoring forces of the platform. If the mooring lines are all connected at one point, a so-called single-point mooring system, the system can hardly create any restoring forces against yaw rotation. On the other hand, in the case of a spread mooring system, the mooring lines additionally generate a restoring force against yaw rotation.

The U-Maine floater has a spread mooring system with one mooring line connected at each of the side columns. This generates a yaw restoring force. With a catenary mooring line set-up, the suspended weight of the mooring lines limits horizontal displacement. The mooring lines also generate an additional restoring force in the other three rigid body motions: heave, pitch and roll (Al-Solihat and Nahon, 2014).

2.4 Added mass

Added mass describes the effect that a body moving in a fluid not only needs to accelerate its own mass but also the surrounding fluid. This effect was first reported by Bessel in 1828, who measured the period of a pendulum, once in air and in water. The observed increase in the period is due to the added mass of the system (Sarpkaya and Isaacson, 1982).

Equation 2.2 shows the Equation of Motion (EoM) of a simple SDOF system. The added mass acts in the opposite direction of the motion of the body, identical to the inertial mass (Benitz et al., 2015).

$$m\ddot{x} + b\dot{x} + cx = f(t) - m_a\ddot{x} \tag{2.2}$$

Bringing the added mass to the left-hand side (LHS) of the equation results in Equation 2.3

$$(m + m_a)\ddot{x} + b\dot{x} + cx = f(t) \tag{2.3}$$

As can be seen in Equation 2.4, this changes the natural frequency of the system by increasing the denominator and hence lowering the natural frequency.

$$\omega_n = \sqrt{\frac{k}{m + m_a}} \tag{2.4}$$

For a floating body like a FOWT the added mass acts due to the rigid body motions. In a case with no incident waves, the rigid body motions result in outgoing waves that create a fluid pressure on the body. Integrating these over the body surface yields forces and moments in the three translational directions and three rotational ones. These forces depend on added mass coefficients A_{kj} and damping coefficients B_{kj}. Faltinsen, 1999 gives an extensive overview on how to calculate them theoretically. The most important properties to remember are that the added mass coefficients are functions of the speed of the body, the body's shape and the frequency of oscillation. The influence of the frequency dependency of the added mass coefficients is investigated in section 3.2.

2.5 Dynamics of FOWT

FOWT, as well as bottom-fixed offshore wind turbines, are subject to many different loads. These contain external excitation like wind and wave forces but also structural loads that need to be avoided, and hence well understood. The environmental loads are captured through a frequency range that indicates what frequencies need to be avoided. The for the tower important structural loads act at the rotor passing frequency (1P) and the blade passing frequency (3P), as well as harmonics of the blade passing frequency (6P, 9p). They all depend on the rotor speed of the wind turbine, which varies across different turbine models. Furthermore, modern wind turbines operate in a range of rotor speeds ($\omega_{cut-in} < \omega < \omega_{cut-out}$).

Figure 2.4a shows the 1P and 3P range together with the Pierson–Moskowitz wave and Kaimal wind spectrum. An additional safety margin of ±10% is accounted for around the 1P and 3P frequencies. Furthermore, the tower first bending natural frequencies is indicated outside the excitation ranges.

The importance of avoiding these frequencies and hence resonance is best explained at the example of a SDOF-mass-spring-damper. A detailed explanation of the findings is provided in Van Der

Tempel and Molenaar, 2002. The most important takeaway is the influence of the Dynamic Amplification Factor (DAF) on the static response. An example Frequency Response Function (FRF) showing the DAF, but omitting the phase shift is illustrated in Figure 2.4b. Several key concepts are briefly discussed below.

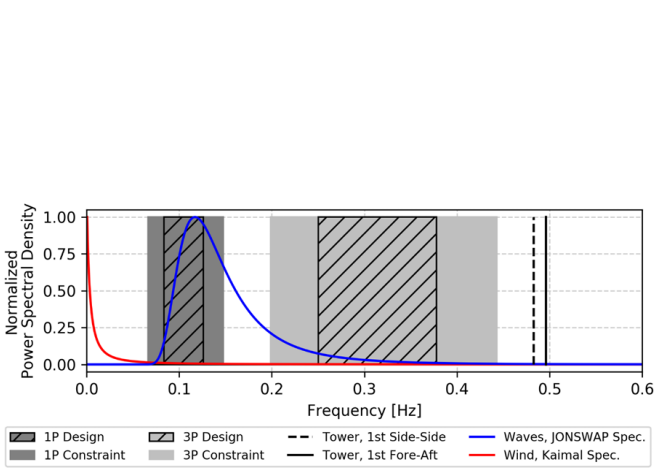

(a) UMaine 15 MW power spectrum of main excitations, taken from Allen et al., 2020.

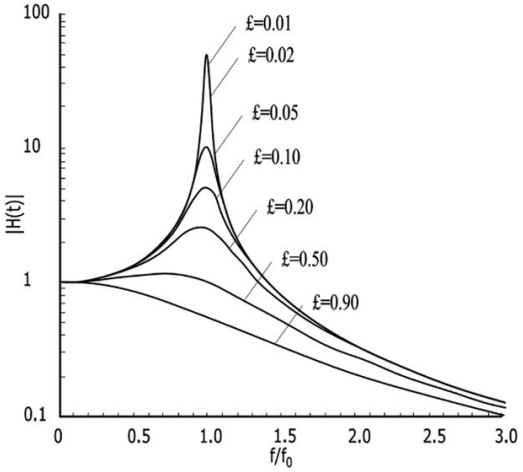

(b) DAF of a SDOF-mass-spring-damper system for different damping ratios (Kiriparan et al., 2021).

Figure 2.4: Power spectrum of main excitations for UMaine 15 MW turbine and dynamic amplification factor for an Single Degree of Freedom (SDOF)-system.

Most importantly, the DAF relates the amplitude of the force to different frequencies of the excitation force. The x-axis represents the ratio between the excitation force frequency and the system's natural frequency, denoted as $\beta = f/f_n$, where f_n is the natural frequency. The y-axis captures the amplitude of the force as a ratio of the amplitude of the force over the amplitude of the static response. The different curves indicate different damping ratios, which shall be ignored for now. Figure 2.4b can be split into three different main regions:

- $\beta << 1$: The system's response is quasi-static, following the force as if it were static.
- $\beta \approx 1$: The motion gets significantly amplified; the spring force and inertia force almost cancel.
- $\beta >> 1$: Almost no response because the system cannot follow the high frequency.

A second observation is that more damping helps to lower the amplitude of the response. It is thus important to include damping in a system. However, the amount of damping is next to technical challenges limited by the budget. The typical damping for a bottom fixed wind turbine was found to be between 1% and 4% for side-to-side and between 2% and 8% for fore-aft direction in operating conditions (Arany et al., 2016). The difference is due to the aerodynamic damping of the rotor when rotating. For a FOWT similar damping can be assumed. However, even with damping included, the DAF can still amplify the response significantly. This shows the importance of avoiding resonance between excitation force and natural frequency.

In the case of FOWT the frequency, the forces are known (see Figure 2.4a) but they can't be changed. Thus, the natural frequency of the structure must be placed such that it doesn't coincide with the frequency of the excitation forces.

Three different tower design regions can be defined in Figure 2.4a. They are "soft-soft", which

includes frequencies below 1P but above the wind spectrum; "soft-stiff" for tower designs with a tower first bending natural frequency between 1P and 3P but outside the wave spectrum; and lastly, "stiff-stiff", which is located above 3P.

The natural frequency is varied by changing the amount of steel used, which changes the tower stiffness. More material, for example, by having a wider diameter or thicker walls, increases the stiffness. At first glance, the easiest approach would be to adopt a stiff-stiff tower design by increasing the natural frequency to place it well above the excitation frequencies. However, this will be more expensive, as more steel is required. Hence, a design that uses as little steel as possible would be the goal (Van Der Tempel and Molenaar, 2002).

The soft-soft design involves very low tower stiffness. The tower is compliant with the excitation loads by having a natural frequency that is lower than the excitation frequencies from rotor and wave (still above wind). Even though this would be the cheapest option, it is in general too flexible and can be excited by the waves (Harger et al., 2023). Moreover, the increasing size of wind turbines and rotor blades shifts the 1P regime towards lower frequencies, complicating the soft-soft design. This occurs because wind turbines have an optimal Tip Speed Ratio (TSR) of roughly 8, which maximises the power coefficient. With increasing blade size, the only way to keep the TSR at this value is by reducing the rotor speed (Van Der Tempel and Molenaar, 2002).

Lastly, the soft-stiff design positions the tower's natural frequency between the 1P and 3P regions. However, it's challenging to match the gap between 1P and 3P. In addition, wind turbines with a wider range of rotor speeds either have a very small gap or no gap at all (Areva M5000 5 MW) (Arany et al., 2016). A modern approach to this problem is to design the pitch controller so that the rotor speed that matches the natural frequency is skipped intentionally. This way excitation is prevented. While this is feasible, the jump in rotational speed causes additional costs regarding power production and maintenance (Arany et al., 2016).

Depending on the rotor speed and wave spectrum, a stiff-stiff tower design can be the best choice. No matter which region is aimed for, a reliable method to predict the tower's natural frequency is needed. Such a method is the modal analysis.

2.6 Modal analysis

Modal analysis is used to identify how a structure vibrates, yielding results such as the natural frequencies, mode shapes and the mode participation factor. These parameters are crucial for predicting the tower's response to dynamic excitations and are applied during the preliminary design phase to:

- Identify the natural frequency of the system to assess potential resonance issues.
- Analyse the mode shape of the system to detect regions of high deformation or stress.

In addition to preliminary design, the results from modal analysis can be used for modal superposition. Modal superposition allows handling the response of each mode individually and treating them like SDOF-systems. These are easy and fast to solve. Additionally, only the most important modes need to be considered. These include modes with either a high participation factor or a natural frequency close to the frequency of the forces. This way the number of equations to be solved is reduced and the computation time further decreased. However, this method only applies to linear systems.

For a Multiple Degrees of Freedom (MDOF) system, the equation of motion is written as:

$$\mathbf{M}\ddot{x} + \mathbf{C}\dot{x} + \mathbf{K}x = f(t) \tag{2.5}$$

Assuming sinusoidal motion, as well as an unforced, undamped case, the EoM reduces to

$$\left(-\mathbf{M}\omega^2 + \mathbf{K}\right)\phi = 0 \tag{2.6}$$

This gives us an eigenvalue problem that can be solved by the computer for the eigenfrequencies (ω) and mode shape vectors (ϕ). There are as many eigenfrequencies as there are DoF. For each of the natural frequencies, a mode shape vector is found that characterises the motion of the tower for that frequency. The vectors are normalised with the max displacement of each mode.

2.6.1 Modal mass and modal stiffness

Additionally, to the mode shape vector and eigenfrequencies, one can furthermore identify the modal mass and likewise the modal stiffness. Both are characteristic for a single mode and determined using Equation 2.7 and Equation 2.8.

$$m_i = \boldsymbol{\phi_i}^T \boldsymbol{M} \boldsymbol{\phi_i} \tag{2.7}$$

$$k_i = \boldsymbol{\phi_i}^T \boldsymbol{K} \boldsymbol{\phi_i} \tag{2.8}$$

With $\boldsymbol{M}$ and $\boldsymbol{K}$ as the system mass and stiffness matrix and i as an indicator for the mode. $\boldsymbol{\phi_i}$ represents the mode shape vector of that mode.

The modal mass determines how much mass is participating at that certain mode. The modal mass and modal stiffness are in the relation that Equation 2.9 yields the natural frequency of that mode.

$$\omega_i = \sqrt{\frac{k_i}{m_i}} \tag{2.9}$$

2.6.2 Modal assurance criterion

Additionally, to subjectively comparing the shape of two modes, a reliable method is required that quantitatively compares two modes. This is achieved by the Mode Assurance Criterion (MAC). The Mode Assurance Criterion compares two different mode shapes with each other and is typically used between analytical and experimental results. It can also be used between two analytical mode shapes. The equation for the MAC is shown in Equation 2.10, with mode shape vectors φ_A and φ_X for different modes r and q (Pastor et al., 2012).

$$MAC(r,q) = \frac{\left|\{\varphi_A\}_r^T \{\varphi_X\}_q\right|^2}{\left(\{\varphi_A\}_r^T \{\varphi_A\}_r\right)\left(\{\varphi_X\}_q^T \{\varphi_X\}_q\right)} \tag{2.10}$$

The result is a number between 0 and 1. A value of 0 stands for no similarity, whereas a value of 1 represents full similarity.

Typically, multiple mode shapes of two models are compared to each other, yielding a matrix of MAC values. In the case of the thesis, the MAC is only applied between selected modes that have been defined as tower bending modes. Hence, no matrix is available, but only a final value that quantifies the similarity between the two mode shapes.

In order to get a better understanding of the range of MAC numbers and the visual difference in mode shape five different functions are created and compared. The reference version has the simple function of:

$$f(y) = 0.1 \cdot y^2 \tag{2.11}$$

The other four functions are variations of this, changing the exponent of power, adding a a-axis and y-axis shift and lastly a rotation at the root. Table 2.1 states the function of each case and the corresponding MAC number when compared to the reference case. Furthermore, Figure 2.5 shows the five different cases for a visual interpretation.

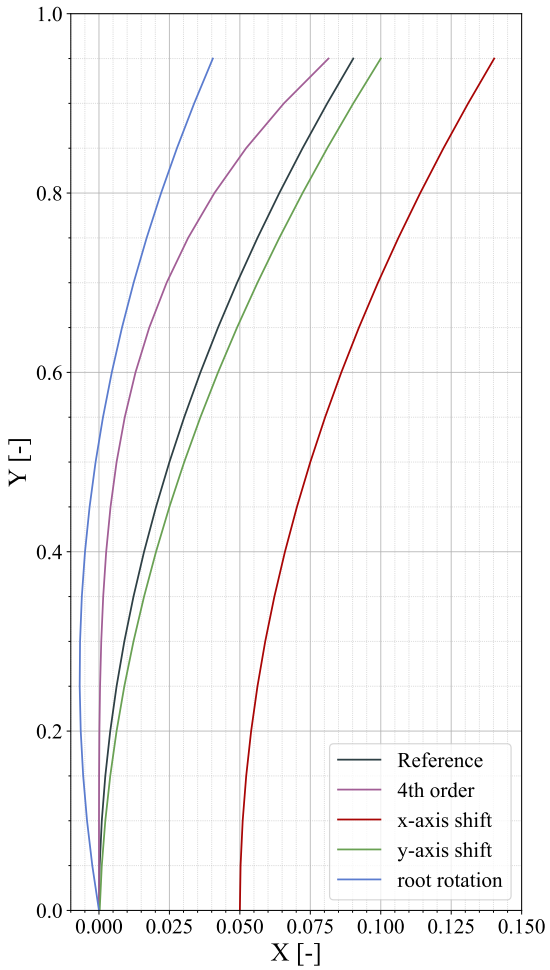

Figure 2.5: Visualisation of different functions. All variations of the reference case with $f(y) = 0.1 \cdot y^2$.

Table 2.1: Modal assurance criterion number between the different functions visualised in the figure above and the reference case.

Name	**Function**	MAC
reference	$0.1 \cdot y^2$	–
exponent	$0.1 \cdot y^4$	0.919
x-axis	$0.1 \cdot y^2 + 0.05$	0.844
y-axis	$0.1 \cdot y_{shift}^2$	0.999
root rotation	$0.1 \cdot y^2 \cdot \cos(0.052) - y \cdot \sin(0.052)$	0.781

2.7 Decay test

A decay test can be either performed numerically or experimentally. In both cases the setup and goal are the same: The structure of interest is given an initial displacement or velocity. After releasing the structure, it will oscillate its equilibrium position. For a damped system the oscillation will decrease and eventually die out. Observing the time series of this oscillation can give important insight on the natural frequency and damping of the system.

The natural frequency can be simply found by measuring the period of the characteristic variable.

The damping can occur due to different sources. In case of a FOWT structural damping, aerodynamic damping of the blades as well as hydrodynamic damping are possible. Depending on the type of damping, the damping process behaves either linearly or non-linearly. For linear damping the logarithmic decrement can be used to find the damping ratio. The logarithmic decrement is found by comparing the amplitude of two points with n as the amount of full periods in between. In the case of non-linear damping, on the other hand, as for example quadratic damping due to drag from hydrodynamic damping, one can use the PQ method. More information on this can be found in Bachynski-Polic, 2021 and Muskulus, 2023.

2.8 OrcaFlex

OrcaFlex is a software tool used for the dynamic and static simulation of offshore structures. It is capable of performing analysis on riser systems, mooring systems, towed systems but also FOWT. Users can individually alter the environmental conditions. Models in OrcaFlex are built using modular objects. The available objects have different modelling capabilities that are explained in subsection 2.8.1.

2.8.1 OrcaFlex objects

For the modelling of a wind turbine, the following five objects are used: *line*, *turbine*, *6D buoys*, *3D buoys*, and *vessel*. The important simulation characteristics are quickly summarised. A more detailed description of each of the objects can be found under: OrcaFlex Help.

The line element is used to model the mooring lines, tower and floater (if flexibility of the floater is considered). Its most important characteristic is that it is flexible since it is the only object in *OrcaFlex* with that property. Length, connection points, material properties like density, stiffness, inner/outer diameter, and hydrodynamic properties can be specified. A finite element approach is chosen where the lines are divided into a number of massless line segments. Mass, buoyancy, and weight are lumped

to the nodes, which are positioned between the segments, as visualised in 2.6a. The segments account for axial and torsional properties of the line. It is important that these properties do not have to be symmetric. The use of *line types* enables changes to the line's structural properties along the line length. The bending stiffness of the line element is included by rotating spring dampers at either side of the node, as shown in Figure 2.6b. No Hermite shape functions are used to capture the deformation of the line segments. Hence, each segment, for itself, is a straight line.

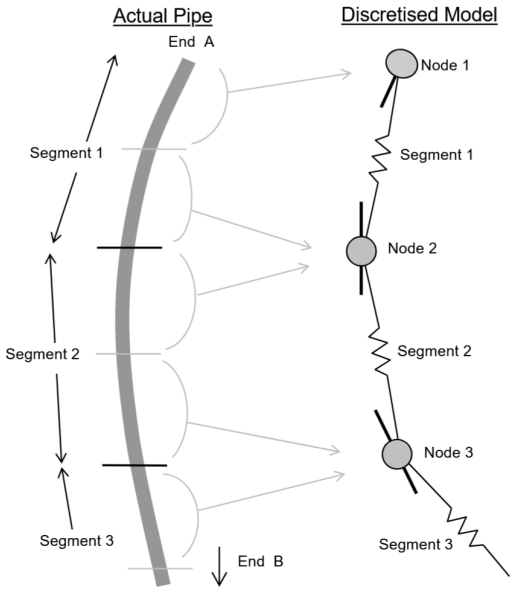

(a) OrcaFlex line element with segments and nodes.

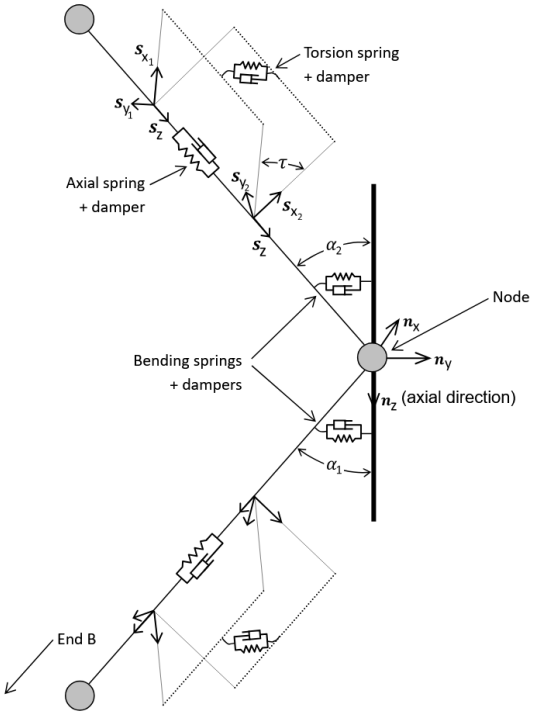

(b) Bending properties of a *line* in OrcaFlex.

Figure 2.6: Illustration of line modelling in OrcaFlex.

The *turbine* object is used to model the wind turbine's aerodynamic behaviour, so in operating conditions but also to account for the blade flexibility, which is modelled similar to a *line*.

6D buoys and *3D buoys* can be freely chosen to have any value of volume and mass and can thus be used as either point mass, massless volume or a combination of the two. The 3D buoy has only the three translation degrees of freedom. On the other hand, the 6D buoy includes all 6 DoF. It furthermore allows for the application of wave loads through the Morison equation and an accurate calculation of the submerged volume as well as water plane area.

The *vessel* object can be used for many different cases. Its main usage for this project is its capability to import Response Amplitude Operator (RAO)s and added mass and damping properties from a diffraction analysis tool. However, the *vessel* is a rigid body and thus does not account for flexibility.

2.8.2 OrcaFlex *modal analysis*

OrcaFlex operates in multiple simulation stages. The static analysis is used to establish a stable initial condition for the model. With the static simulation finished, one can perform a *dynamic analysis*, *fatigue analysis* or *modal analysis*.

The *modal analysis* is used for this project to identify the tower mode shapes. It performs a modal analysis for the whole system by combining the stiffness and mass matrix of all objects, including coupling terms where needed. Utilising these two matrices, the eigenvalue problem is solved according to the theory explained in section 2.6. The results can be visualised in 3D, where each mode shape can be visualised, vibrating at its corresponding natural frequency. This is done for a specified number of modes. The shown modes are system modes. Hence, an approach on how the mode shapes are identified is explained in subsection 3.1.6.

2.8.3 OrcaFlex Python interface

OrcaFlex simulations can be set up using Python using the OrcaFlex API. This way models can be created, parameters of certain objects changed, and environmental conditions altered, all through Python. In Python *for loops*, *while loops* and *if statements* can be implemented in the code. The big advantage is that it allows for the automation of certain steps. It is, for example, possible to change the stiffness of certain parameters based on the results of a previous simulation, without the need to look at the results manually.

Additionally, the OrcaFlex API allows easy extraction of results, which makes post-processing in Python faster and more efficient. The OrcaFlex API has no intuitive syntax, but clear documentation of the commands and syntax is provided under OrcaFlex API.

Chapter 3

Methodology

The methodology chapter mainly focuses on the methods used to answer the research questions. However, some research questions need to be answered in the process before advancing to the next steps. This includes, for example, a study on the impact of added mass in the OrcaFlex *modal analysis* tool, which needs to be understood in order to generate a correct flexible floater design. Figure 3.1 summarises the research plan and research questions that are discussed in the following chapter.

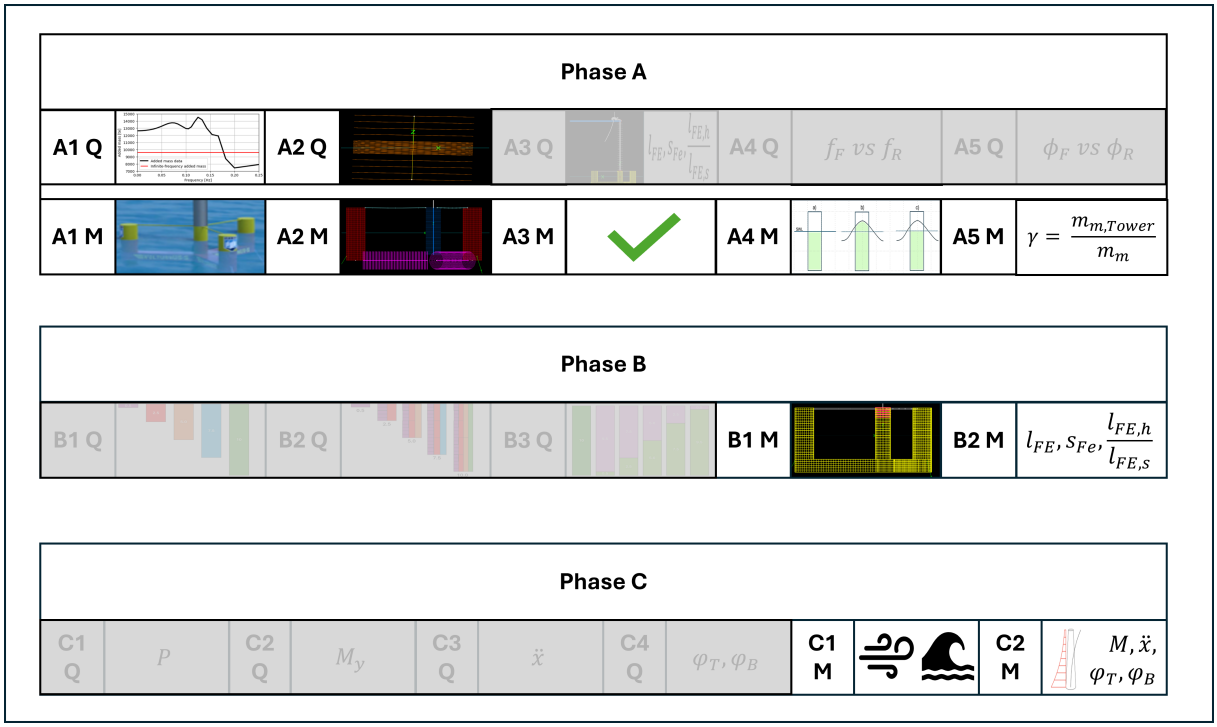

Figure 3.1: Overview highlighting the research plan for this chapter. Grey highlighted questions are discussed in chapter 4.

3.1 Phase A: Flexible and Rigid Floater

Phase A aims to explain the preparatory. The first step of the research methods is the **Selection of a Rigid Floater Design** (**A1 M**). This is done in subsection 3.1.1, which additionally describes how the floater is modelled in OrcaFlex. The rigid floater model is used to answer the first research question, **A1 Q**, an additional study on the **Investigation of Added Mass in Modal Analysis**. Following the process of **Building a Flexible Floater in OrcaFlex** (**A2 M**) is explained in subsection 3.1.3. This process encountered an unexpected sensitivity of the rigid body motions to the line segmentation near SWL. Hence, a second additional study is performed in subsection 3.1.4. This answers the next research question, **A2 Q**, on the **Impact of Line Segmentation near SWL in OrcaFlex**. After this study, the next step is the **Validation of Flexible Floater** (**A3 M**) in subsection 3.1.5. In the following, an error sensitivity is performed since, in the process of analysing the results, some unexpected results have been found. Changing the model and rerunning everything was not possible in the scope of this work. Hence, the error and its impact on the result, as well as its cause and possible mitigations, are explained in subsection 3.1.6 on the **Floater Error Assessment (A4 M)**. Lastly, three different general approaches on how to **Define a Tower Mode Identification Method** (**A5 M**) are explained. This includes a decay test setup in the time domain, a modal analysis approach in the frequency domain, and the use of a simplified floater model.

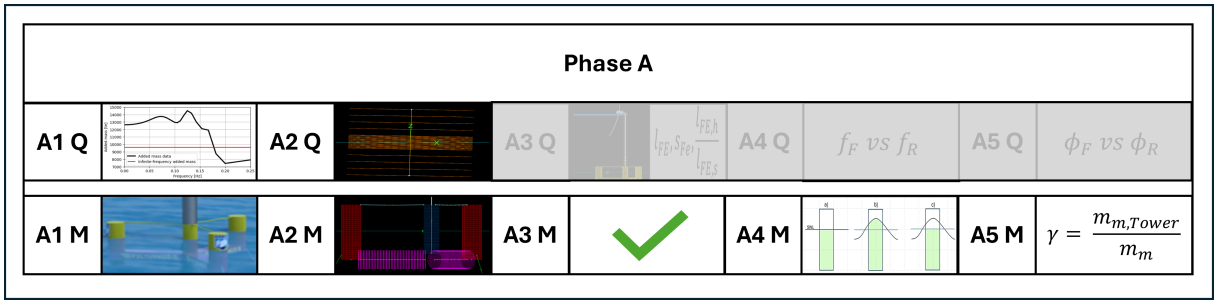

Figure 3.2: Overview highlighting the research plan for this section. Grey highlighted questions are discussed in chapter 4.

3.1.1 Selection of a Rigid Floater Design (A1 M)

Orcina provides some examples of models that can directly be used in OrcaFlex. One such model is the U-Maine 15 MW model, a semi-submersible floater with a 15 MW FOWT mounted on top (Allen et al., 2020). This is the same floater that was already used in the pre-thesis. Hence, the description of the floater is reused.

The system gains stability from three side columns with constant ballast at the bottom. The side columns are connected to a centre column via steel arms that are filled with seawater. In addition to the arms, struts are used to connect the centre and side columns above the waterline. The tower is mounted on the centre column, with the 15 MW reference wind turbine version 1.1.3 on top (Gaertner et al., 2020). A catenary mooring system is used that adds additional stability, as explained in section 2.3.

The most important structural parameters of the floater as well as a sketch of the FOWT are shown in Figure 3.3. A more detailed description of the system is provided in Allen et al., 2020.

In addition to the floater properties, the natural frequency of the rigid body motions and the fore-aft tower bending are reported. It should be noted that no clear indication is given in the paper

whether the floater was assumed to be rigid or flexible. Since the connection between floater and tower was assumed rigid, it is concluded that a rigid floater was assumed in Allen et al., 2020. The natural tower frequency in Allen et al., 2020 is reported as 0.496 Hz. However, the FAQ of the GitHub repository (IEA Wind Task 37 GitHub) mentions that "In simulation in both OpenFAST and HAWC2, the first natural frequency of the floating tower is closer to 0.4 Hz", and that "The set of modelling tools used to estimate that frequency and drive the tower design was found to have an error." Hence, the tower's first bending natural frequency in fore-aft in Allen et al., 2020 was not used as a reference.

Table 3.1: Parameters of 15 MW wind turbine, according to Allen et al., 2020.

Variable	Value	Unit
Intrinsic properties		
E_{steel}	200×10^9	Pa
S_{Steel}	79.3×10^9	Pa
Geometry		
m_{total}	$17,854 \times 10^3$	kg
m_{steel}	$3,914 \times 10^3$	kg
$m_{seawater\ ballast}$	$11,300 \times 10^3$	kg
$m_{ballast}$	$2,540 \times 10^3$	kg
m_{point}	100×10^3	kg
V_{hull}	20,206	m^3
CoG	-14.94	m
CoB	-13.63	m
I_{roll}	12.51×10^9	kgm^2
I_{pitch}	12.51×10^9	kgm^2
I_{yaw}	23.67×10^9	kgm^2
Natural frequency		
Surge	0.007	Hz
Sway	0.007	Hz
Heave	0.049	Hz
Pitch	0.036	Hz
Roll	0.036	Hz
Yaw	0.011	Hz
Tower bending	0.496	Hz

Figure 3.3: Sketch of the 15 MW FOWT from Allen et al., 2020.

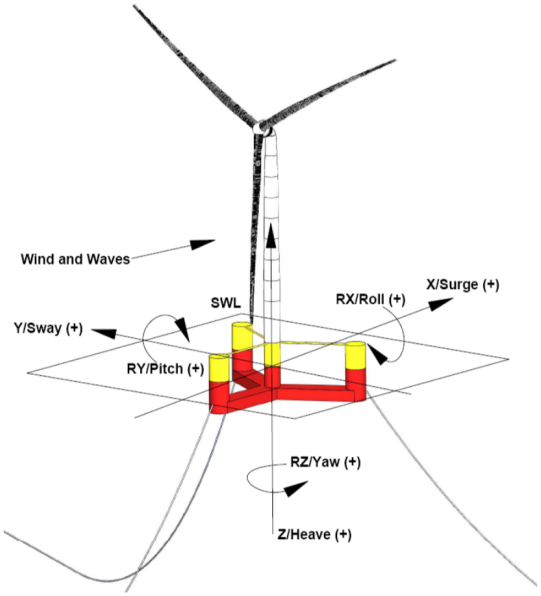

The rigid floater was modelled as a *vessel object* in OrcaFlex. This *object* contains the moment of inertia, CoG and a specific *vessel type*. The *vessel type* contains information about the submerged volume, CoB, RAO's, added mass and hydrostatic stiffness. These properties were calculated in OrcaWave using a mesh of the floater.

In order to have two identical floaters, with only the stiffness being different, all these parameters need to be identical. As a preparation for the thesis, the pre-thesis already aimed to build a correct model. However, mismatches and errors were identified in these models. Whilst most of these were resolved by reworking the flexible floater in subsection 3.1.3, the moment of inertia proved to be

difficult to change. The position, total mass and density distribution of the single components need to be changed in order to alter the moment of inertia, whilst maintaining total mass and CoG. Changing the moment of inertia of the rigid floater, on the other hand, is a simpler task. As the goal of the thesis is not to have an accurate flexible model of the U-Maine floater but to have two FOWT models that only differ in floater flexibility, it was decided to adjust the rigid floater's moment of inertia to the value of the moment of inertia of the flexible floater.

In a first step the compound properties were used to calculate the moment of inertia and CoG of the flexible floater according to the centre of origin. The superstructure also influences the behaviour of the floater and thus had to be included in the OrcaWave calculation. The results from OrcaWave were then imported into OrcaFlex and used as input for the *vessel type* that represents the rigid floater.

The superstructure is now included in the *vessel type* through the OrcaWave calculation. Additionally, the superstructure is modelled in OrcaFlex. This would result in counting it twice. Hence, the superstructure's mass, CoG and moment of inertia were subtracted from the *vessel type* using the inertia compensation property.

3.1.2 Investigation of Added Mass in Modal Analysis (A1 Q)

The previous work used the built-in *modal analysis* tool from OrcaFlex to investigate the tower bending modes modes and rigid body motions. However, the results were different from the reference values, even for the rigid model which is provided as an OrcaFlex example. It was concluded that the *modal analysis* tool was understood wrong. Thus, this additional study was performed right at the beginning of the thesis to gain a better understanding of the *modal analysis* tool. This is crucial for the model validation and later work, which requires a sound understanding of the *modal analysis* tool.

The *modal analysis* tool works in the frequency domain, not allowing for frequency-dependent added mass. The OrcaFlex documentation states that "added mass is [...] neglected in modal analysis if the data are frequency dependent" and a constant added mass matrix is chosen instead. Two different assumptions were tested, and the results compared to the reference results from Allen et al., 2020.

Firstly, the infinite added mass was used as the constant added mass matrix. The infinite added mass is reported in OrcaFlex individually for each combination of DoF and describes the value of added mass in the case of an infinitely high frequency. Figure 3.4 shows the frequency-dependent added mass as a full curve and the infinite added mass as the dashed horizontal line. The rigid body motion frequencies when using this assumption are reported in Table 3.2.

In a second approach, the added mass value for each combination of DoF was found by utilising the fact that the correct frequency of the rigid body motions was already known via the reference values. For surge this is, for example, 0.007 Hz. The added mass value for $\mathbf{A}_{11}$ for example, was simply read off the curve from Figure 3.4 at a value of 0.007 Hz and then used as an input to the added mass matrix. This was repeated for all the other entries of the added mass matrix. The resulting rigid body motions are reported in Table 3.2.

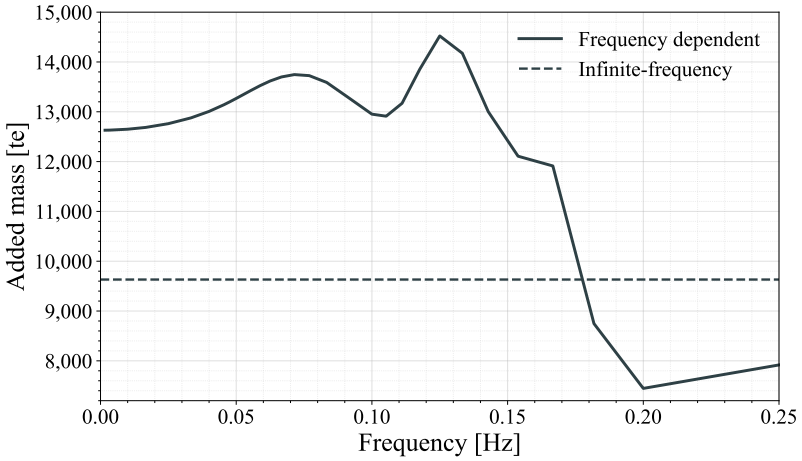

Figure 3.4: Frequency dependent added mass for $\mathbf{A}_{11}$.

Table 3.2: Comparison of natural frequency of rigid body motions with different added mass assumptions: No changes (no added mass), Infinite (infinite added mass), Individual (added mass at frequency of rigid body motion).

Motion	Reference [Hz]	No changes [Hz]	Infinite [Hz]	Individual [Hz]
Surge	0.007	0.00979	0.00808	0.00773
Sway	0.007	0.00985	0.00813	0.00775
Heave	0.049	0.07340	0.04981	0.04838
Roll	0.036	0.03951	0.03552	0.03528
Pitch	0.036	0.03947	0.03550	0.03526
Yaw	0.011	0.01691	0.01260	0.01186

It can be seen that the infinite frequency added mass already resolves in better results than the case with a frequency-dependent added mass matrix, where an added mass of 0 kg was assumed. However, the values are still significantly off for most DoF. With the individual added mass, read of at the frequency of the rigid body motions, the results in Table 3.2 show a maximum difference of 10.7 %, which is lower than for the others, indicating that this is the correct approach.

The small differences that are still visible most likely resolve from the accuracy of the reported frequencies. The added mass for the surge motion, for example, was read off at 0.007 Hz, as this was the reported value. However, the value could be rounded and could hence also be, for example, in a range between 0.066 Hz and 0.074 Hz. This would have resolved in a different added mass and thus also a different natural frequency. A more accurate approach would have been to integrate an iterative process of reading off the values, finding the corresponding added mass and using it as an input until no significant changes are observed. This is also a possible approach for the case where the correct natural frequency is not known and one has to start with a guess.

Even though this is more accurate, it is a repetitive task when doing it manually. At that point in the thesis, the Python API was not known yet. Hence, it was decided to skip this step and focus on other parts, as the accuracy was already acceptable. However, for further analysis, this method could provide higher accuracy.

3.1.3 Building a Flexible Floater in OrcaFlex (A2 M)

A rigid model of the U-Maine 15 MW model already exists, as stated in subsection 3.1.1. However, a flexible model is also required as a reference model. A first attempt of implementing a flexible model with the same characteristics was already made in the pre-thesis. This process is quickly recapped.

Flexible floater recap

The same approach as in the pre-thesis was followed, where the flexible *line* elements solely capture the structural and hydrostatic properties. All structural damping is removed from the *line* elements. The hydrodynamics, on the other hand, were captured by using the same *vessel* as used for the rigid floater. The mass, moment of inertia, submerged volume and hydrostatic stiffness were set to zero, leaving an empty hull that determines the loads via the RAO calculation in OrcaWave and also captures the frequency dependent added mass matrix. The empty rigid floater hull was connected to the centre column of the flexible floater and transfers the hydrodynamic loads this way. This method is mentioned in Engebretsen et al., 2020 as a typical approach. Two important drawbacks of this method are mentioned in this paper. Lumping the loads onto a single point does not allow for structural analysis, as the internal sectional loads along the submerged substructure can't be accessed. Furthermore, the effect of hydroelastic coupling is not captured.

The first step of capturing the structural properties of the UMaine VolturnUS floater was to rebuild it in the Computer-aided design (CAD) tool Siemens NX using the data sheet from iea wind (Allen et al., 2020). This way, missing parameters like the wall thickness and height of the constant and fluid ballast were determined.

Next, the floater was split into four different types of parts: centre column (x1), arms (x3), side columns (x3) and struts (x3). These single parts were rebuilt in OrcaFlex using the *line type*. OrcaFlex *line types* only allow for cylindrical cross sections. The centre column, side column and struts are cylindrical and were hence easily implemented. However, the arms have a rectangular cross-section, requiring the calculation of an equivalent stiffness and diameter. The properties of each component are reported in section A.2.

OrcaFlex *line types* allow for inclusion of added mass properties per *line type*. These were not used and are set to zero. The same was done for the drag and lift coefficient. Instead, the hydrodynamic properties of the floater were calculated with OrcaWave and imported into OrcaFlex and applied to the rigid floater hull as explained above.

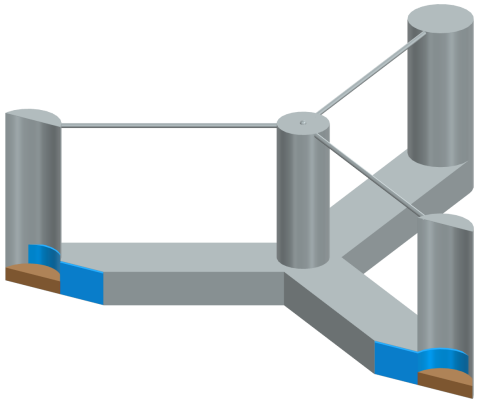

(a) Floater rebuild in Siemens NX with a wall thickness of 45 mm, a constant ballast height of 2.64 m (brown) and a sea water height of 6.57 m (blue).

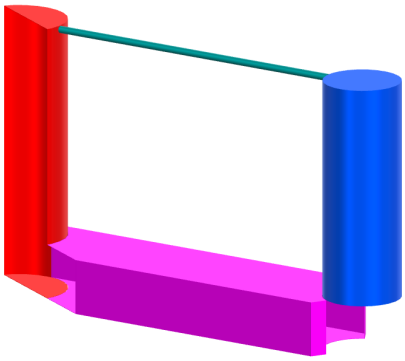

(b) Floater rebuild using 4 different parts: centre column (blue), arm (pink), side column (red), and struts (teal). Section view to include more detail.

Figure 3.5: Combined view of the 15 MW CAD model: Full rebuild and parts breakdown.

Flexible floater in Siemens NX

The first step to improve the floater was to check the initial CAD model by comparing the CoG, CoB, moment of inertia and displaced volume. The results are reported in Table 3.3. It becomes evident that the CoG as well as the moment of inertia are off compared to the data sheet form Allen et al., 2020.

Table 3.3: Comparison of Parameters. Data sheet (Allen et al., 2020), CAD model (pre-thesis), CAD 2.0 (thesis).

Parameter	Units	Data sheet	CAD	CAD 2.0
Hull Displacement	m^3	20,206	20,206	20,206
Hull Steel mass	t	3,914	3,914	3,914
Tower Interface Mass	t	100	100	100
Fixed Ballast Mass	t	2,540	2,540	2,540
Seawater Ballast Mass	t	11,300	11,300	11,300
Draft	m	20	20	20
Freeboard	m	15	15	15
Vertical CoG from SWL	m	-14.94	-14.83	-14.94
Vertical CoB from SWL	m	-13.63	-13.63	-13.63
Roll Inertia about CoG	kg/m^2	1.25E+10	1.17E+10	1.18E+10
Pitch Inertia about CoG	kg/m^2	1.25E+10	1.17E+10	1.18E+10
Yaw Inertia about CoG	kg/m^2	2.37E+10	2.17E+10	2.17E+10

The difference in the CoG was simply accounted for by changing the density of the constant ballast in the side columns. The density is not explicitly specified in the data sheet, where it is simply stated to be a combination of iron and concrete. Hence, the density could vary between 2200 kg/m^3

(high concrete and low iron share) and 7850 kg/m^3 (high steel and low concrete share). Increasing the density to a value of 6225 kg/m^3 from 2650 kg/m^3 whilst maintaining the total mass resulted in a match of the CoG (Table 3.3). Additionally, the moment of inertia was altered. However, not enough in order to get the same result as reported in the data sheet.

The improved model version in Siemens NX has a perfect match in CoG. However, no simple changes could be made that change the inertia without also altering other model properties. Thus, the following decision was made: Instead of further changing the flexible model by changing properties of the floater, the rigid model is adjusted to match the moment of inertia of the floater model as reported in Table 3.3. This was done, as the goal is not to have a flexible model matching the UMaine model but to have two similar models, one rigid and one flexible. The rigid model was adjusted as explained in subsection 3.1.1.

Flexible floater in OrcaFlex

The next step was to integrate the changes made to the model in Siemens NX into the OrcaFlex model. However, even after adjusting the density of the side column ballast, the heave, pitch and roll natural periods were still off. Surge, sway and yaw natural frequency, on the other hand, matched the results, indicating that the mooring system was correctly connected to the flexible floater.

Using the theory from section 2.2 the differences in heave, pitch and roll allowed narrowing down possible reasons to either a wrong CoG, CoB, displaced volume or waterplane area. The cross-section at SWL is simply four cylinders with a defined diameter. The diameter was checked, and no difference were found. Hence, the OrcaFlex model was checked for differences in the CoG, CoB and moment of inertia.

At this point the model from Siemens NX was utilised to compare the parameters of the single components from OrcaFlex with the parameters of the single components in Siemens NX. Already in the previous work some sources of inaccuracy were determined, like the missing feature of a lid. The lids were simply added to match the mass. No focus was put on the ratio between the lid at the top and bottom in order to match the CoG. This was now accounted for by determining a ratio between the top and bottom lids. Furthermore, additional buoyant elements were added to the centre and side columns in order to account for the missing volume at these points due to limitations in the modelling capabilities which only allow for the parts to have volume along the *line*. The position of these buoyant elements was adjusted to match the CoB.

This way a model was created with an acceptable match between the mass, submerged volume, CoG and CoB, as summarised in Table 3.4.

Table 3.4: Comparison of parameters between data sheet and OrcaFlex floater model.

Parameter	Units	Data sheet	OrcaFlex
Hull Displacement	m^3	20,206	20,206
Hull Steel mass	t	3,914	3,914
Tower Interface Mass	t	100	100
Fixed Ballast Mass	t	2,540	2,540
Fluid Ballast Mass	t	11,300	11,300
Vertical CoG from SWL	m	-14.94	-14.94
Vertical CoB from SWL	m	-13.64	-13.64
Roll Inertia about CoG	kg/m^2	1.251E+10	1.179E+10
Pitch Inertia about CoG	kg/m^2	1.251E+10	1.179E+10
Yaw Inertia about CoG	kg/m^2	2.367E+10	2.177E+10

Despite the difference between the two models in CoG being below 0.01 m, there were still a big difference between the rigid body motions. In the previous work, the differences were argued to be due to the difference in the CoG that existed then and the mismatch in moment of inertia. However, this issue was resolved in the current model. Furthermore, the mismatchment of the moment of inertia was taken care of by adjusting the rigid floaters' properties accordingly, as explained in subsection 3.1.1. But, even with these changes, there was still a difference between the rigid body motions. The reason for this is discussed in the following section.

3.1.4 Impact of Line Segmentation near SWL in OrcaFlex (A2 Q)

A first suspicion was that the difference in rigid body motions between the flexible and rigid floater stems solely from the flexibility of the floater. This was investigated by increasing the stiffness of the floater. Increasing the stiffness did not influence the results enough to explain the observed difference. Hence, there had to be a different underlying effect.

The line elements consist of many segments and nodes, as explained in subsection 2.8.1. FEM tools are typically sensitive to the amount of elements used. Testing this for the flexible floater, a sensitivity to the number of elements was identified. More specifically, to the amount of elements near SWL.

In order to investigate this assumption, an additional study was performed, focusing on the change in rigid body motions over varying line segmentation near SWL. The simplified case shown in Figure 3.6 was created. Only one single cylinder was modelled. Two constraints were chained such that the first only allows for movement in global z. The second one was linked to the first one but rotated by 1.5°,forcing the cylinder to follow this initial rotation. Two constraints were needed, as otherwise movement along the local z-axis would occur.

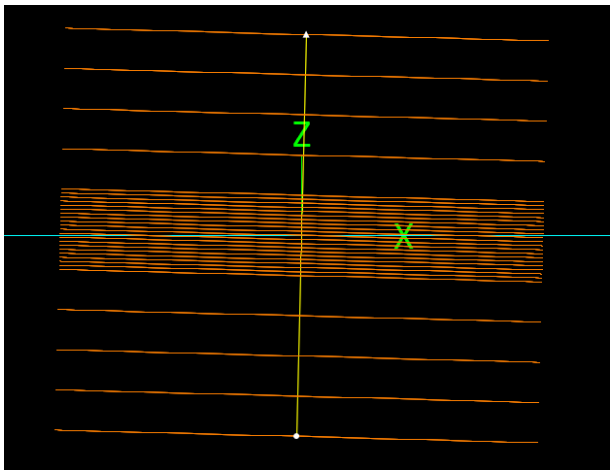

Figure 3.6: Set-up of the single-cylinder system with varying segment length near SWL.

The elements near SWL were grouped into a belt of total length 2 m. The amount of elements in this belt was varied from 1 to 50 elements. Thus, the resulting length of each individual element is determined as:

$$l_{Element} = \frac{l_{total}}{\text{Number of Elements}} \tag{3.1}$$

A Python script using the OrcaFlex API explained in subsection 2.8.3 was written that loads and changes the described OrcaFlex model. The heave natural period was automatically extracted from the modal analysis tool for a changing amount of elements near SWL. The results are shown in Figure 3.7. Additionally, the theoretical heave natural period was determined by using Equation 3.2, as well as the natural heave period for a case in OrcaFlex with no initial pitch.

$$T_3 = 2\pi\sqrt{\frac{m}{C_{33}}} \tag{3.2}$$

$$C_{33} = \rho g A_{wp} \tag{3.3}$$

$$A_{wp} = \pi a r \tag{3.4}$$

where r is the radius and a is the stretched side of the ellipse.

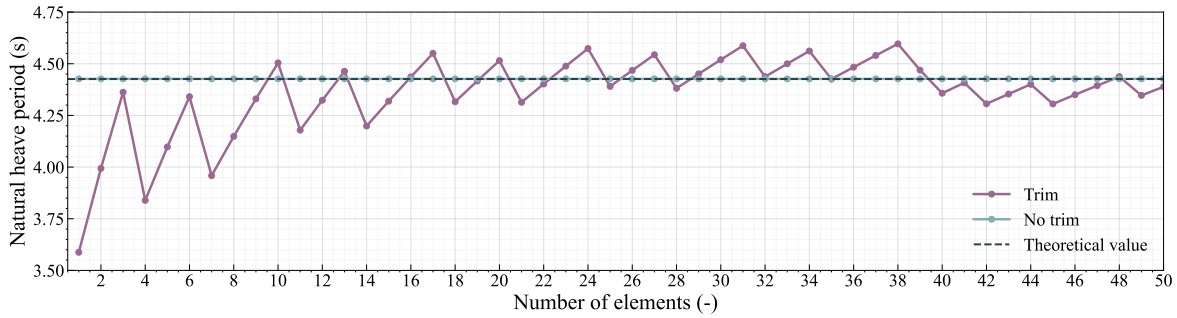

Figure 3.7: Natural heave period over changing amount of segments near SWL for the cylinder case with initial pitch of 1.5°, without initial trim, and the theoretical value.

The case with an initial trim shows a clear deviation from the theoretical value. Even with an amount of 50 elements, which results in a segment length of 0.04 m, the result from the simulation and the theoretical value do not match. Nevertheless, the difference decreases with an increasing amount of elements. It is hence concluded that the results converge with an increasing number of elements.

Equation 3.2 displays that the heave period is influenced by the mass (m), density (ρ), gravity (g) and waterplane area (A_{wp}). Density and acceleration are constant. Hence, the only two remaining variables are the waterplane area and mass.

Variation in the mass can be caused by a wrongly determined volume. Hence, this was checked. The OrcaFlex documentation clearly states that partly submerged elements are accounted for by calculating the proportion wet. This value indicates how much of the line is actually submerged and determines the corresponding submerged volume.

In terms of the waterplane area, the OrcaFlex documentation states that every body is assumed to be a "wall-sided body". This means that "OrcaFlex does not take account of the variation in waterplane area with draft that arises from the circular cross-section." This assumption potentially caused the observed differences, as the example was not a wall-sided body due to the trim angle of 1.5°.

This assumption was discussed with OrcaFlex and stems from the fact that the OrcaFlex *line element* is typically used for long *lines* with small diameters. These long *lines* require the use of simplifications. The small diameter of the *lines* makes the effect of the assumption negligible.

In the case of this thesis, the floater was built of *line* structures with a big diameter. Hence, the influence of the simplification that *lines* are assumed to be wall-sided has a significant influence on the rigid body motions. The made assumptions are within the source code, which can't be accessed in this thesis. Hence, a sensitivity study on the FOWT model's rigid body motion to the number of segments near SWL was performed. The theoretical value from Allen et al., 2020 is reported as a reference. The results are shown in Figure 3.8.

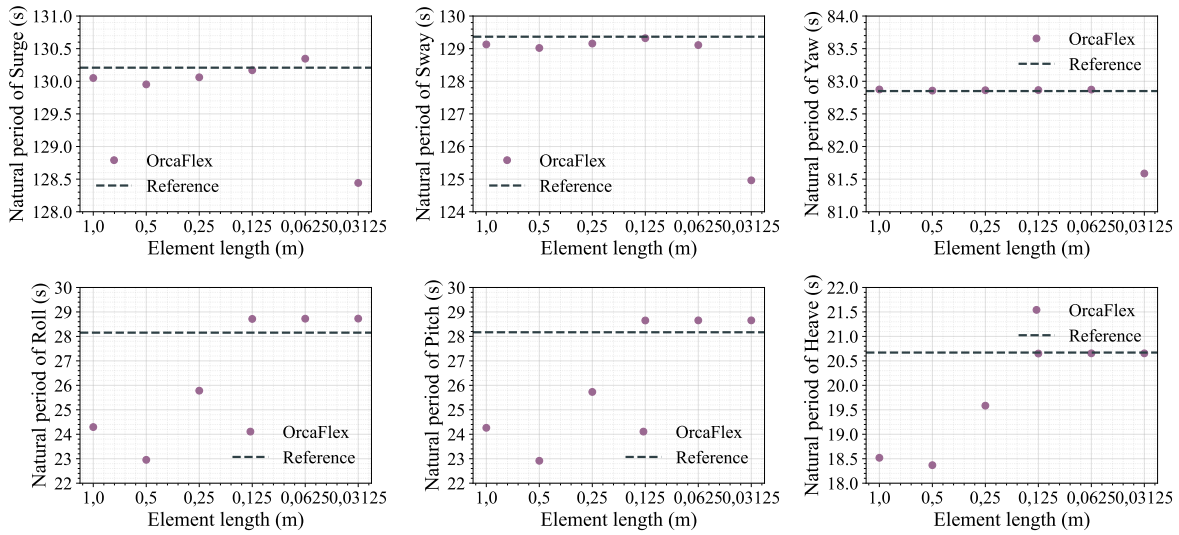

Figure 3.8: Change of rigid body periods of the FOWT model over segment length near SWL.

The smallest relative differences (2.4 % in roll) between the reference value reported in the data sheet from Allen et al., 2020 and the model was found in all degrees of freedom for an element size

of 0.125 m. Hence, this was chosen as *line* discretisation near SWL. In order to be computationally efficient, not the whole cylinder was modelled with this high accuracy but only the part around SWL.

Condition number

Even though high resolution of elements near SWL gave accurate results in the static calculation, it also caused convergence issues in dynamic analysis. Very small time steps were required to achieve a stable simulation, which resulted in a high computational effort.

Hence, a different solution had to be found that allows for bigger time steps and, at the same time, a more stable simulation. Firstly, the line segmentation of the centre column was changed. Here it was found that the more coarse segmentation of the centre column does not significantly influence the static position nor the rigid body motions. Instead, the differences stem from the side columns.

In the next step, rigid *6D buoys* of the *spar buoy type* were used for the side columns instead of flexible *lines*. This had the clear advantage of more accurate calculation of the waterplane area and the clear disadvantage of being rigid. The static results and rigid body motions showed good agreement with the reference values from Allen et al., 2020 and were even closer than the case with flexible high-resolution side columns. This shows the advantage of a more accurately calculated waterplane area.

Despite the good match in static position being promising, replacing the flexible side columns with a rigid body was expected to have a negative influence on the tower dynamics. Hence, the first tower bending mode in fore-aft was compared to the flexible case with fine segmentation. More detailed information on how the first tower mode was identified follows in the next sections. For now the shape, natural frequency and MAC number are important, which describe the similarity between two modes as explained in subsection 2.6.2.

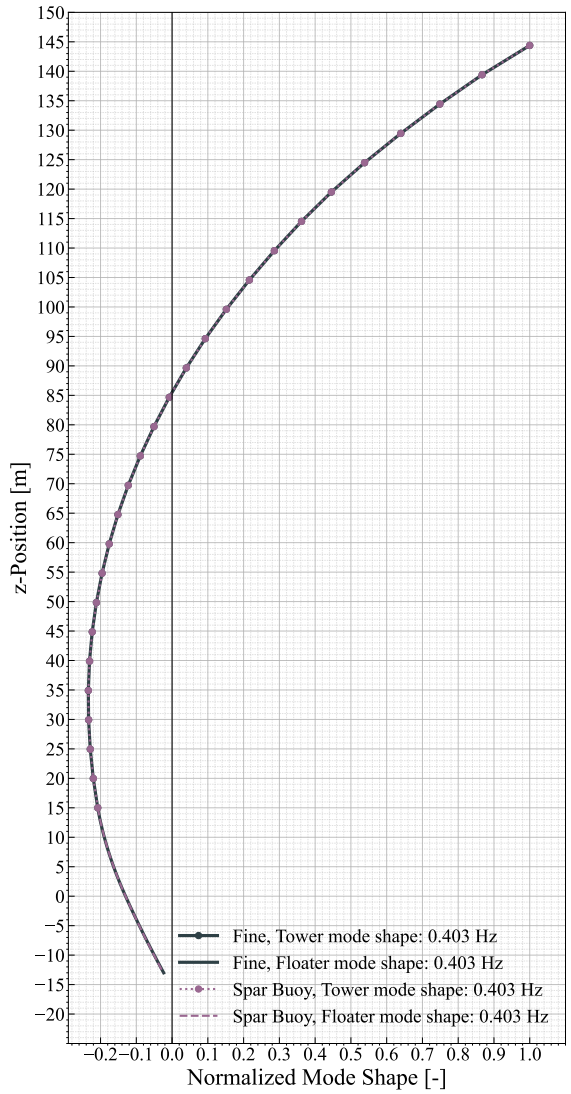

Figure 3.9: Comparison of the first tower bending mode in fore-aft of the fine model and the model with rigid side columns.

Replacing the flexible side columns with rigid *spar buoy* types did not change the natural frequency, nor did it effect the normalised mode shape. This is indicated through the identical tower natural frequency and MAC number of one, which compares the mode shape of the fine flexible case and the case with rigid side columns. More information on the identification of tower modes and the presentations given in subsection 3.1.6.

The impact of the side columns on the tower modes being that small is expected to stem from the fact that the tower is not directly connected to the side columns but to the centre column. Even more so, the side columns are not directly connected to the centre column. Hence, the impact of them being rigid is considered small, and the assumption to replace the flexible side columns with rigid side columns and to use more coarse segmentation for the centre column in order to be able to run dynamic simulations is considered valid.

3.1.5 Validation of Flexible Floater (A3 M)

The final step of modelling the flexible floater was the floater validation. This step is crucial to make sure that the flexible floater model is captured correctly and can be used as a reference to the rigid models, including a flexible element. The validation method used is not optimal, as the flexible floater was solely compared to the adjusted rigid floater from OrcaFlex. The not changed rigid floater model was only validated using the the data sheets from Allen et al., 2020, and Li et al., 2023, however no other source was available to validate the adjusted rigid floater model. A more optimal way of validation would have included an additional data source for a fully flexible floater with matching properties or, even better, real-life measurements.

Key points that were compared were the static equilibrium position of the floater (Table 3.5) and the rigid body motions (Table 3.6) determined through *modal analysis* in OrcaFlex and decay tests.

Firstly, the static equilibrium position of the floater was compared, yielding the results of Table 3.5. The biggest difference was observed for R2 with 5.42 %. The difference is expected to stem from the added flexibility of the flexible floater.

Table 3.5: Comparison of rigid and flexible floater designs' static positions.

Floater Design	**x [m]**	**y [m]**	**z [m]**	**R1 [°]**	**R2 [°]**	**R3 [°]**
Rigid	-0.352	-0.005	-0.554	-0.019	1.402	-342e-6
Flexible	-0.358	-0.005	-0.570	-0.020	1.478	-350e-6

Using the *modal analysis* tool with the constant individual added mass as discussed in subsection 3.1.2 the rigid body motions were found as the first six modes with the lowest natural frequency. The results are summarised in Table 3.6. Good agreement can be seen between the flexible floater and rigid floater, as well as the data sheet. Solely the pitch and roll motion show slight differences that are expected to stem from the different static position and added floater flexibility.

Table 3.6: Comparison of natural frequency of rigid body motions between reference [1]: Allen et al., 2020, reference [2]: Li et al., 2023, *modal analysis* in OrcaFlex, and decay test in OrcaFlex. All for flexible (F) and rigid (R) floater model.

Motion	**Ref [1]: R** [Hz]	**Ref [2]: F** [Hz]	**Modal: R** [Hz]	**Modal: F** [Hz]	**Decay: R** [Hz]	**Decay: F** [Hz]
Surge	0.007	0.0074	0.0077	0.0077	0.0077	0.0077
Sway	0.007	0.0074	0.0077	0.0077	0.0077	0.0077
Heave	0.049	0.0484	0.0484	0.0484	0.0483	0.0485
Roll	0.036	0.0348	0.0355	0.0348	0.0355	0.0351
Pitch	0.036	0.0347	0.0355	0.0349	0.0357	0.0353
Yaw	0.011	0.0113	0.0121	0.0121	0.0120	0.0120

Additionally, to using the *modal analysis* tool from OrcaFlex, decay tests have been performed to identify the rigid body motions. For each DoF a different setup was chosen. Using a *winch*, the floater was displaced in the DoF of interest. This is shown in the example of surge and pitch decay in Figure 3.10.

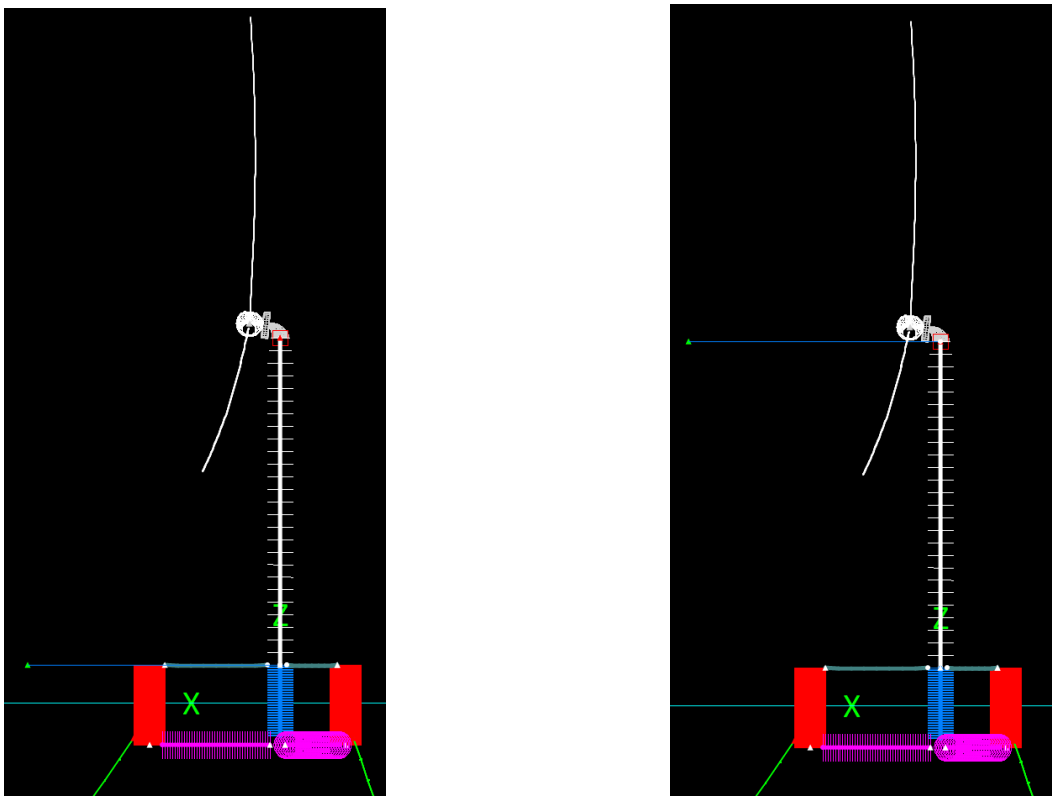

(a) OrcaFlex setup for a surge decay test, with a winch (blue line) connected to the FOWT.

(b) OrcaFlex setup for pitch decay test, with winch (blue line) connected to the FOWT.

Figure 3.10: OrcaFlex setups for surge and pitch decay tests using a winch (blue line).

After 10 seconds of displacement, the winch connection was released, and the FOWT oscillates freely around static equilibrium. The first 200 seconds were neglected in order to not account for the transient. Only the last 6000 seconds were kept for analysis. The resulting time series and spectra are shown in Figure 3.11. Since surge and sway, as well as pitch and roll, were similar due to symmetry, only one of each is shown. The frequency of each rigid body motion is additionally summarised in Table 3.6.

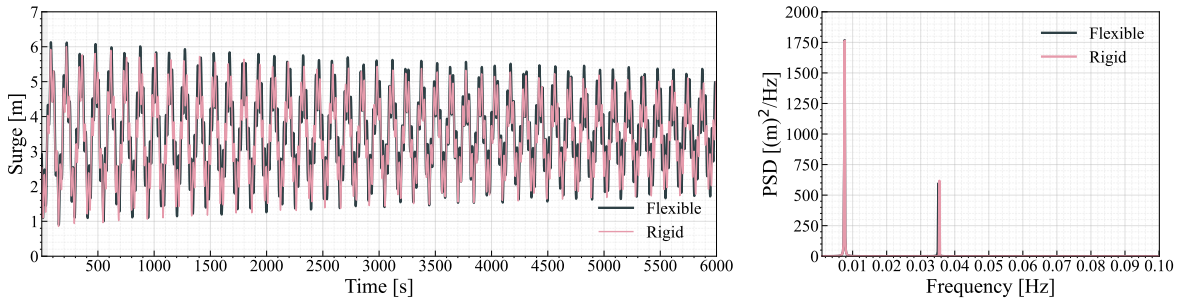

(a) Surge decay test.

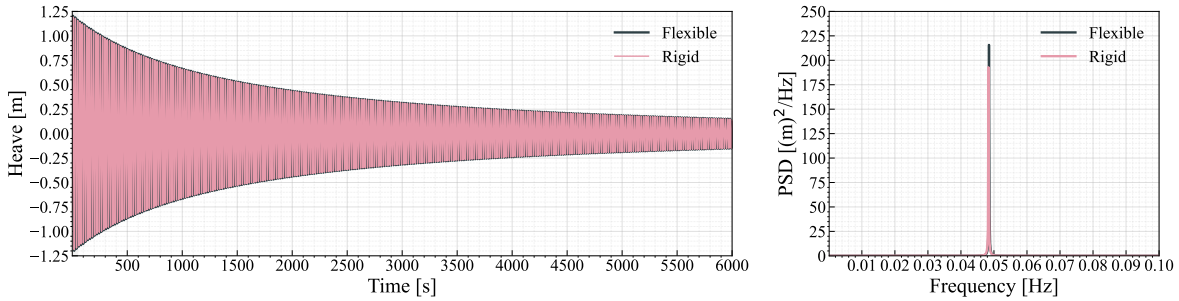

(b) Heave decay test.

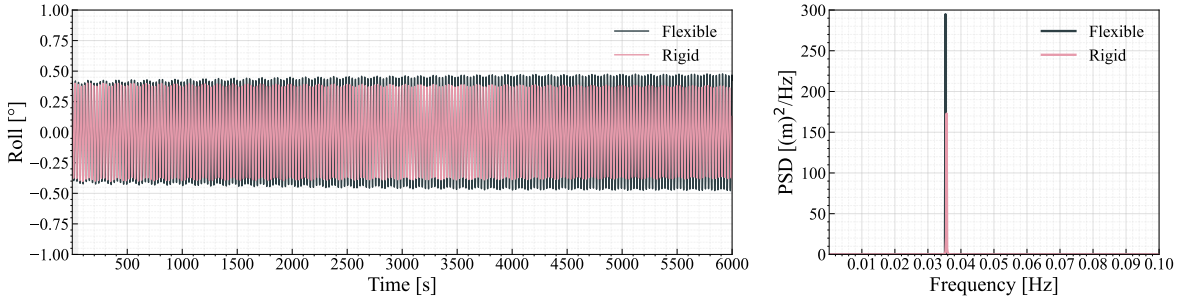

(c) Roll decay test.

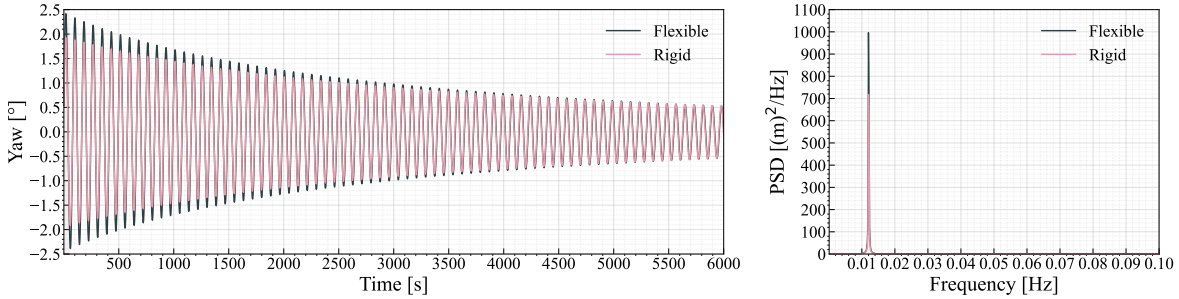

(d) Yaw decay test.

Figure 3.11: Time series and spectrum of decay tests.

The identified frequencies, show agreement within 9% when comparing rigid and flexible floater,

as well as compared to the modal analysis and benchmark results. The surge displacement shows additional coupling with pitch motion. Looking at the setup in Figure 3.10a one can see that the winch was connected above SWL, resulting in a moment. A more optimal setup would include a winch at a lower position. Again, the pitch and roll natural frequencies are different for flexible and rigid floaters. This is expected to be due to the added floater flexibility.

3.1.6 Floater Error Assessment (A4 M)

All validation steps show sufficient agreement between the two models and the reference. Hence, no further validation steps were made prior to the next steps. Unfortunately, only after setting up the different designs and running all designs for the differently complex environmental conditions were results found that led to the decision to look at the RAO. With all simulations and preparations already finished, there was no more time to identify the reason for the behaviour, redesign the floaters, and rerun all simulations. Hence, the focus was put on identifying the reason for the observation, the impact on the results, and possible solutions to solve this error.

The starting point of this was the calculation of the RAO's by simulating the different models for regular waves with a wave height of 1 m for a range of periods from 3 seconds up to 30 seconds in steps of 0.25 seconds. The wave heading is 0°, so the motions of interest are surge, heave and pitch. The resulting time series after the initial transient was used to identify the maximum magnitude, which is then the response of the design in the DoF of interest. The resulting RAOs in surge, heave and pitch of the rigid floater and flexible floater were investigated. The most interesting observations were made at low frequencies in the range of the rigid body natural frequencies. The RAOs in this frequency range are shown in Figure 3.12.

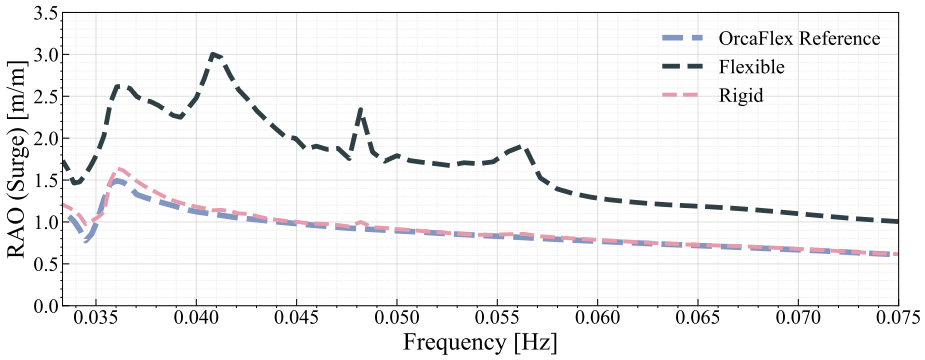

(a) Surge RAO of OrcaFlex example, flexible floater design and rigid floater design.

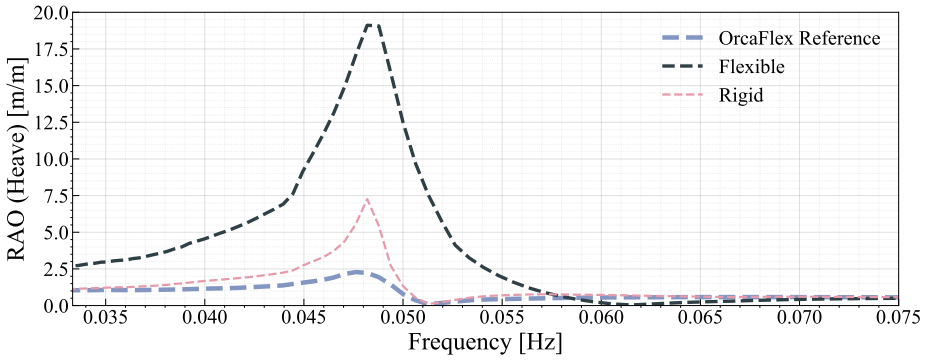

(b) Heave RAO of OrcaFlex example, flexible floater design and rigid floater design.

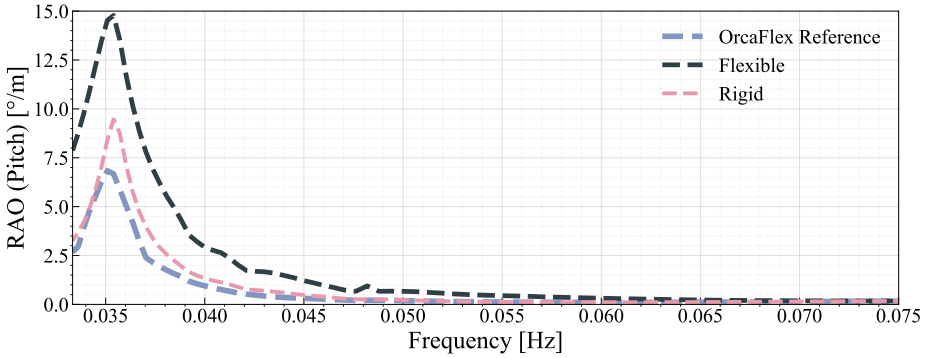

(c) Pitch RAO of OrcaFlex example, flexible floater design and rigid floater design.

Figure 3.12: RAO plots (surge, heave, and pitch) of OrcaFlex example compared to flexible and rigid floater designs.

The flexible and rigid design both show an increased response at the natural frequency of the respective rigid body motion. Especially the flexible design shows highly increased amplitudes. The biggest discrepancy was found in the heave direction, where the flexible floater shows almost 10 times the excitation of the OrcaFlex example. In terms of the tower bending, the pitch motion is significantly more load driving than surge and heave. For pitch, the flexible case shows more than

double the response. The rigid floater also shows an up to a 30% increased response in pitch.

Recalling the theory from section 2.5, and more specifically Figure 2.4b, damping is seen to have a big impact on the response at excitation frequency. Hence, all sources of damping were revised. The flexible floater's *lines*, which capture the mass and volume, drag and added mass, were all set to zero in order to capture all hydrodynamic effects through the massless rigid floater. This is the same rigid floater used for the rigid floater design, which, in addition to the added mass and RAOs also captures the damping. The frequency-dependent damping terms were compared between the different models, and no discrepancies were identified. However, OrcaFlex includes an additional category called 'Other damping', which captures additional linear damping and quadratic damping (viscous) for each DoF. All viscous damping entries were set to zero for the flexible and rigid floater designs, whereas the OrcaFlex example had entries for each DoF. The lack of this additional damping clearly explains the observed increased response.

In the next step the rigid and flexible floater design were adjusted to capture this additional damping in order to assess the mistake made by neglecting it. The RAOs of the adjusted flexible and rigid floater for pitch are shown in Figure 3.13 in comparison to the OrcaFlex example and the designs without viscous damping.

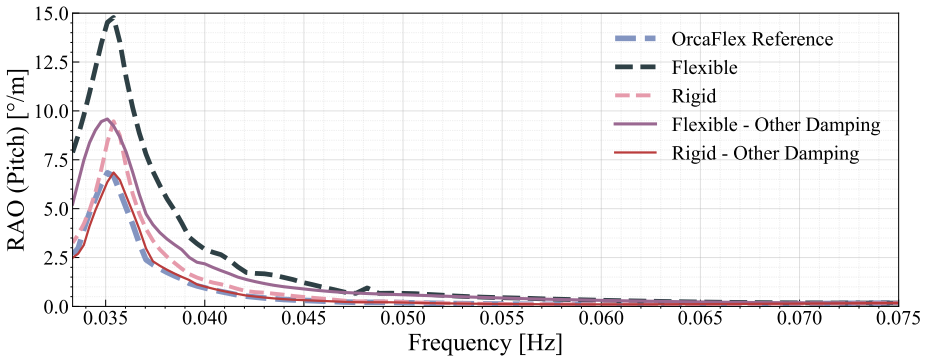

Figure 3.13: Pitch RAO of OrcaFlex example, flexible floater design, rigid floater design, and flexible as well as rigid floater design including viscous damping.

Including the viscous damping proved to be the mistake for the rigid floater design, as including it matches the curve with the OrcaFlex curve. The response amplitude of the flexible design was also reduced significantly; however, it is still notably higher.

As previously mentioned, the flexible floater designs' hydrodynamic loads are captured by the massless rigid floater. However, with the difference in RAOs identified, it was suspected that a further underlying effect results in unintentional hydrodynamic properties from the *line* elements. Recalling Figure 3.12b the heave motion shows the biggest discrepancy between the flexible and rigid floater design. This suggests that the *line* elements were influencing these motions, leading to double counting, even though all hydrodynamic coefficients were set to zero.

The *line* elements of the flexible floater do capture the hydrostatic properties by capturing the volume. Hence, it was suspected that waves change the submerged volume of the floater which result in an additional heave force. Any changes in heave motion will result in double counting of heave forces. Engebretsen et al., 2020 explains a similar modelling approach to the one used in this thesis, where they state that:

"Additionally, the time-domain solver must also allow specifying buoyancy calculation on beam

elements only up to the mean free surface (instead of to the instantaneous free surface) in order to avoid double counting of heave excitation. By this approach, the vertical centre of buoyancy is still coupled with heave motion but is not strictly correctly calculated under incoming waves, as the wetted length is only calculated up to MWL." (Engebretsen et al., 2020)

The explanation matches the observed behaviour, and the effect is visualised in Figure 3.14. The leftmost case shows an example cylinder with no waves. The submerged volume goes up to SWL and results in a buoyancy force ($F_{B,1}$). This is case behaves as it should. The case in the middle includes waves and shows that the bypassing wave changes the submerged volume and hence increases the resulting buoyancy force ($F_{B,2}$). The additional buoyancy force due to the wave changing the submerged volume is also accounted for by the RAOs of the rigid floater hull. It is accounted for twice. Engebretsen et al., 2020 additionally suggests a solution to this, which is visualised in the rightmost case. The bypassing waves do not result in a change in submerged volume. The submerged volume is still only calculated up to the static SWL with no waves, and hence the buoyancy force is identical to the first case ($F_{B,1}$). This way, heave motions are only accounted for through the rigid floater hull. However, no simple solution to implement this approach was found in OrcaFlex.

The way that heave is being counted double also explains why pitch is influenced. The different *line* elements are influenced by the waves at different times, resulting in different heave forces with a lever due to the distance to the CoG. This creates a moment resulting in the increased pitch excitation.

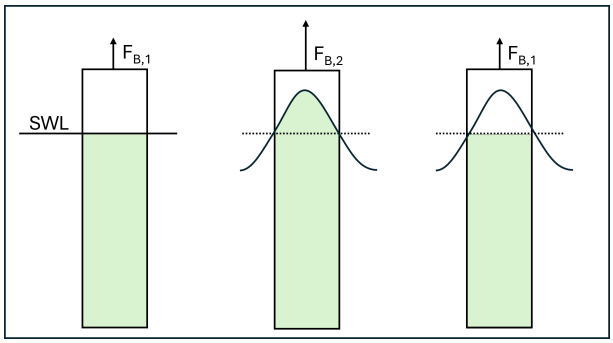

Figure 3.14: Submerged volume without waves, with waves and dynamic calculation of submerged volume, and waves but static calculation of submerged volume.

The last step after identifying the reason for the observed behaviour was to assess the impact on the results. For this, the excitation had to be compared to the response. The external excitations stem from the waves. In the case of regular waves, the highest wave period is 9.45 seconds, which corresponds to 0.106 Hz. The irregular wave with the highest peak period is also 9.45 seconds. However, due to the fact that the waves are irregular, they also include wave components with a higher period. Hence, only the case of irregular waves was used as an excitation. Figure 3.15 shows the time series of the irregular wave state at a peak period of 9.45 seconds and the resulting spectrum.

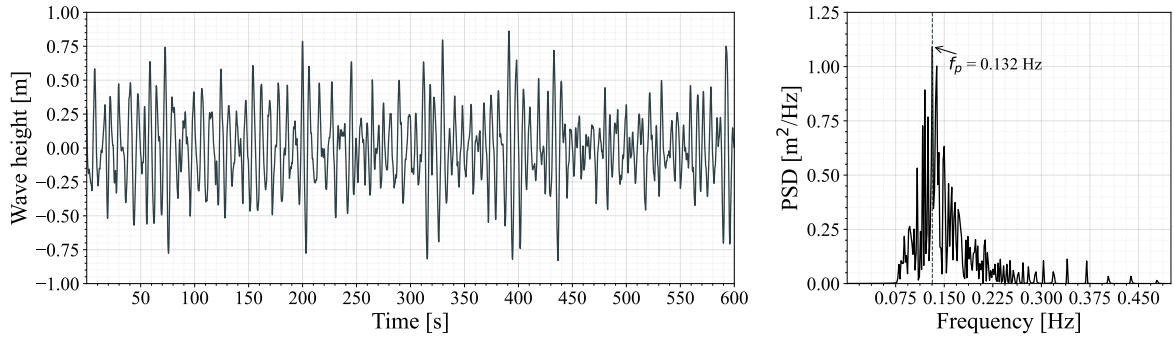

Figure 3.15: Wave time series and spectrum for irregular sea state with Hs = 4.52 m and Tp = 9.45 s.

Including the spectrum in the RAO plot of pitch motion shows the overlapping range of frequencies (Figure 3.16a). It becomes evident that the frequency range at which the big differences in the RAOs between the different designs are identified do not overlap with the excitation frequency. Figure 3.16b focuses on the frequency range in which the wave spectrum has most energy, ranging from 0.075 Hz to 0.2 Hz.

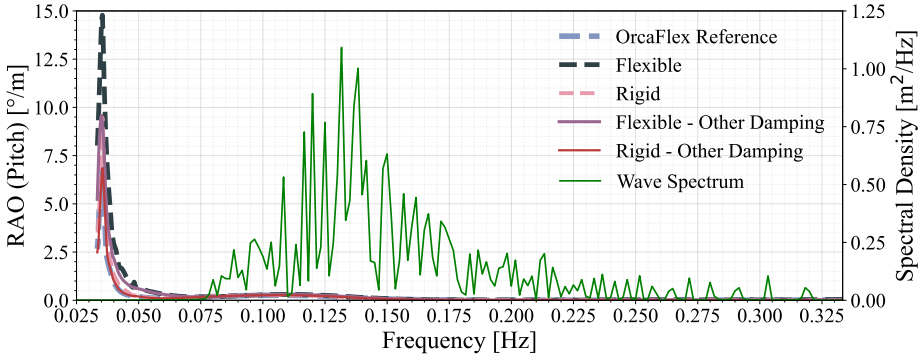

(a) Pitch RAO and wave excitation combined.

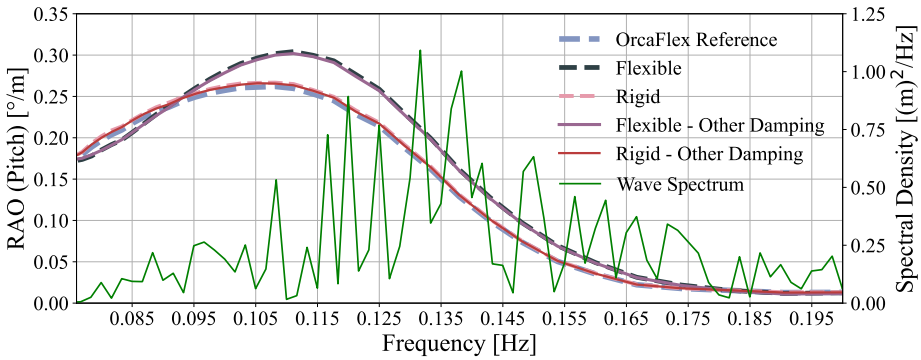

(b) Pitch RAO and wave excitation combined focused on frequency range with the highest energy content.

Figure 3.16: Pitch RAO and wave excitation combined.

In Figure 3.16b it can be seen that the rigid case with and without viscous damping are still identical. The same applies for the flexible floater design with and without viscous damping. This shows that in the range of wave excitation there is indeed no difference between using the model with and without viscous damping. However, there is a difference between the flexible and rigid model, probably stemming from the double counting of heave motion explained previously. The difference is in the range of 0.05° pitch angle per metre wave height. This is significantly less than observed at the peak but still needs to be considered when using the flexible floater design as a reference in section 4.3 for cases including waves. Static calculations as well as dynamic simulations, including no waves, like a decay test, constant wind or turbulent wind, are not significantly influenced by this.

3.1.7 Tower Mode Identification Method (A5 M)

In order to compare the natural frequency and mode shape of different models, the modes of interest have to be identified. In the case of a single-body system, the different mode shapes solely indicate higher-order modes or modes of the same order but in different directions. Hence, the process of identifying modes is clear.

On the other hand, in the case of a system with multiple flexible components, it was found not to be straightforward to identify the modes of a single component. The FOWT model consists of multiple flexible bodies, namely, the tower, the blades, the mooring lines, and, depending on the model, the floater. Hence, the model is a flexible multibody system. The coupling of the different flexible components results in no mode where only one flexible component is moving (Bir and Jonkman, 2008). Instead, it seems that the different modes are dominated by different components. This makes the identification of modes in the case of differently stiff components (tower vs blades/mooring lines) difficult, as the softer components (blades/mooring lines) are always included as noise to some extent. The goal is to extract those modes where the component of interest (tower) is dominating the structure mode and coupling with other components is minimal.

No clear definition was found on how to identify the tower's first bending natural frequency of a FOWT during the literature review. Hence, three different methods to address this problem are proposed in the following section. Each of them has different advantages and disadvantages. The first method relies on the theory of decay tests explained in section 2.7. The second and third methods rely on the *modal analysis* tool from OrcaFlex, both with different adjustments made to the model. The theory of these methods is explained in chapter 2. This section focuses on the application of the methods in the scope of the thesis.

Decay test

The first method useds the principle of a decay test in order to identify the first tower bending mode in fore-aft. Again, a winch was used in the floater setup. The winch was connected to the tower top, similar to the setup for the pitch decay test in Figure 3.10b. Instead of slowly displacing the FOWT gradually, a big haul-in rate was chosen that is applied over a short time frame. This resulted in a displacement of mostly the tower top and hence forces a first tower bending mode in fore-aft.

In post-processing, the time series of the tower bending at the root was exported. Additionally, to the time series, the spectrum of this time series of tower bending was created, and they are presented together in Figure 3.17. This power spectrum contains the amount of energy for each frequency. One of the peaks present in the Power Spectral Density (PSD) is the tower's natural frequency.

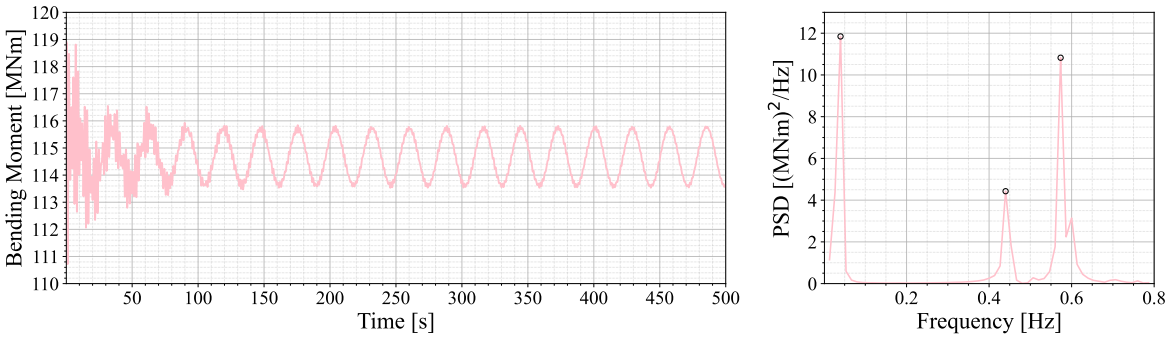

Figure 3.17: Time series and spectrum of tower decay for the rigid floater model.

The complete time domain is visualised, but only the first 75 seconds are analysed in the PSD. Three clear peaks can be seen that are indicated by the markers. The first peak is too low for tower bending and is indicating a rigid body motion. The identified frequency of roughly 0.04 Hz and the way the model is excited both match the pitch natural frequency.

The second peak is located at 0.573 Hz, and the third highest peak is at 0.44 Hz. The peak magnitude indicates the amount of energy in tower bending at each frequency. A big peak does not necessarily imply that it is a tower bending mode. As can be seen for the first peak, the large amount of energy can also stem from another motion that results in tower bending. Hence, it is important to understand the reason for each peak, which requires looking at the motion of the tower in comparison to other motions. This way, the mode in which the tower is dominant can be identified. In the example of Figure 3.17 the peak at 0.573 Hz is too high for a tower's first bending frequency and is expected to show strong coupling with other components. The peak at 0.44 Hz, on the other hand, matches with literature. Thus, the peak at 0.44 Hz would be identified as the first tower bending frequency using the decay test. The result is discussed in subsection 4.1.1, subsection 4.1.2 and compared to literature later in section A.5.

A clear advantage of the time decay test is that the full system with all coupled components, as well as damping and non-linear stiffness terms, are included. This results in a time series and spectrum that captures all occurring coupling effects. However, the peaks need to be manually checked in case of multiple peaks at similar frequencies in order to understand which component is dominating the mode. Even though the setup is intuitive and the theory well defined in literature, it requires a time domain simulation. This is computationally heavy, especially for a large number of simulations, proven by the decay test shown in Figure 3.17 which ran for 43 minutes.

Mode participation

The *modal analysis* tool from OrcaFlex uses the same theory as explained in section 2.6. The results show as many modes as selected (up to the number of DoF) for the fully coupled model. For each mode the frequency is given as well as the position of each DoF. The nodes' positions make up the mode shape, which is normalised according to the maximum displacement. Hence, it does not contain any physical meaning other than the displacement of one node relative to another. Different approaches are possible to identify tower-dominated modes.

The first approach is a visual inspection of the modes, where the user manually identifies the modes of interest by looking at each mode. The goal is to find those modes that look most like a first

tower bending mode of a FOWT. Even though this works, it requires the user to check the modes and also includes a bias due to subjective decision-making.

An improved approach of this utilises the fact that the mode shape vector is reported. This includes the relative position of each DoF. The nodal displacement of the component of interest, in this case the tower, is compared for all modes. Following that, they are sorted in descending order. This gives the modes in which the component of interest is moving the most relative to the other components within that mode. In other words, those modes are found where the component of interest has the highest relative motion.

The third approach is a further development of the second one. Additionally to the mode shape vectors, the modal mass discussed in subsection 2.6.1 is utilised. The modal mass of the whole system determines how much mass is participating in the mode and is thus also referred to as the participation factor (Abdelnour and Zabel, 2024). However, the modal mass of the whole system is looked at.

It would be more interesting to focus on the modal mass of the single components. This is done by solely using the mode shape vector and mass matrix of each single component as stated in Equation 3.5 for the example of the tower.

By further dividing the component's modal mass by the total modal mass, one gets a participation factor of that component relative to the whole modal mass (Equation 3.6). By sorting the values in descending order, one can easily identify the mode where the component has the highest relative contribution to the modal mass.

$$m_{m,Tower,i} = \phi^{T}_{Tower,i} \cdot \mathbf{M}_{Tower} \cdot \phi_{Tower,i} \tag{3.5}$$

, with $m_{m,Tower,i}$ the tower modal mass of mode i, $\phi_{Tower,i}$ the tower mode shape vector of mode i, and $\mathbf{M}_{Tower}$ the tower mass matrix.

$$\gamma_{Tower,i} = \frac{m_{m,Tower,i}}{m_{m,i}} \tag{3.6}$$

, with γ_{Tower} the mode participation factor of the tower at mode i, and $m_{m,i}$ the total modal mass of mode i.

This approach is similar to the strain energy approach used in aerospace (Nieto et al., 2018 and Shen et al., 1993). This method is currently used by Dillon Volk from Siemens Gamesa to define tower mode shapes for monopile wind turbines. This approach was integrated into this work as a useful tool to find the tower mode shape of a FOWT. Credit for this approach goes to Dillon Volk.

In the case of this thesis, the multibody system is the whole system of the FOWT consisting of the flexible components: tower, mooring lines, blades, and, depending on the model, the floater. The component of interest is the tower. The procedure of identifying the tower mass matrix is explained in section A.3.

The clear advantage of this method is that it relies on quantitative measures. By considering the modal mass, it also considers the global impact of the modes. Additionally, once set up, it can be integrated into scripts and run automatically. This, in combination with the fact that frequency domain analysis is faster than a time domain solution, makes it more efficient. However, non-linear effects as well as damping are not considered.

Simplified model

The last approach of identifying the modes of a single component aims to simplify the model so far that only the components of interest are still flexible. Performing the *modal analysis* tool on this results in modes only including the component of interest, making the mode identification easier.

This method requires replacing all flexible components that are not of interest with rigid bodies. In the case of this thesis, the noise stems from the blades and mooring lines. Hence, they are replaced by rigid components that include mass CoG and moment of inertia in a mass point. Such a mass point is modelled in OrcaFlex through a *6D buoy*.

A first low-fidelity model was created to test if this approach works for the scope of the thesis. The general problem is that replacing the blades and the mooring lines with rigid *6D buoys* will alter the natural frequency of the tower. However, as will be explained in more detail in section 3.2, the tower first bending natural frequency only needs to be identified in order to tune the properties of the implemented flexible element such that a match in tower first bending natural frequency is achieved. The idea for this approach is to identify the properties of the flexible element that result in a matching tower's first bending natural frequency using the simplified model and then implement the same flexible element in the full model and still achieve a match. Using the low-fidelity model explained in section A.4 this approach could not be successfully implemented.

Hence, this approach is not suitable within the thesis. However, it generally makes the mode identification process easier and helps getting an understanding of the influence of the different components.

In conclusion, the decay test method is best known in literature and intuitive. The modal participation method, on the other hand, is less well known adjusted version of the strain energy method. Nevertheless, the advantages of reduced computational effort and allowing for implementation into automated processes lead to the conclusion to use the modal participation method. In later stages, when transferring to time domain simulations (subsection 4.3.1) the findings from the decay test and modal participation method will be compared.

3.2 Phase B: Flexile Element Design Study

The overall goal of **Phase B** is to **Implement the Flexible Element** (B1 M) between the rigid floater and the flexible tower. This includes the definition of a general implementation method and also a method of how to **Create Variations of Designs** (B2 M) that enforces different resulting mode shapes.

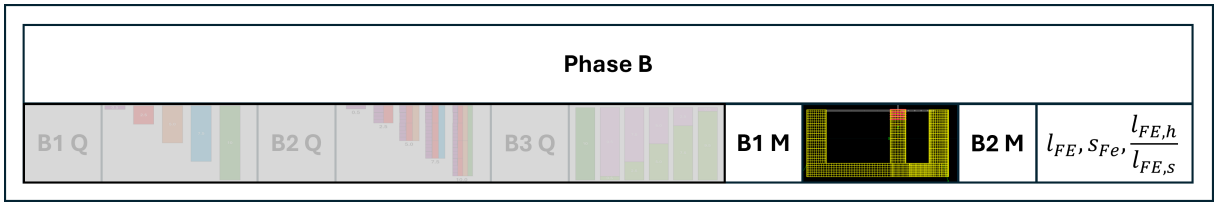

Figure 3.18: Overview highlighting the research plan for this section. Grey highlighted questions are discussed in chapter 4.

3.2.1 Implement the Flexible Element (B1 M)

The flexible element is implemented between the rigid floater and the flexible tower. The outer and inner diameters of the flexible element are identical to the tower at the root. The mass was set to a value close to zero. Furthermore, all structural damping terms have been removed. The only parameters being varied are the total length, segment length and the Young's modulus of the flexible element.

A variation in the total length means that the connection point is shifted. The tower end position stays identical, and likewise does the starting point of the flexible element. Hence, for a changing total length, the connection point of the rigid floater and the flexible element shifts downwards.

In all designs the goal is to get a matching tower's first bending natural frequency, but not necessarily a match in mode shape. With the focus put on the natural frequency, the method introduced in section 3.1.7 is applied. A match in natural frequency is achieved by altering the Young's modulus. In order to make this process efficient and fast for a big variety of designs, a Python script was written.

A *while loop* was implemented in Python, which loads a general OrcaFlex model with a FOWT using a rigid floater and a general configuration of the flexible element already set up. Following this, the properties of the flexible element are changed, and the first tower bending natural frequency is calculated. While the tower's first bending natural frequency is below the target, the Young's modulus is increased in small steps. Only after a match is achieved between them is a working design found. This iterative process is visualised in Figure 3.19. This *while* loop process is used throughout the whole thesis in order to generate flexible element designs with a matching tower first bending natural frequency.

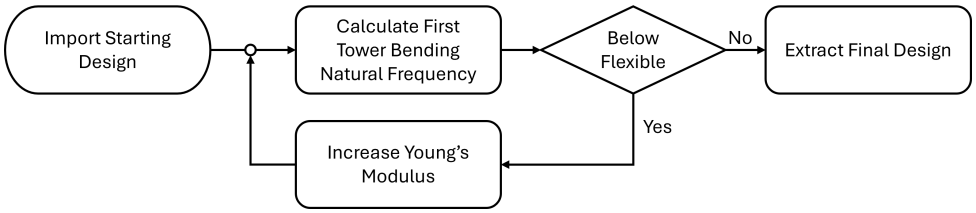

Figure 3.19: Iterative process of finding a design with a matching tower first bending natural frequency compared to the flexible floater design.

3.2.2 Create Variations of Designs (B2 M)

Different designs are created in order to investigate the impact of different properties of the flexible element on the tower mode shape. Three different approaches are chosen. The first one checks total line length variation. The second one the impact of segment length of the flexible element, and the last one the impact of having one stiffer and one less stiff element.

The total flexible element length variation was performed for the following lengths: 0.5 m, 2.5 m, 5.0 m, 7.5 m and 10.0 m, as visualised in Figure 3.20a. The flexible element shall not be underwater at any point since this could introduce unwanted buoyancy effects. The clearance between the tower and SWL is 15 m in the design position. With heavy motion and oncoming waves, a safety margin of 5 m is added. Hence, 10.0 m total length is the upper limit.

The line segmentation study was performed for all total length possibilities. The line segment sizes are equal to the steps of total length, meaning that the segment length can be 0.5 m, 2.5 m, 5.0 m or 10.0 m. The resulting combinations of the first two approaches are visualised in Figure 3.20b. For a total length of 10 m, for example, four variations exist, which consist of 20, 4, 2 and 1 segments.

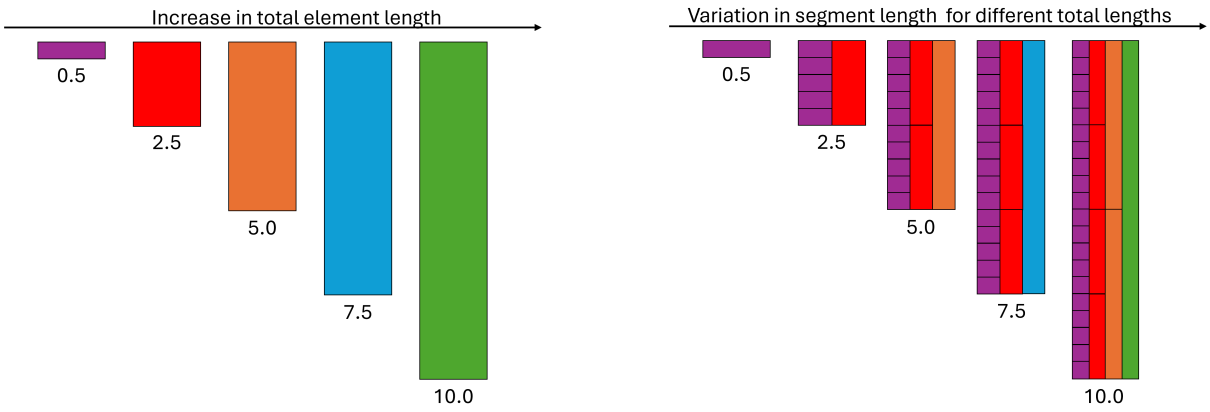

(a) Variation of total length of the flexible element.

(b) Variation of segment length for different total lengths.

Figure 3.20: Length variations in the flexible element and its segments.

An additional approach is to use one stiffer (hard) and one less stiff flexible element (soft) combined within one configuration. The definition of 'more' and 'less' stiff is that the stiffer element is 10 times the stiffness of the less stiff element. The position of the two was also varied, meaning that either the hard element is connected to the tower (on top) and the soft one was connected to the floater (bottom) or vice versa. Other than that, the process was identical. The total length was varied, the ratio between the two was changed, and the Young's modulus was changed until a match in the tower's first bending natural frequency was achieved. For all ratios, only one segment was used for the hard component and for the soft component. The resulting designs for soft at the top and hard at the bottom are visualised in Figure 3.21. The same set of designs was created for hard at the top and soft at the bottom.

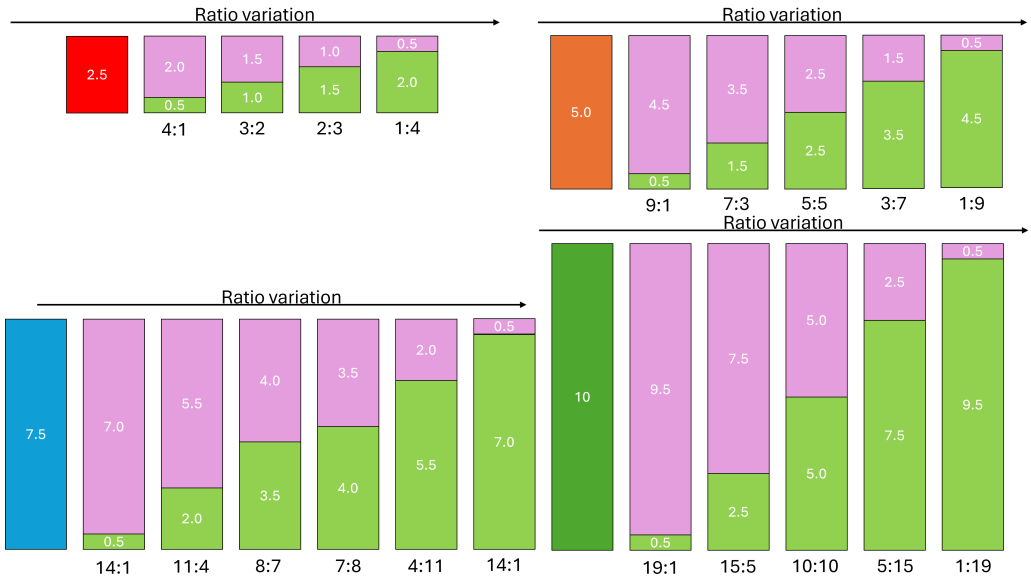

Figure 3.21: Variation of ratio between soft and hard flexible elements for different total lengths. Pink symbolises 'soft', whereas green symbolises 'hard' with a ten times larger Young's modulus.

3.3 Phase C: Effect of Tower Mode Shape Deviation

Lastly, **Phase C** investigates the **Effect of Tower Mode Shape Error** on the tower dynamics in the time domain under different Design Load Case (DLC)'s. Hence, a clear definition of the DLC's and **Tower Dynamics** is needed. An overview of the methodology steps is provided in Figure 3.22.

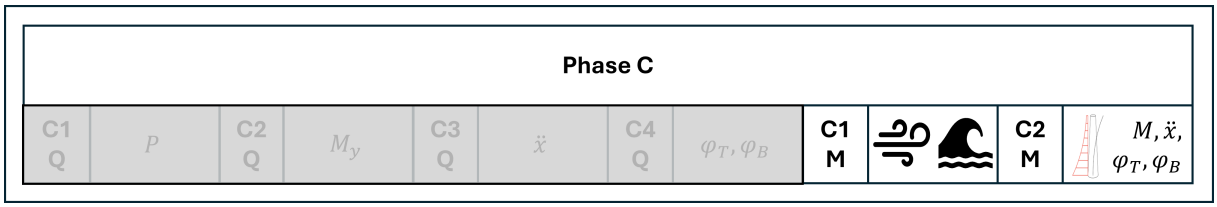

.

Figure 3.22: Overview highlighting the research plan for this section. Grey highlighted questions are discussed in chapter 4

3.3.1 Design Load Cases (C1 M)

The dynamic analysis was performed in the time domain under environmental conditions defined in this section. In general, increasing steps of complexity were tested and used to investigate different behaviours as well as sensitivities towards the different environmental impacts. All environmental conditions were performed with the key parameters from Allen et al., 2020 load case 1.1. This data is summarised in Table 3.7.

Table 3.7: Environmental conditions for DLC with NTM wind condition.

Wind Condition	Hub Height Wind Speed [m/s]	Wind Headings [°]	Significant Wave Height [m]	Peak Period [s]	Gamma Shape Factor [-]	Wave Headings [°]
NTM	4.00	0.00	1.10	8.52	1.00	0.00
	6.00	0.00	1.18	8.31	1.00	0.00
	8.00	0.00	1.32	8.01	1.00	0.00
	10.00	0.00	1.54	7.65	1.00	0.00
	12.00	0.00	1.84	7.44	1.00	0.00
	14.00	0.00	2.19	7.46	1.00	0.00
	16.00	0.00	2.60	7.61	1.35	0.00
	18.00	0.00	3.06	8.05	1.59	0.00
	20.00	0.00	3.62	8.52	1.82	0.00
	22.00	0.00	4.03	8.99	1.82	0.00
	24.00	0.00	4.52	9.45	1.89	0.00

Constant Wind

The first step of complexity was constant wind without any other environmental loads. The wind speed was chosen according to the wind speeds in Table 3.7. A total simulation time of 1000 seconds was chosen, with a transient of 400 seconds, consisting of a 300 seconds ramp-up and 100 seconds of constant wind. The last 600 seconds were used as 10-minute data.

Turbulent Wind

In the next step, turbulent wind with a Normal Turbulence Model (NTM) according to Commission, 2019 was included. OrcaFlex requires a *.bin* file for each wind direction (u, v and w). Additionally, it requires information about the grid, mean wind speed, target standard deviation and wind origin. The *.bin* files were created as Mann turbulent wind fields in BHawc, a Siemens Gamesa in-house program. This required the definition of the following parameters.

Firstly, the wind field's dimensions had to be defined, as shown in Figure 3.23. The height and width (global y and z directions) were determined according to the turbine diameter. In this case, 240 m. The depth of the wind field (x-direction) depends on the mean wind speed. For a total simulation length of 1000 seconds with a mean wind speed of, for example, 10 m/s, the wind field requires a length of 10 km. Additionally, to the length, the amount of grid points had to be determined. These values were chosen on recommendation of experienced colleagues. Due to historical reasons in the calculation method of the wind fields, the number of grid points is reported to the power of 2. With the outer dimension and amount of grid points defined, the distance between points was calculated, which is a required OrcaFlex input.

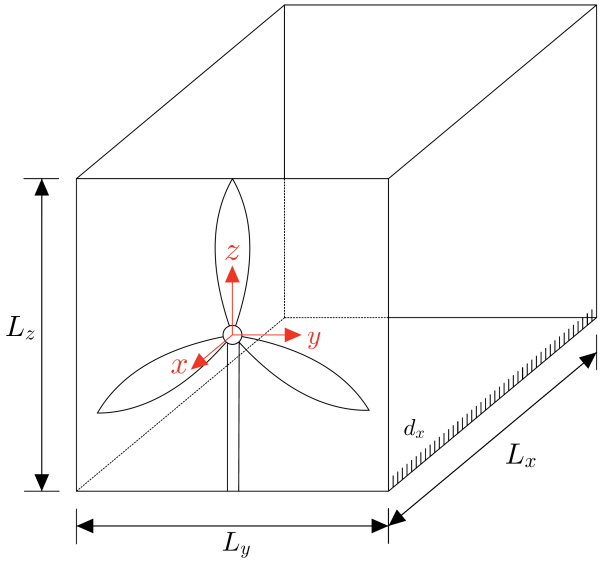

Figure 3.23: Example of wind field for arbitrary wind turbine, defining the dimensions of the field.

Next to the definition of the wind field, information about the strength of turbulence had to be defined. According to Commission, 2019 the length scale parameter l is found as:

$$l = 0.8 * \Lambda_1 \tag{3.7}$$

Λ_1 is the longitudinal turbulence parameter and depends on the hub height. For turbines with a hub height larger than 60 m, Λ_1 is defined as 42 m. Commission, 2019 also defines the non-dimensional shear distortion parameter Γ as 3.9 m. These two parameters are wind turbine specific but do not change with the wind speed. $\alpha\epsilon$ on the other hand, depends on the wind speed and is best calculated with Equation 3.8 (Mann, 1994 and Nybø et al., 2021).

$$\alpha\epsilon^{2/3} = \frac{55}{18} \cdot 0.4754 \cdot \sigma_{iso}^2 \cdot l^{-2/3} \tag{3.8}$$

The un-sheared, isotropic variance σ_{iso}^2 was calculated using the standard deviation in mean wind direction σ_1 with the relation:

$$\sigma_{iso} = 0.55 \cdot \sigma_1 \tag{3.9}$$

The standard deviation in mean wind direction was found in Commission, 2019 as:

$$\sigma_1 = I_{Ref} \cdot (0.75 \cdot v_{hub} + b) \tag{3.10}$$

b is a constant defined as 5.6 m/s and I_{Ref} depends on the wind turbine class, which is class B in this case, defining I_{Ref} as 0.14.

With that, all required variables were determined for different wind speeds to create the turbulent wind fields in BHawc and input them into OrcaWave. An example time series for a turbulent wind speed with a mean of 20 m/s is shown in Figure 3.24. The wind speed was ramped up for the first 100 seconds. This is visualised through the grey area in Figure 3.24.

Additionally, the spectrum of the wind speed after ramp-up was determined. The spectrum is defined as the Fourier transform of the covariance function of the underlying process and is also called PSD (Muskulus, 2023). The wind spectrum and all following spectra are positively defined double-sided spectra.

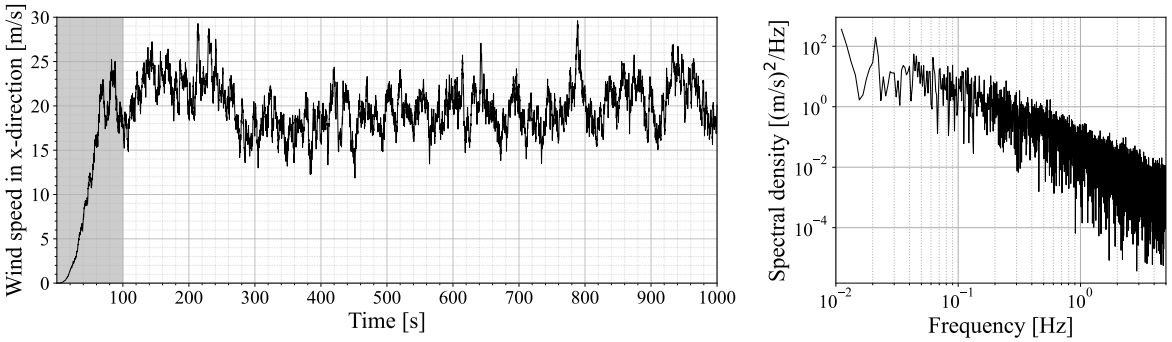

Figure 3.24: Turbulent wind time series and corresponding positively defined double-sided spectrum.

The mean wind was only determined for the time after ramp-up. The mean was calculated as 19.91 m/s. It is not equal to 20 m/s due to the fact that not the whole time series of 1000 seconds was considered. Neglecting the transient phase results in a short time series with a different mean wind speed.

The standard deviation shown in Figure 3.24 was calculated as the square root of two times the area under the spectrum. The target standard deviation in the x-direction is 2.87 m/s, compared to the calculated value of 2.71 m/s. This difference is a consequence of the reduced time series.

For the case with 22 m/s and 24 m/s, the turbine performed a rotor shutdown. The OrcaFlex documentation of the controller states that for a blade pitch angle higher than 20°, shutdown mode is activated (Ross and McKinnon, 2018). The controller feathers the blades to 90°, reducing the lift force and stopping the rotor. The controller is operated with a *.dll* file that can't be easily modified. Since the controller is not in the scope of the thesis, the file was not adjusted.

Non-producing states, including rotor shut-down, are not of interest. Hence, the cases of 22 m/s and 24 m/s turbulent wind were omitted, and 20 m/s was used as the highest wind speed case.

Regular Waves

The next step of complexity is the inclusion of waves, however, without any wind. In the first step, regular waves were used, using the Airy waves. The wave height and corresponding wave period were chosen according to Table 3.7.

Iregular Waves

Following, irregular waves were modelled. Hs, Tp and γ from Table 3.7 were used to create a JONSWAP spectrum in OrcaFlex. The spectrum's range is defined using a relative frequency minimum (r_{min}) and relative frequency maximum (r_{max}). For a single peak spectrum, as the JONSWAP spectrum is one, the range is defined as $f_{min} = f_p \cdot r_{min}$ and the max as $f_{max} = f_p \cdot r_{max}$. This is done, as the so-called equal-area approach that guarantees an identical amount of energy per wave component can otherwise result in very wide bins for frequencies with low energy (typically near the tails). For the first entry of Table 3.7 a time series of the water level was created. This and the resulting spectrum are shown in Figure 3.25.

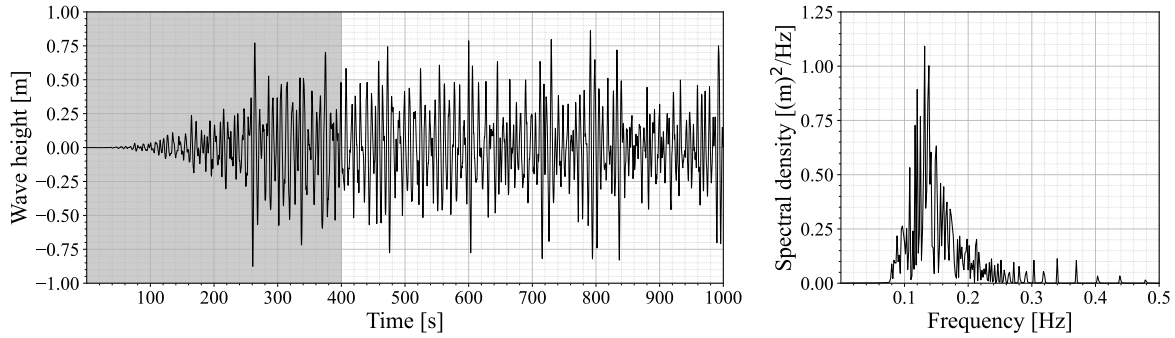

Figure 3.25: Irregular wave time series and corresponding positively defined double-sided spectrum.

In the case of the irregular waves, the first 400 seconds were taken as ramp-up. The mean and spectrum were only calculated for the time series after ramp-up. The mean value from the time series was approximately 0 m, which is to be expected.

The standard deviation was 0.273 m and was again found as the square root of twice the area under the spectrum. Multiplying the standard deviation by four gives an estimate of the significant wave height:

$$H_s = 4 \cdot 0.273 \text{ m} = 1.08 \approx 1.1 \text{ m} \tag{3.11}$$

The peak period was simply found as $1/f_p$, where the peak frequency is the frequency at the peak of the spectrum. With $f_p = 0.132$ Hz the peak period was found as $T_p = 7.60$ s, which is off from the desired 8.52 s. This difference is also expected to stem from the reduced time series.

Full DLC

Lastly, a full Design Load Case was simulated. More specifically, DLC 1.1 from Allen et al., 2020 with turbulent wind using Mann wind fields created through BHawc, and irregular waves defined by the JONSWAP spectrum. In this case, as in all others, a total simulation of 1000 seconds was chosen, with 400 seconds transient that were disregarded and 600 seconds of data.

3.3.2 Tower dynamics (C2 M)

Goal of the thesis is to investigate the impact of different tower mode shapes on the tower dynamics. This requires a clear definition of what tower dynamics should be compared.

The most obvious choice is to compare the bending of the tower in fore-aft, so bending around the global y-axis. A time series is available for each node, allowing spectral analysis as well as bending profiles along tower height. The tower bending is important, as this determines the loads on the primary structure, so on the tower itself. These can be design-driving. An overestimation leads to too conventional designs with too much material and hence too high cost. Underestimating the loads, on the other hand, can result in unexpected failure.

Furthermore, the acceleration of the tower was tracked. Again, a time series of each node is available. The acceleration is primarily important for secondary structures, so anything attached to the tower, like, for example, platforms.

Lastly, the tilt of the nacelle and node at tower root were checked. Siemens Gamesa, as a turbine manufacturer, has a special interest in correct modelling of nacelle tilt.

Chapter 4

Results and discussion

4.1 Phase A: Flexible and Rigid Floater

Firstly, the remaining research questions from Phase A are investigated and the results discussed. The first step is to **Compare Methods to Identify Tower Modes in the Multibody System Floating Offshore Wind Turbine**. Following that, the results of using a rigid floater are compared to using a flexible floater by comparing the **Differences in Tower Natural Frequency between Fully Flexible Floater Model and Fully Rigid Floater Model** and the **Differences in Tower Mode Shape between Fully Flexible Floater Model and Fully Rigid Floater Model**. An overview of the discussed topics is provided in Figure 4.1.

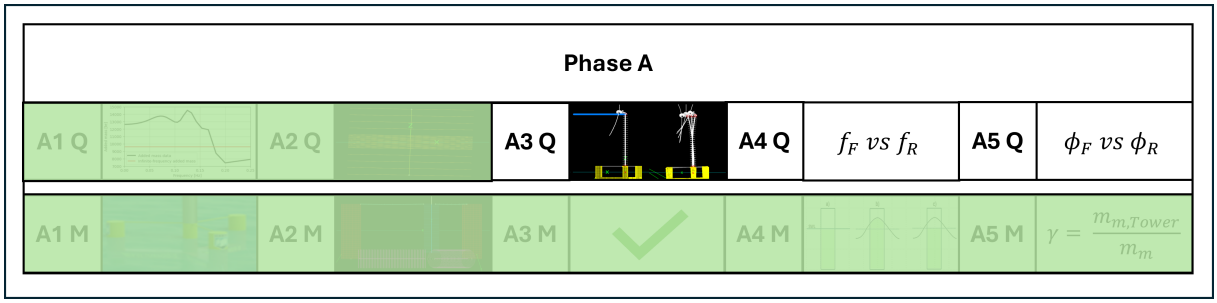

Figure 4.1: Overview highlighting the research plan for this section. Green highlighted questions were discussed in chapter 3.

4.1.1 Compare Methods to Identify Tower Modes in the Multibody System Floating Offshore Wind Turbine (A3 Q)

In accordance with subsection 3.1.6 the tower's first bending mode shape was identified using the adjusted *modal analysis* tool. In the following, the results are presented in comparison to time decay tests that were performed for both the flexible and rigid model.

Using the 'mode participation' method, the mode in which the tower dominates most (except for rigid body motions) was found to be at 0.408 Hz for the flexible floater design and at 0.451 Hz for the rigid floater design. Performing a decay test results in the time domain and spectrum shown in Figure 4.2. The peak in the frequency spectrum was found to be at 0.41 Hz for the flexible floater design and at 0.44 Hz for the rigid floater design. The first 75 seconds of the decay process were used

to create the PSD. The first peak resembles the pitch natural frequency, the second peak the different tower first bending natural frequencies, and the third peak shows coupling with other components that also result in tower bending.

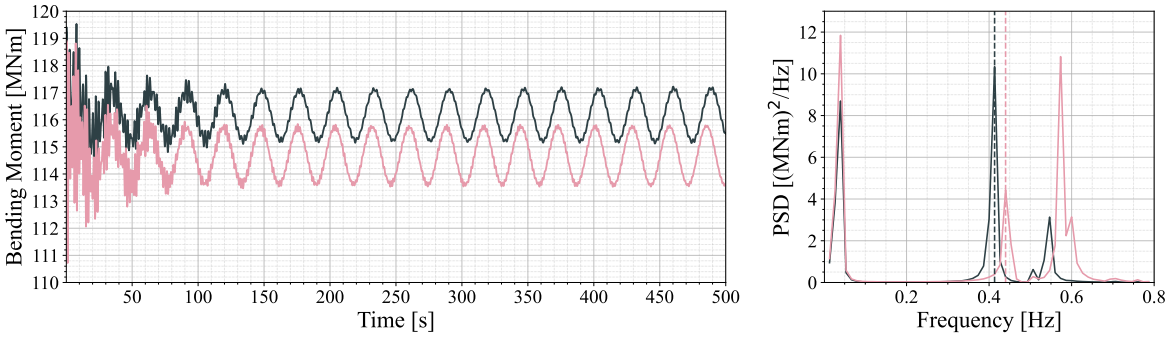

Figure 4.2: Time domain of decay test showing tower bending at root. Corresponding spectrum only includes values within the first 75 seconds.

Comparing the findings, one can see slight differences between the results of the two freqeuncy identification methods. They are in general considered small and possibly stem from the fact that the decay test considered non-linear effects and damping and, furthermore, that the resolution of the PSD is limited to the length of the observed time span. Observing a longer time span would increase the resolution, but at the same time, the relatively high structural damping would cause the tower bending to die out, resulting in less significance to the tower motion. The agreement within 2.5% gives good ground for confirmation of both methods, as they independently reach the same results.

4.1.2 Differences in Tower Natural Frequency between Fully Flexible Floater Model and Fully Rigid Floater Model (A4 Q)

In the next step the identified first tower bending natural frequency of the flexible and rigid cases are compared to each other in Table 4.1. They are furthermore compared to results from literature that used similar setups in section A.5.

Table 4.1: Tower first bending natural frequency of flexible floater compared to rigid floater case.

Flexible Floater	Rigid Floater
0.408 Hz	0.451 Hz

The first tower natural bending frequency increases for the rigid floater over the flexible floater case. This behaviour is to be expected, as the rigid floater is stiffer than the flexible floater. The increase in stiffness leads to an increase in the frequency as given in Equation 2.9.

4.1.3 Differences in Tower Mode Shape between Fully Flexible Floater Model and Fully Rigid Floater Model (A5 Q)

Figure 4.3 visualizes the tower mode shape of the flexible floater and rigid floater design allowing to compare them to each other.

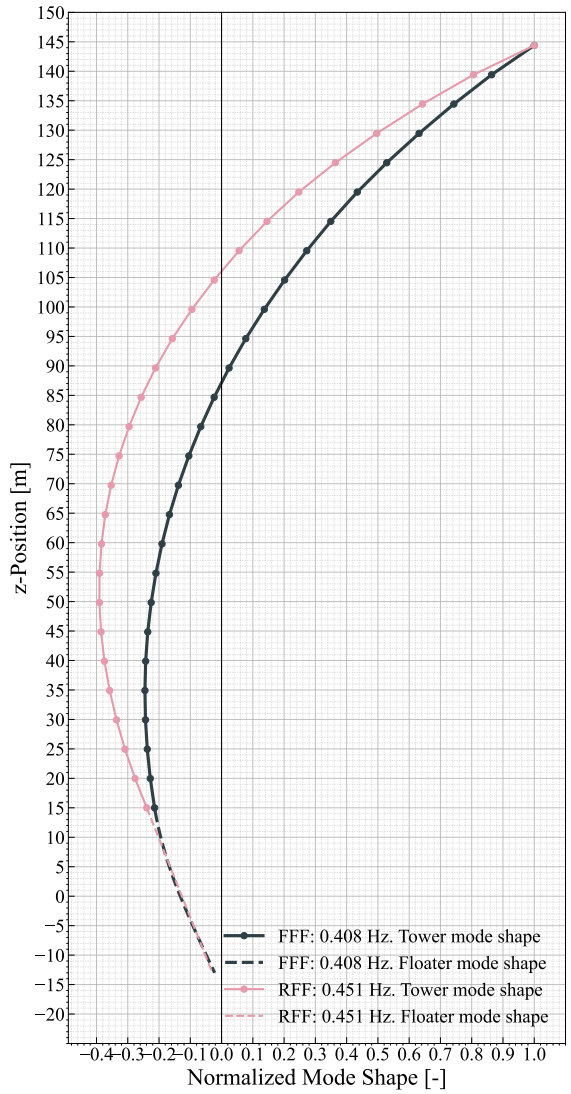

Figure 4.3: Mode shape of flexible floater design compared to rigid floater design.

The mode shapes are normalised according to the max tower displacement. Hence, both cases have a tower top displacement of 1, as is typical for a first tower bending mode shape.

Both modes are closer to the case of a free-free beam or pined-free beam rather than a clamped-free beam (as is the case of bottom fixed wind turbines). This observation does not change between rigid and flexible floater design. However, comparing the tower root it can be seen that the rigid floater shows more lateral displacement and also more rotation. This matches the observation from Harger et al., 2023.

The flexible floater has its mass and stiffness attributes distributed over the nodes. This allows the flexible floater to have displacement of single nodes through bending, which is visible as the black dashed line in Figure 4.3 shows a continuous bend curve. The rigid floater, on the other hand, has all its mass properties constrained to one single point. Hence, it can only perform rigid body motions, with the rigid floater visualised as the dashed straight line.

In terms of energy this can be explained as follows: The rigid floater can only store kinetic energy. The flexible floater, on the other hand, additionally captures bending and hence includes strain energy. Thus, less kinetic energy in the form of translational and rotational motion is required to reach the same energy level.

4.2 Phase B: Flexible Element Design Study

The research question for Phase B is the investigation of the influence of flexible element design on the tower mode shape. This is investigated by first focusing on the **Influence of Flexible Element Length on the Tower Mode Shape**, then the **Influence of Flexible Element Segmentation on the Tower Mode Shape** and lastly the **Influence of Flexible Element Composition on the Tower Mode Shape**. These steps are summarised in Figure 4.4.

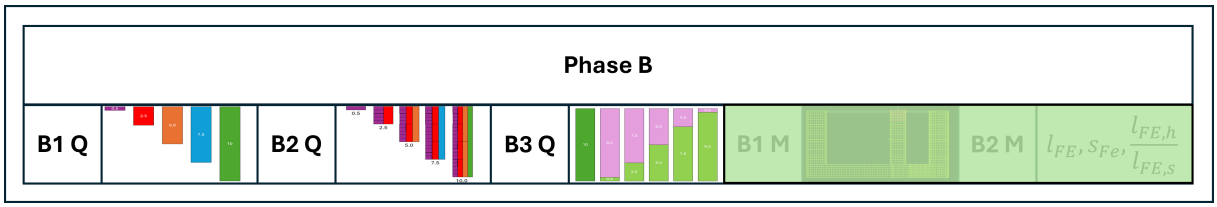

Figure 4.4: Overview highlighting the research plan for this section. Green highlighted questions are discussed in chapter 3.

4.2.1 Influence of Flexible Element Length on the Tower Mode Shape (B1 Q)

After implementing the flexible element as stated in subsection 3.2.1 one can start altering the properties of the flexible element. The first, obvious step is to change the total length of the flexible element. The resulting mode shapes for a total length of 0.5 m, 2.5 m, 5.0 m, 7.5 m and eventually 10.0 m are displayed in Figure 4.5a, with the natural frequency reported for all designs at 0.408 Hz, which matches the flexible floater design as intended.

Firstly, the focus is put on the changes made to the flexible element in order to get a matching first tower bending natural frequency over a changing element length. The properties of the flexible element over the different total lengths are summarized in Table 4.2. The Young's modulus as reported in Table 4.2 is found to increase with an increase in total length of the flexible element to maintain a constant total bending stiffness (Equation 4.1).

$$\begin{aligned} k &= \frac{EI}{L} \\ I &= \frac{\pi}{64}\left(D_o^4 - D_i^4\right) \end{aligned} \tag{4.1}$$

Table 4.2: Variation of Young's modulus and MAC number of flexible element over increasing flexible element length.

L [m]	E [GPa]	MAC [-]
0.5	3.1	0.9966
2.5	15.6	0.9974
5.0	31.6	0.9983
7.5	48.0	0.9990
10.0	64.8	0.9995

The MAC number reported in Table 4.2 is used as a quantitive measure to compare the different designs. A clear trend is visible, where a higher MAC number (and hence better match compared to the flexible floater designs' tower mode shape) is achieved with an increasing total length of the flexible element.

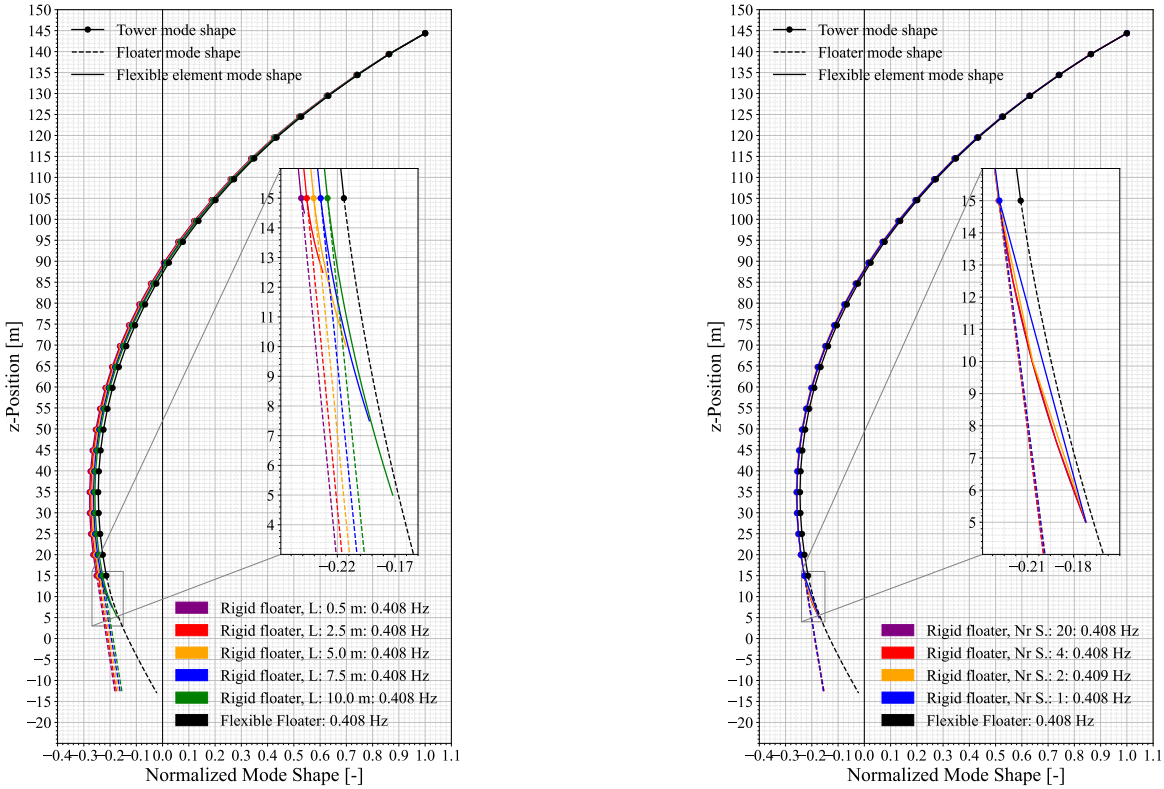

(a) Mode shape of flexible element designs with varying total length.

(b) Mode shape of flexible element design with varying number of segments.

Figure 4.5: Mode shapes for total length and amount of segments variation.

This better match in the MAC number comes with a better match in the horizontal position of the tower root node, as can be seen in Figure 4.5a.

In comparison to the mode shape of the rigid floater design, all flexible element designs show less rotation of the tower bottom node, and less horizontal displacement. With increasing length of the flexible element the match in horizontal position and tower bottom rotation improves further. This leads to the finding that a longer flexible element results in a better match of the tower first bending mode shape.

Explaining the observation in terms of energy, the change over element length can be explained as follows. The additional strain energy due to the flexibility of the centre column depends on the volume of the body (Gavin, 2012). Hence, the advantage of using a longer flexible element over a shorter one stems from the fact that a longer flexible element can store more strain energy. Less kinetic energy is required, resulting in a reduction in rigid body motions and a better match of mode shapes.

4.2.2 Influence of Flexible Element Segmentation on the Tower Mode Shape (B2 Q)

The results from the previous subsection suggest that longer elements result in a better match of the mode shape. Due to this finding the following section solely presents flexible element designs with a total length of 10 m. The mode shapes of flexible elements with a different total lengths over different segmentation length, as described in subsection 3.2.2, are summarised in section A.6.

The mode shapes for a total element length of 10 m with variation in the number of segments are shown in Figure 4.5b, as well as the natural first tower bending frequency, which matches the flexible floater design in all cases. The underlying properties of each designs' flexible element and the MAC number when compared to the flexible floater design are summarised in Table 4.3.

Table 4.3: Variation of Young's modulus and MAC number over changing number of segments.

Nr Segments [-]	E [GPa]	MAC [-]
20	64.3	0.9995
4	64.3	0.9995
2	66.0	0.9993
1	65.0	0.9995

The variations in the MAC number are expected to stem from the fluctuation in Young's modulus which was determined by the *while loop* explained in subsection 3.2.1. The results for the other total element lengths, shown in section A.6, support this finding.

Figure 4.5b shows a clearly improved flexible floater mode shape for the case with more segments compared to the flexible floater, as the curved shape of the floater is captured better. However, the position of tower root and the end point of the rigid floater are identical. Combined with the observed constant MAC number, this indicates that the accuracy of the first tower bending mode shape does not depend on the number of segments used in the flexible element but on the Young's modulus. All designs in the close range of 64.3 GPa to 65.0 GPa show the same MAC number, whereas the outlier with 66.0 GPa has a worse performance considering the MAC number.

OrcaFlex does not use Hermite shape functions of second order or higher to capture the shape of a single segment. If that had been the case, one element would have already been sufficient to capture the quadratic or maximal cubic shape of the tower's first bending mode. Instead, OrcaFlex

models each connecting segment between nodes as a straight line. As explained in subsection 2.8.1 the bending stiffness is captured by rotational spring dampers at each end of the segment, between segment and node. Hence, it is concluded that the accuracy of the flexible elements' mode shape, and thus the amount of segments used for the flexible element, does not influence the accuracy of the tower mode shape.

4.2.3 Influence of Flexible Element Composition on the Tower Mode Shape (B3 Q)

In the last step, multiple designs consisting of two elements of different Young's modulus were created according to subsection 3.2.2. Again, only the cases with a total length of 10 m are discussed. The other cases are shown in section A.7. The mode shapes of the different designs, for both soft-hard and hard-soft, are shown in Figure 4.6.

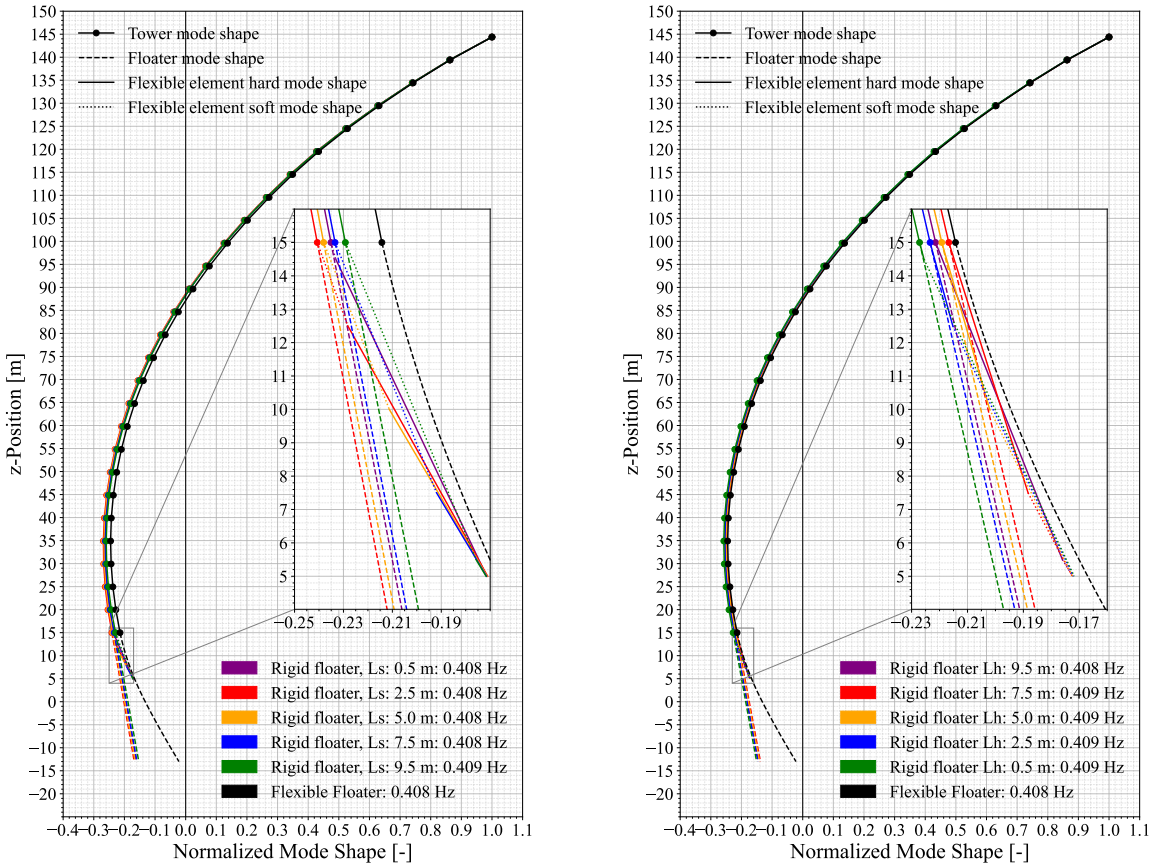

(a) Soft-Hard configuration. **(b)** Hard-Soft configuration.

Figure 4.6: Mode shape of flexible element designs with varying stiffness ratio.

The underlying values as well as the resulting MAC number of both designs are shown in Table 4.4

and Table 4.5.

In the case of the hard-soft design, the case with a 7.5 m long hard segment, 2.5 m long soft segment and a Young's modulus of 220 for the hard segment has the highest MAC number. It is generally found, that flexible element designs where the hard segment has a Young's modulus close to 200 GPa perform best.

The same finding is made for the soft-hard design, where the soft design is connected to the tower. The closer the Young's modulus of the soft segment to 200 GPa the higher the MAC number. The only exception to this is the design with a 9.5 m long hard segment. It is assumed that in this design the hard segment dominates and with a Young's modulus of close o 200 GPa results in the high MAC number.

The tower and centre column both have a Young's modulus of 200 GPa. It is hence expected that those designs perform best, where the Young's modulus of the segment that is connected to the tower is close to that value.

Table 4.4: Variation of Young's modulus and MAC number over changing ratio between soft and hard.

L_h [m]	L_s [m]	E_h [GPa]	E_s [GPa]	MAC [-]
9.5	0.5	93	9.3	0.9988
7.5	2.5	206	20.6	0.9982
5.0	5.0	351	35.1	0.9985
2.5	7.5	501	50.1	0.9989
0.5	9.5	628	62.8	0.9992

Table 4.5: Variation of Young's modulus and MAC number over changing ratio between hard and soft.

L_h [m]	L_s [m]	E_h [GPa]	E_s [GPa]	MAC [-]
9.5	0.5	95	9.5	0.9998
7.5	2.5	220	22.0	0.9999
5.0	5.0	370	37.0	0.9998
2.5	7.5	516	51.6	0.9996
0.5	9.5	631	63.1	0.9994

4.2.4 Improved design

Using the findings from the previous parameter sensitivity studies, an improved design was created. This design has a total length of 10 m and two segments with different Young's moduli. The segment directly connected to the tower has a Young's modulus of 200 GPa and is considered the hard segment. The length of this segment is chosen to be 9.5 m in order to be as dominant as possible. The segment with a remaining length of 0.5 m is regarded as the soft segment and its Young's modulus is found with the *while loop*. Furthermore, a smaller step size was used when altering the Young's modulus in the *while loop* to match the tower's natural frequency more accurately.

The resulting mode shape is shown in Figure 4.7a, and the underlying values as well as the resulting MAC number are reported in Table 4.6.

Table 4.6: Parameters and resulting MAC number of improved design.

L_h [m]	L_s [m]	E_h [GPa]	E_s [GPa]	k [GNm]	MAC [-]
9.5	0.5	200	4.9	230.04	1.0000

The MAC number reported in Table 4.6 shows an even better match between the mode shapes and implies that the findings have been correctly identified and also correctly implemented. Before confirming this the assumption that a match in Young's modulus is desired needs to be tested.

The second moment of area is constant for all flexible element designs, and furthermore matches the second moment of area of the centre column of the flexible floater. Hence, the good match could also stem from an identical product of Young's modulus (E) and second moment of area (I), rather than solely a match of Young's modulus.

This is tested by looking at the Improved design. The second moment of area is changed by changing the inner diameter to 9.5 m yielding $I = 91.054m^4$. The Young's modulus of the hard segment is kept at 200 GPa, and the one of the soft segment is again changed in a *while loop* until a match of tower first bending natural frequency is achieved.

Figure 4.7b shows the resulting mode shape, with the MAC number reported up to the sixth digit in Table 4.7, indicated by the letter 'I'. A slight difference can be seen between the results, indicating that not only the Young's modulus needs to be match, but the product of Young's modulus and second moment of area.

The initial cases' product of EI is found as: $EI = 34.4\ \text{m}^4 \cdot 200\ \text{GPa} = 6.88 * 10^{12}\ \text{Nm}^2$. In a next step this value is kept constant. Together with the new second moment of area of $I = 91.054\ \text{m}^4$ a new Young's modulus of $E = 75.56$ GPa is determined. This case is also tested and compared to the others in Figure 4.7b and Table 4.7 indicated as 'EI'.

The match of the MAC number as well as the visual comparison show a better match and support the assumption that not solely the Young's modulus of the centre column needs to be matched but instead the product of Young's modulus and second moment of area.

Table 4.7: MAC number of Improved design with no changes (E), Improved design with different second moment of area (I) and Improved design with product of Young's modulus and second moment of area (EI) identical to the initial cases'.

Model Name	E	I	EI
MAC	0.999997	0.999972	0.999997

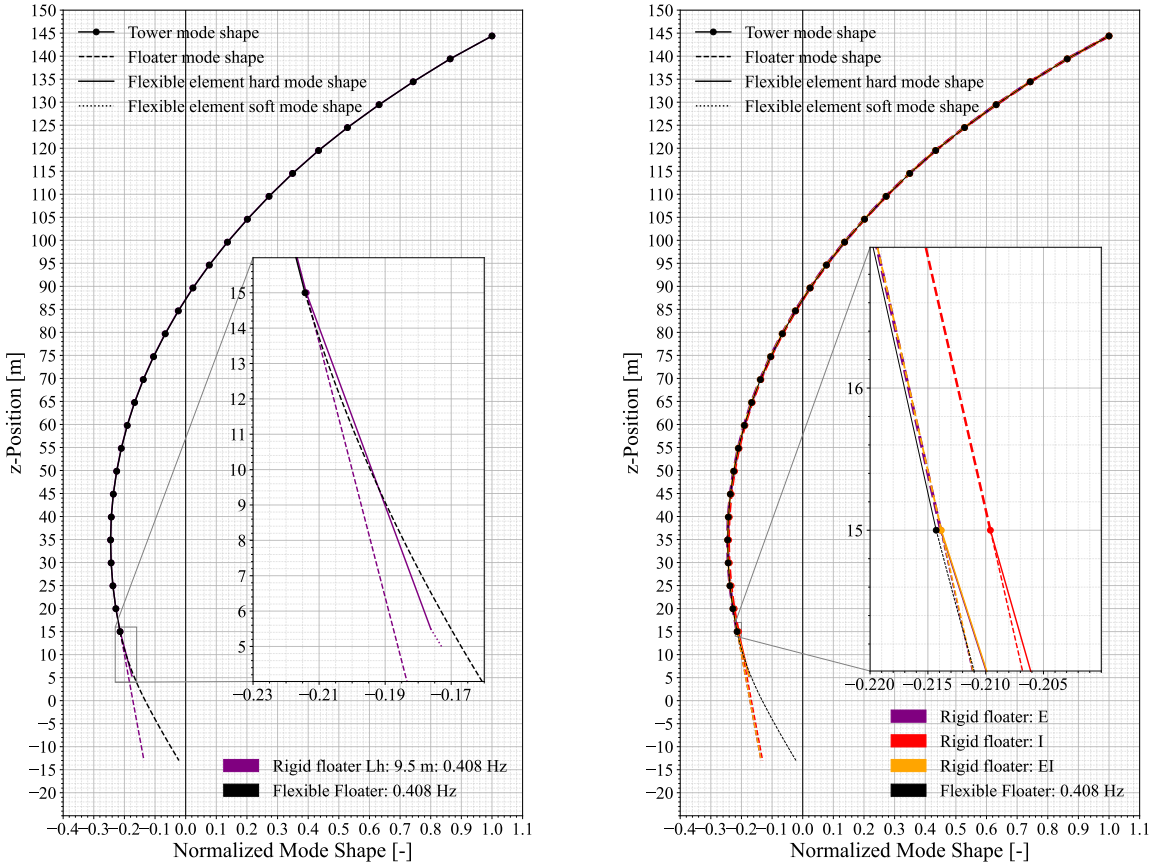

(a) Mode shape of the Improved design using the findings of the previous studies.

(b) Mode shape of the Improved design with no changes (E), different second moment of area (I), and product EI identical to the initial cases'.

Figure 4.7: Mode shape of the Improved design and sensitivity of Improved design towards EI.

The MAC number of 1 for the improved design gives ground to the conclusion that the sensitivity of the MAC number towards the different parameters were identified correctly. The following points are concluded:

- Increasing the length of the flexible element increases the MAC number.
- The MAC is insensitive to the number of segments.
- A product of Young's modulus and second moment of area close to the one of centre column for the segment connected to the tower increases the MAC number.
- The *while loop* step size needs to be decreased in order to get a more accurate match for the Young's modulus.

4.2.5 Selected designs

Investigating all possible designs would result in too much data. Hence, the most interesting and representative designs are chosen. A total number of 5 designs are chosen:

- **Short**: Flexible element of 0.5 m. This is the shortest and simplest design with the smallest MAC number.
- **Fine**: Flexible element of 10.0 m with 20 segments. The longest design possible, with the highest discretisations and hence complexity.
- **Coarse**: 10 m long flexible element with 1 single segment as a simplification of the fine case, but still a high MAC number.
- **Dual**: Flexible element consisting of two segments. One harder at the top and one softer at the bottom, as this gave the best initial match in mode shape.
- Improved: Improved design of flexible element applying the found dependencies. Two segments of different Young's modulus, where the top one is matching the flexible floaters Young's modulus. Included as it has the highest overall MAC number.

These 5 designs are shown in Figure 4.8 together with the flexible floater design. Additionally, Table 4.8 summarises the parameters of the selected design.

Table 4.8: Parameters and resulting MAC number of selected designs.

Name	$L(L_h/L_s)$ [m]	Nr Segments	$E(E_h/E_s)$ [GPa]]	k [GNm]	MAC [-]
Short	0.5	1	3.1	213.28	0.9966
Fine	10.0	20	64.3	221.19	0.9995
Coarse	10.0	1	65.0	223.60	0.9995
Dual	(7.5 / 2.5)	2	(220 / 22.0)	232.86	0.9999
Improved	(9.5 / 0.5)	2	(200 / 4.9)	230.04	1.0000

The differences in MAC number are also visible in Figure 4.8, where the Short design shows the biggest horizontal displacement. The Fine and Coarse designs tower root node positions are almost identical. This match is also observed for the overall tower mode shape. The Dual and Improved designs MAC numbers are closest to 1 suggesting a near perfect match with the flexible floater's first tower bending mode shape. The Improved design shows a slightly better match for the tower root node; however, this difference is hardly visible in the complete tower mode shape.

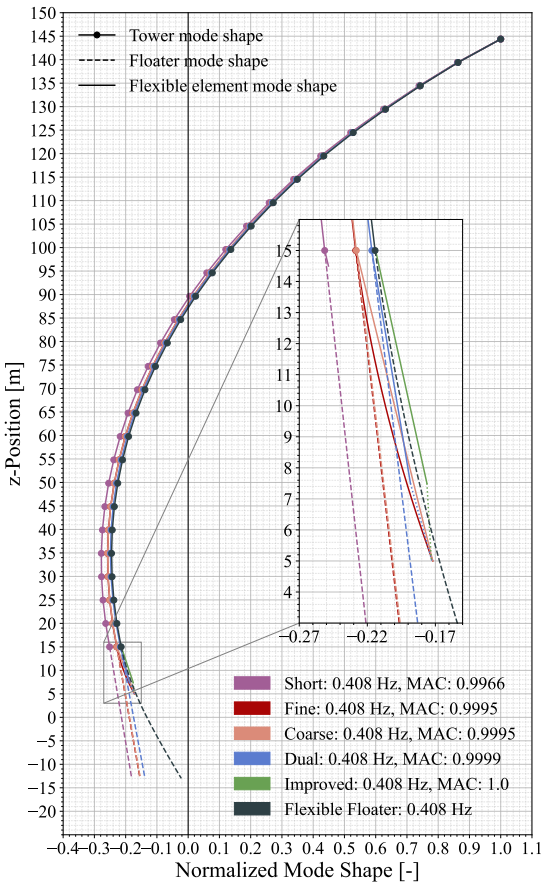

Figure 4.8: Mode shape of the selected flexible element designs and a flexible floater design.

4.3 Phase C: Effect of Tower Mode Shape Deviation

The last phase, Phase C, focuses on the performance of the different flexible elements in order to understand the effect of a mismatch in the tower mode shape on the tower dynamics in time domain simulations. This is investigated by answering the research question shown in Figure 4.9. Firstly, the **Influence of Tower Mode Shape Deviation on Tower Bending** is investigated. Next, the **Influence of Tower Mode Shape Deviation on Tower Acceleration** is studied, before lastly focusing on the **Influence of Tower Mode Shape Deviation on Tower Top and Root Rotation**.

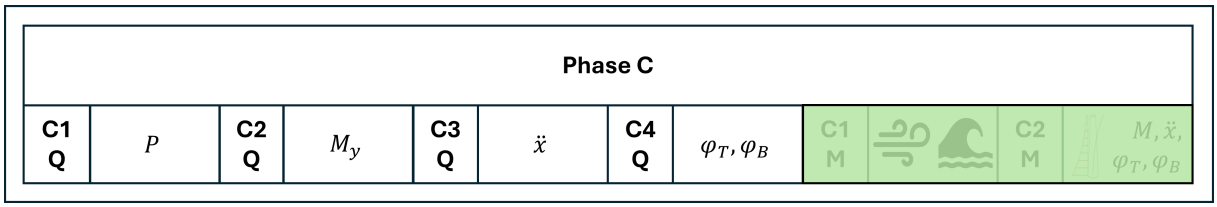

Figure 4.9: Overview highlighting the research plan for this section. Grey highlighted questions were discussed in chapter 3.

4.3.1 Influence of Tower Mode Shape Deviation on Decay Test (C1 Q)

Before looking at the tower dynamics, the influence of the flexible element on the overall performance is checked by performing a decay test at the example of subsection 3.1.6. Furthermore, the turbine performance, like the mean power production and mean thrust force for constant wind speeds are compared to the flexible floater case in section A.8.

The decay test from subsection 4.1.1 is repeated for all designs. The time series of tower root bending moment and the resulting spectrum using the first 75 seconds of the time series are summarised in Figure 4.10.

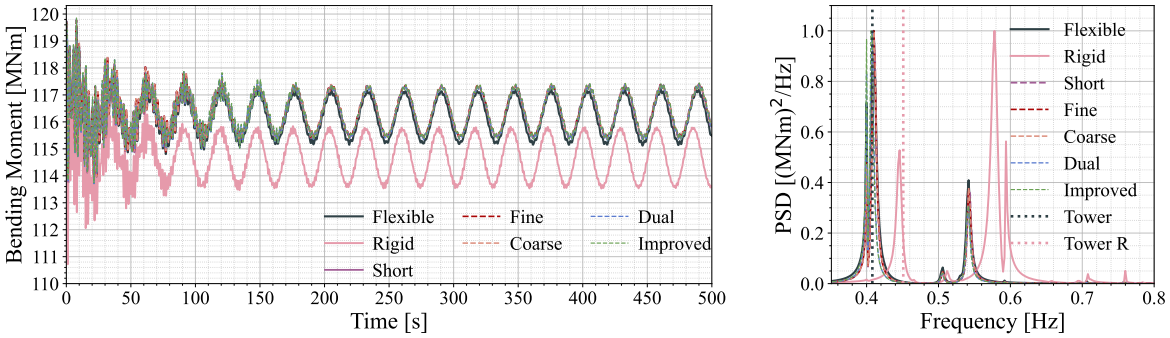

Figure 4.10: Time domain of decay test showing tower bending at root. Corresponding spectrum only includes values within the first 75 seconds.

The spectrum of the tower bending at root shows an overall good alignment between all peaks of the different flexible element designs and the flexible floater case. Especially when compared to the rigid case, a big improvement can be seen. This shows that the inclusion of a flexible element between tower and the rigid floater also improves the motions at frequencies other than the first tower bending frequency when decaying without any external environmental conditions.

Looking at the time domain results, one can see slight differences in the curves of the different designs and the flexible floater after the transient. They are not as big as for the rigid floater design but are still investigated, comparing the mean and standard deviation, omitting the first 100 seconds. The results are captured in Table 4.9.

Table 4.9: Mean and standard deviation of the flexible floater and of the different designs relative to the flexible floater. All taken after a transient of 100 seconds.

	Flexible [kNm]	**Rigid**	**Short**	**Fine**	**Coarse**	**Dual**	**Improved**
		[%] relative to Flexible					
mean	116.17	-1.29	0.18	0.19	0.19	0.16	0.19
std	0.67	12.37	-2.39	-2.78	-2.76	-1.18	-1.22

The results of the decay test using a rigid floater without a flexible element underpredict the loads by 1.29 %. Implementing a flexible element, no matter the configuration, already improves this difference to below 0.2 %. The differences between the different designs are minor. The best-performing design is the Dual design using one hard segment connected to tower and one soft connected to the floater. The worst-performing ones are the Fine, Coarse, and Improved designs. Without a clear pattern correlated to the MAC number and an overall small difference between the designs, it is concluded that the accuracy of the mode shape does not influence the mean tower bending moment in a decay test.

The standard deviation, on the other hand, shows bigger differences. The rigid floater design is off by 12.37 % and also the designs using a flexible element have differences of up to 2.8 % compared to the flexible floater design.

The Dual and Improved design have the best mode shape match and also show the smallest difference in standard deviation. This indicates that a close match in tower mode shape results in a good match of the bending moments standard deviation during a decay test.

No differences are found between the Fine and Coarse design. Since also no differences are identified between the mean values, it is concluded that the number of segments used for the flexible element does not influence the results of the bending moment during a decay test.

Having a deviation below 0.2 % in mean values and below 3 % in standard deviation when using a flexible element in a decay test shows that tuning the flexible elements properties to match the first tower bending frequency successfully improves the results.

4.3.2 Influence of Tower Mode Shape Deviation on Tower Bending (C2 Q)

The tower bending at tower root is looked at for the different designs for increasing complexity of environmental conditions, as explained in subsection 3.3.1.

Constant Wind

For the first case under constant wind the time series of the bending moment at tower root for a mean wind speed of 6 m/s and 10 m/s is looked at in order to get a better understanding of the dynamic behaviour. Figure 4.11a shows 600 seconds of data after the transient. Additionally, the spectrum of is shown in a log-log scale.

The time series shows a large oscillation, which, looking at the PSD, matches the surge natural freqeuncy in both cases. The excitation frequencies and energy contents when comparing designs using a flexible element and the flexible allign well. This includes the surge natural frequency and the blade passing frequency, as well as the harmonics of it.

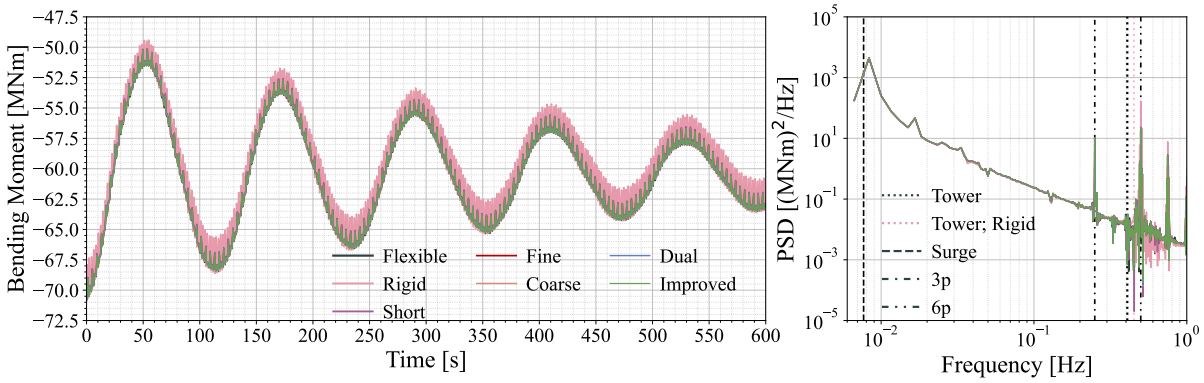

(a) Time series and spectrum of tower root bending for 6 m/s constant wind speed.

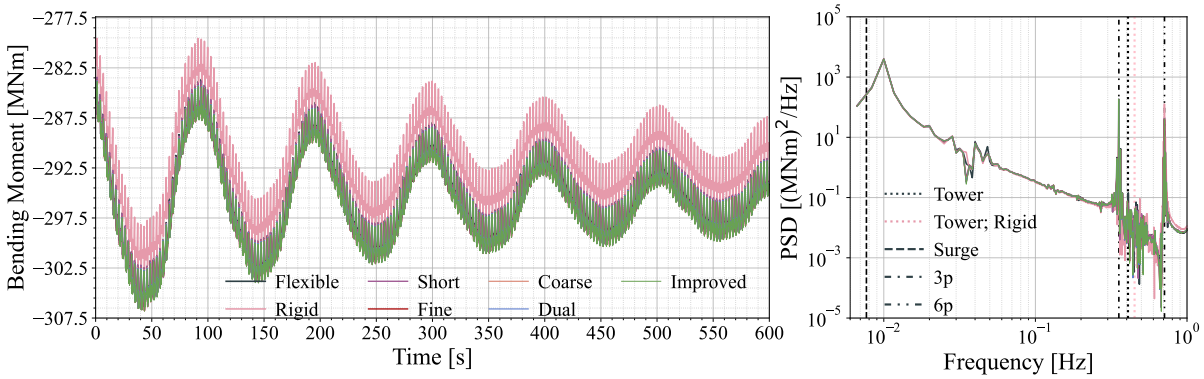

(b) Time series and spectrum of tower root bending for 10 m/s constant wind speed.

Figure 4.11: Time series of bending at tower root and corresponding spectrum in log-log scale for constant wind speeds.

An offset between the in *modal analysis* determined surge natural frequency and the position of the peak in the spectrum is seen. With constant wind, no free decay is taking place. The thrust force resulting from the turbine operating pushes the turbine into a steady offset position around which it oscillates. This offset increases the mooring line stiffness, which, as a result, increases the surge natural frequency.

The offset is larger with a wind speed of 10 m/s. Looking at Figure A.10d it can be seen that the thrust force is largest at rated wind speed. This peak in thrust force likewise results in a peak in surge amplitude (Figure A.10a), explaining the larger shift of the response frequency around the surge natural frequency.

Of most interest is the behaviour of the different designs around the tower's first bending natural frequency. Hence, Figure 4.12 focuses on the spectrum around the tower's first bending natural frequency of the flexible floater design and rigid floater design.

A clear peak can be seen in both cases at the first multiple of the blade passing frequency (6P). In both cases the rigid floater design shows higher energy contents than the other designs. The reason for this is that with 0.45 Hz the rigid floater tower bending natural frequency is closer to the excitation frequency.

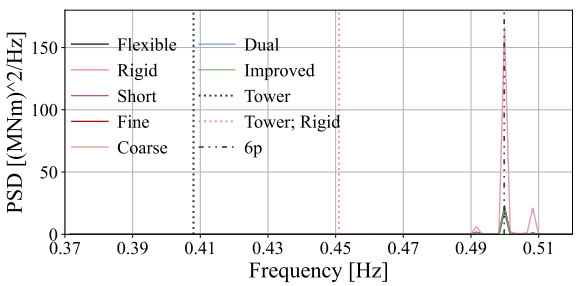

(a) Spectrum of tower root bending for 6 m/s constant wind speed with a focus on the range around the tower's first bending natural frequency.

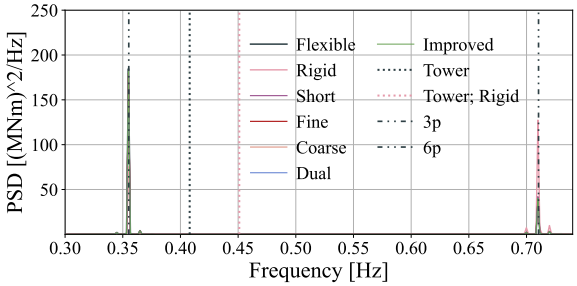

(b) Spectrum of tower root bending for 10 m/s constant wind speed with a focus on the range around the tower's first bending natural frequency.

Figure 4.12: Power spectral density (PSD) of tower bending moment for constant wind speeds.

Figure 4.12a additionally shows a clear peak at blade passing frequency (3P). This peak shows higher energy contents for the flexible element designs than the rigid floater design, as the tower natural frequency is closer to the 3P frequency, All designs show comparable energy contents, as they all have the same tower natural frequency. The change in 3P frequency between the two wind speeds stems from the increase in rotor speed with increasing wind speed.

A better match of the energy contents at the different peaks is found for all cases, and they all show improvement compared to the rigid case. This includes the surge natural frequency and the blade passing frequency as well as the multiples of it.

The time series of the bending moment is further analysed by looking at the mean and standard deviation. This is done for all wind speeds, not only 6 m/s and 10 m/s. The mean values are summarised in Table 4.10 and the standard deviation in Table 4.11. In order to better emphasise differences between the designs in comparison to the flexible floater design and each other, the values are given relative to the flexible floater.

Table 4.10: Mean of tower root bending for constant wind of the flexible floater and of the different designs relative to the flexible floater. All values were taken after a transient of 100 seconds.

wsp [m/s]	**Flexible** [MN]	**Rigid**	**Short**	**Fine**	**Coarse**	**Dual**	**Improved**
		[%] relative to Flexible					
4	42.92	-1.07	0.39	0.35	0.34	0.30	0.31
6	-60.51	-1.66	-0.23	-0.14	-0.14	-0.12	-0.09
8	-192.53	-1.43	-0.04	0.02	0.01	0.02	0.04
10	-295.73	-1.32	0.03	0.08	0.07	0.07	0.10
12	-269.56	-1.33	0.03	0.09	0.09	0.09	0.11
14	-223.28	-1.53	-0.02	0.03	0.02	0.02	0.05
16	-187.29	-1.57	-0.04	0.00	-0.00	0.00	0.03
18	-165.83	-1.59	-0.06	-0.02	-0.02	-0.02	0.01
20	-153.02	-1.61	-0.08	-0.05	-0.04	-0.04	-0.01
22	-146.06	-1.63	-0.09	-0.07	-0.06	-0.06	-0.03
24	-143.37	-1.65	-0.09	-0.07	-0.07	-0.07	-0.03

First of all, it is noted that all designs using a flexible element significantly outperform the rigid

floater design. Other than that, it can be seen that the relative difference decreases for higher wind speeds. Furthermore, the Short design outperforms all other designs for wind speeds close to rated. Outside this zone the longer flexible element designs perform better. However, all differences, except for the rigid floater design, are considered small. Hence, this does not allow for any conclusion on the impact of mode shape deviation on the tower dynamics.

Table 4.11: Standard deviation of tower root bending for constant wind of the flexible floater and of the different designs relative to the flexible floater. All values were taken after a transient of 100 seconds.

Wind speed [m/s]	**Flexible** [MN]	**Rigid**	**Short**	**Fine**	**Coarse**	**Dual**	**Improved**
		[% relative to Flexible]					
4	1.86	0.87	0.16	0.08	0.08	0.07	0.08
6	4.18	0.21	0.06	-0.15	-0.16	-0.16	-0.14
8	6.26	0.44	0.01	-0.25	-0.25	-0.25	-0.23
10	4.32	-1.09	0.19	-0.45	-0.46	-0.46	-0.41
12	3.12	-5.46	-1.70	-3.13	-3.18	-3.23	-2.95
14	4.41	-6.70	-1.10	-1.66	-1.70	-1.75	-1.49
16	3.78	-13.35	-0.90	-0.52	-0.61	-0.76	-0.20
18	3.91	-20.82	-1.16	-0.39	-0.54	-0.81	-0.01
20	4.20	-27.43	-1.37	-0.35	-0.53	-0.94	0.05
22	4.55	-32.60	-1.55	-0.40	-0.62	-1.14	-0.02
24	5.04	-36.88	-1.62	-0.26	-0.50	-1.12	0.12

The standard deviation also shows that all designs including a flexible element outperform the rigid case. Especially for higher wind speeds, the rigid floater design struggles to capture the standard deviation and heavily underpredicts it.

Again, the Short design performs best at rated wind speed, capturing the standard deviation with 1.7 % accuracy; however, it struggles at high wind speeds. The Improved design shows the overall best performance, especially for high wind speeds. The worst performing is the Dual design, which struggles to perform well at high wind speeds. The Fine and Coarse element are also capable of capturing the standard deviation closely. A difference between the two can be seen, with the Fine design performing better. This trend is seen over all wind speeds and is biggest at high wind speeds, where the difference between them is 0.24 % relative to the flexible design. Even though the overall difference is small, it indicates that more elements help to better capture the dynamics.

Turbulent Wind

The following part focuses on the tower bending under turbulent wind fields with mean wind speeds ranging from 4 m/s to 20 m/s generated using the methodology explained in subsection 3.3.1. Firstly, mean and standard deviation for the different wind speeds and designs are looked at, again relative to the flexible floater design, in order to emphasise differences.

Table 4.12: Mean of tower root bending for turbulent wind of the flexible floater and of the different designs relative to the flexible floater. All values were taken after a transient of 100 seconds.

wps [m/s]	**Flexible** [MN]	**Rigid**	**Short**	**Fine**	**Coarse**	**Dual**	**Improved**
			[%] relative to Flexible				
4	34.92	-1.08	0.47	0.42	0.41	0.36	0.37
6	-72.07	-1.63	-0.19	-0.11	-0.11	-0.09	-0.06
8	-184.39	-1.40	-0.03	0.03	0.02	0.03	0.05
10	-243.33	-1.24	-0.00	0.05	0.05	0.05	0.07
12	-200.61	-1.50	0.01	0.06	0.06	0.06	0.09
14	-206.22	-1.45	-0.03	0.02	0.01	0.01	0.04
16	-185.51	-1.60	-0.06	-0.05	-0.05	-0.05	-0.02
18	-160.85	-1.61	-0.08	-0.06	-0.06	-0.06	-0.03
20	-147.16	-1.64	-0.06	-0.02	-0.02	-0.02	0.02

The mean tower bending from Table 4.13 shows the same results as the constant wind case. All flexible element designs perform better than the rigid floater design. For low wind speeds the flexible model designs with a higher MAC number also have a better match in mean tower bending. Close to rated wind speeds, the Short design performs best. In general, the differences are again so small that no further conclusion can be drawn.

Table 4.13: Standard deviation of tower root bending for turbulent wind of the flexible floater and of the different designs relative to the flexible floater. All values were taken after a transient of 100 seconds.

wsp [m/s]	**Flexible** [MN]	**Rigid**	**Short**	**Fine**	**Coarse**	**Dual**	**Improved**
			[%] relative to Flexible				
4	30.14	4.22	0.54	0.46	0.48	0.52	0.43
6	54.22	1.59	0.35	0.33	0.34	0.36	0.33
8	60.29	0.33	0.33	0.32	0.32	0.32	0.32
10	50.01	-0.75	0.28	0.38	0.36	0.30	0.40
12	62.04	-7.39	0.37	0.36	0.31	0.17	0.38
14	47.69	-10.99	0.67	0.99	0.92	0.71	1.05
16	47.35	-17.08	1.04	1.54	1.39	0.95	1.65
18	42.82	-20.40	1.26	1.69	1.54	1.05	1.78
20	49.18	-18.58	3.49	3.35	3.31	3.12	3.29

The standard deviation of the rigid floater design overpredicts the standard deviation at low wind speeds and overpredicts it at high wind speeds. A match of 0.75 % relative to the flexible floater can be found around rated wind speed. The shift from over- to underpredicting stems from the shift of 3P and 6P, shifting further away from the tower's first bending natural frequency of the rigid floater design with increasing wind speed.

Overall, all flexible element designs match the standard deviation of the flexible case significantly better than the rigid floater design. All designs show an increase in overestimation with increasing wind speed. This is likely to be coupled to the increase in standard deviation of the wind.

Again, the Short design performs best around rated wind speed but struggles for low and high

wind speeds. The Dual design performs well in the range of rated wind speeds and is the best performing at high win speeds, with an overestimation of 3 %. The difference between Fine and Coarse design indicates better performance of the Coarse design. However, the differences are relatively small and hence do not allow for a clear conclusion. The Improved design's standard deviation is similar to the Fine and Coarse without any significant differences.

In order to understand this dynamic behaviour better, the spectrum at a mean wind speed of 20 m/s in the range of the tower's first bending natural frequencies is looked at in section A.9.

Regular Waves

Looking at the time domain results under regular waves, a discrepancy was found in the bending moment at tower root that was larger than expected. These plots are shown in section A.10.

The observed differences lead to the decision to investigate the flexible and rigid floater design's dynamics by looking at the RAOs. This error assessment step is explained in subsection 3.1.6 with the main conclusion that a double counting of heave excitations leads to a higher response of the flexible floaters' rigid body motions. This also influences the bending moment through the increased pitch motion.

Hence, the flexible floater results which were initially intended to be the reference case have to be taken with a degree of caution, making it difficult to evaluate the performance of the different designs. Due to this uncertainty, the mean and standard deviation of the bending moment for the regular wave cases of the different designs are reported as absolute values in Table 4.14 and Table 4.15.

Table 4.14: Mean of tower root bending for regular waves of the different designs. All values were taken after a transient of 100 seconds.

Hs [m]	**T** [s]	**Flexible**	**Rigid**	**Short**	**Fine**	**Coarse**	**Dual**	**Improved**
				[MN]				
1.10	8.52	116.39	114.88	116.59	116.60	116.60	116.57	116.60
1.18	8.31	116.34	114.85	116.56	116.57	116.57	116.54	116.57
1.32	8.01	116.21	114.79	116.50	116.51	116.50	116.48	116.50
1.54	7.65	116.22	114.87	116.57	116.59	116.58	116.56	116.58
1.84	7.44	116.26	114.98	116.69	116.70	116.69	116.67	116.70
2.19	7.46	116.27	115.08	116.79	116.80	116.79	116.77	116.79
2.60	7.61	116.27	115.21	116.92	116.93	116.93	116.90	116.93
3.06	8.05	116.18	115.09	116.80	116.81	116.81	116.78	116.81
3.62	8.52	116.96	115.56	117.28	117.29	117.28	117.26	117.28
4.03	8.99	117.88	116.13	117.85	117.86	117.86	117.83	117.86
4.52	9.45	118.67	116.25	117.97	117.98	117.98	117.95	117.98

With the results of the flexible floater being influenced by the double counting of heave motion, it is difficult to compare results to this as a reference. Instead, focus is put on the general behaviour for different sea states and the results of the flexible element designs compared to each other. The general development shows little sensitivity of the mean bending moment towards an increasing wave height and wave period. The standard deviation, on the other hand, increases with increasing period and wave height. Comparing the different flexible element designs with each other, they all

show similar results with small fluctuations. No clear trend is visible that would link a too high or too low mean or standard deviation to a match of the tower's first bending mode shape.

Table 4.15: Standard deviation of tower root bending for regular waves of the different designs. All values were taken after a transient of 100 seconds.

Hs [m]	**T** [s]	**Flexible**	**Rigid**	**Short**	**Fine**	**Coarse**	**Dual**	**Improved**
				[MN]				
1.10	8.52	29.55	26.42	27.02	27.03	27.03	27.03	27.03
1.18	8.31	34.12	29.53	30.23	30.24	30.24	30.24	30.24
1.32	8.01	41.70	34.88	35.77	35.78	35.78	35.78	35.77
1.54	7.65	47.54	37.35	38.38	38.40	38.40	38.40	38.39
1.84	7.44	56.05	42.17	43.41	43.44	43.43	43.43	43.42
2.19	7.46	65.37	49.17	50.60	50.63	50.63	50.62	50.62
2.60	7.61	82.24	64.48	66.27	66.30	66.29	66.28	66.31
3.06	8.05	94.73	79.01	81.01	81.05	81.04	81.02	81.06
3.62	8.52	98.35	87.55	89.52	89.54	89.54	89.52	89.55
4.03	8.99	87.83	84.38	86.07	86.09	86.08	86.06	86.09
4.52	9.45	64.06	73.40	74.64	74.65	74.64	74.62	74.64

Irregular Waves

The time series of pitch and bending moment at root are shown in section A.11 and discussed in more detail. In general the flexible floater design shows an increased response due to the double counting of the heave motion mentioned earlier. Additionally, the flexible floater design and flexible element designs all show a clear peak at 0.4125 Hz, whereas the peak is at 0.45 Hz. This indicates the successful shift of the tower first bending natural frequency.

The different flexible element designs' mean values, as reported in Table 4.16 are again comparable. Hence, no conclusions can be drawn towards a dependency on the MAC number. The different designs' mean values also show a better match with the flexible floater design than the rigid floater design, which must be taken with care, though.

Table 4.16: Mean of tower root bending for irregular waves of the different designs. All values were taken after a transient of 100 seconds.

Hs [m]	**T** [s]	**Flexible**	**Rigid**	**Short**	**Fine**	**Coarse**	**Dual**	**Improved**
				[MN]				
1.10	8.52	116.23	114.75	116.46	116.47	116.47	116.44	116.47
1.18	8.31	116.15	114.73	116.45	116.46	116.45	116.43	116.45
1.32	8.01	116.13	114.80	116.50	116.52	116.51	116.48	116.51
1.54	7.65	115.93	114.80	116.50	116.51	116.50	116.48	116.50
1.84	7.44	116.12	114.89	116.60	116.62	116.61	116.59	116.61
2.19	7.46	116.03	114.96	116.66	116.68	116.67	116.65	116.67
2.60	7.61	116.09	115.10	116.82	116.84	116.83	116.80	116.83
3.06	8.05	116.60	115.25	116.98	116.99	116.98	116.96	116.98
3.62	8.52	116.61	115.34	117.06	117.07	117.07	117.04	117.07
4.03	8.99	116.23	115.55	117.29	117.30	117.29	117.27	117.30
4.52	9.45	117.36	115.33	117.02	117.03	117.02	117.00	117.02

The standard deviations compared in Table 4.17 show significantly higher values for the flexible floater design. Comparing the flexible element designs with each other, a maximum difference of 1.4 % is identified. Unfortunately, with the lack of a reliable reference, it is not possible to draw any conclusion from this other than that the small differences in the MAC number have no significant impact on mean and standard deviation of the bending moment at root.

Table 4.17: Standard deviation of tower root bending for irregular waves of the different designs. All values were taken after a transient of 100 seconds.

Hs [m]	**T** [s]	**Flexible**	**Rigid**	**Short**	**Fine**	**Coarse**	**Dual**	**Improved**
				[MN]				
1.10	8.52	20.71	13.54	14.28	14.32	14.31	14.28	14.33
1.18	8.31	22.98	14.23	15.38	15.39	15.41	15.50	15.42
1.32	8.01	24.13	15.15	16.06	16.09	16.08	16.07	16.10
1.54	7.65	31.59	16.39	19.88	19.92	19.96	20.15	20.01
1.84	7.44	35.08	18.76	20.17	20.21	20.21	20.23	20.23
2.19	7.46	42.73	22.05	23.73	23.77	23.78	23.82	23.81
2.60	7.61	57.89	30.23	33.36	33.47	33.46	33.42	33.52
3.06	8.05	63.65	39.73	42.17	42.23	42.23	42.29	42.27
3.62	8.52	77.01	49.41	51.92	51.97	51.98	52.01	52.01
4.03	8.99	86.19	53.90	56.30	56.38	56.36	56.32	56.41
4.52	9.45	95.76	59.76	62.11	62.17	62.16	62.17	62.20

Design Load Case

Simulations under Design Load Case include turbulent wind and irregular waves, as reported in Table 3.7. Due to the findings in subsection 3.1.6 regarding the increased sensitivity of the flexible floater towards wave excitations, the flexible floaters' DLC simulations need to be looked at with care. The pitch motion of the different designs is looked at in section A.12. The main observation is

that the impact of double counting is not as significant, which is expected to stem from the additional aerodynamic damping added by including wind.

Next the bending moment at tower root is to looked at. For this, Figure 4.13 visualises the time series and spectrum. The wave and wind spectrum are additionally shown. They are both normalised in order to be able to show them in the same plot.

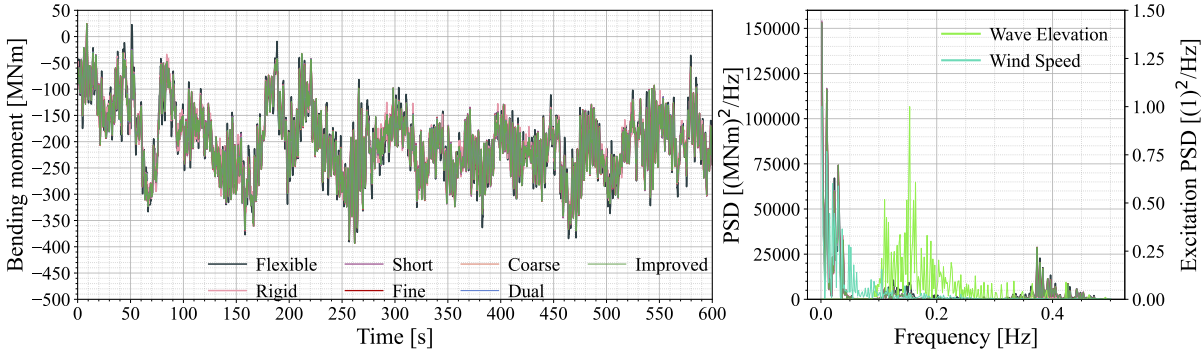

Figure 4.13: Time series and spectrum of tower root bending for for DLC with mean wind speed of 12 m/s, waves of Hs = 1.18 m and Tp = 8.31 s.

The mean value in the time domain looks identical without any clear differences. Looking at the results from Table 4.18 it is found that all designs are indeed in the same range. The flexible element designs are also closer to the flexible floater design than the rigid floater design, even though this does not automatically mean that they more accurately capture the real behaviour, as the flexible floater design is still impacted by the double-counted heave excitation. Comparing the mean values of the different flexible element designs, it appears that an increased match in MAC number results in a lower mean bending moment. This trend is found for all DLCs.

Table 4.18: Mean of tower root bending for DLCs of the different designs. All values were taken after a transient of 100 seconds.

wsp [m/s]	**Hs** [m]	**T** [s]	**Flexible**	**Rigid**	**Short**	**Fine** [MN]	**Coarse**	**Dual**	**Improved**
4	1.10	8.52	35.06	34.66	35.21	35.20	35.19	35.17	35.18
6	1.18	8.31	-71.99	-70.85	-71.89	-71.94	-71.94	-71.95	-71.98
8	1.32	8.01	-184.24	-181.75	-184.27	-184.38	-184.37	-184.37	-184.42
10	1.54	7.65	-243.22	-240.24	-243.27	-243.40	-243.39	-243.39	-243.45
12	1.84	7.44	-199.78	-197.14	-200.12	-200.23	-200.22	-200.23	-200.29
14	2.19	7.46	-205.73	-202.81	-205.72	-205.82	-205.81	-205.82	-205.87
16	2.60	7.61	-183.88	-181.25	-184.12	-184.18	-184.18	-184.18	-184.24
18	3.06	8.05	-159.85	-157.60	-160.04	-160.12	-160.11	-160.12	-160.17
20	3.62	8.52	-145.92	-143.77	-146.06	-146.12	-146.11	-146.12	-146.17

The spectrum generally shows better agreement of the peak height between the different designs, but due to the frequency range, comparison is difficult. The frequency range can be split into three different regions, though, that allow for better analysis. The three regions indicate excitation through

waves, wind and the frequency range around the tower's first bending frequency and are all shown individually in Figure 4.14.

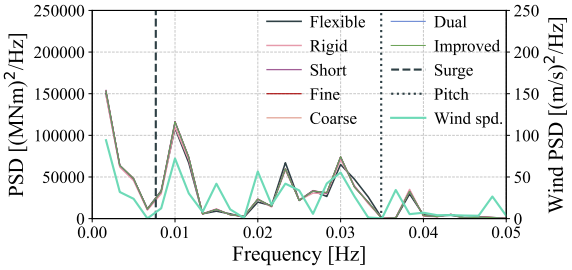

(a) Spectrum of tower root bending for DLC with mean wind speed of 12 m/s, waves of Hs = 1.18 m and Tp = 8.31 s with a focus on the wind excitation range.

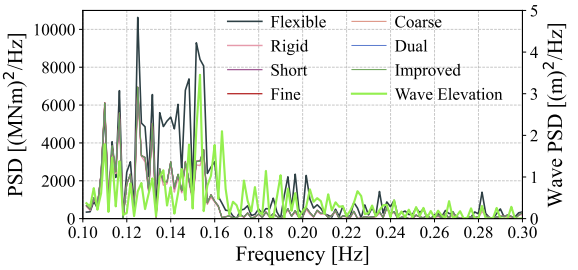

(b) Spectrum of tower root bending for DLC with mean wind speed of 12 m/s, waves of Hs = 1.18 m and Tp = 8.31 s with a focus on the wave excitation range.

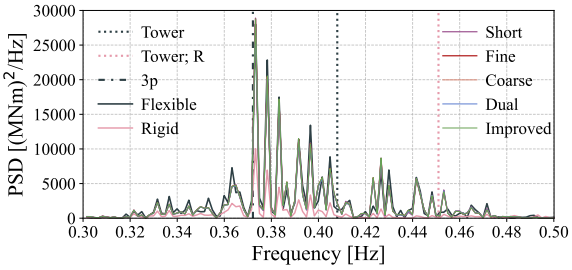

(c) Spectrum of tower root bending for DLC with mean wind speed of 12 m/s, waves of Hs = 1.18 m and Tp = 8.31 s with a focus on the range around the tower's first bending natural frequency.

Figure 4.14: Combined PSD figures for DLC 1.1 with wsp = 12 m/s, Hs = 1.18 m and Tp = 8.31.

In the wind-dominated frequency range, the different designs show only little differences. Peaks in the wind spectrum align well with peaks in the tower bending, indicating a correct response of all designs. The spectrum focusing on the wave-dominated frequency range, on the other hand, shows significantly higher excitation for the flexible floater model because of double counting of the heave motions. The different flexible element designs are all well aligned compared to each other and in line with the wave spectrum peaks, indicating a correct response. In the range around the tower's first bending frequency, the flexible floater design and flexible element designs show higher excitation around 3P than the rigid floater. This is due to the first tower bending frequency of these designs being closer and hence increased excitation.

In general, all flexible element designs show realistic behaviour and are comparable to each other. The mean values for the different DLCs as shown in Table 4.18, as well as the standard deviations shown in Table 4.19 are very similar and do not give any insight on the influence of the MAC number on the tower bending. The standard deviation for the flexible floater designs is again significantly higher for all DLCs when compared to the rigid floater design and the flexible element designs. Looking at Figure 4.14 the main reason for this is the difference in response in the wave frequency range.

Table 4.19: Standard deviation of tower root bending for DLCs of the different designs. All values were taken after a transient of 100 seconds..

wsp [m/s]	**Hs** [m]	**T** [s]	**Flexible**	**Rigid**	**Short**	**Fine**	**Coarse**	**Dual**	**Improved**
					[MN]				
4	1.10	8.52	35.07	33.96	33.13	33.12	33.12	33.13	33.11
6	1.18	8.31	57.58	56.74	56.20	56.19	56.20	56.20	56.19
8	1.32	8.01	64.07	62.09	62.23	62.23	62.23	62.23	62.24
10	1.54	7.65	54.80	51.84	52.46	52.50	52.49	52.46	52.51
12	1.84	7.44	66.58	59.81	64.58	64.57	64.55	64.47	64.59
14	2.19	7.46	56.78	47.03	52.41	52.55	52.51	52.42	52.58
16	2.60	7.61	64.52	48.39	56.26	56.50	56.43	56.25	56.55
18	3.06	8.05	68.73	51.44	59.05	59.33	59.28	59.11	59.38
20	3.62	8.52	83.25	62.61	71.29	71.05	71.03	70.95	71.05

4.3.3 Influence of Tower Mode Shape Deviation on Tower Acceleration (C3 Q)

Additionally, to the tower bending the influence of the flexible element on the tower accelerations is also checked. The tower acceleration is design driving for loads on secondary tower structures, as they are determined through their own inertia. Focus will be put on the tower top acceleration.

Constant wind

Starting point of increasing complexity of environmental loads is again the case of constant wind. The mean values are all roughly identical with 0 m/s^2. This is also found for all other wind speeds and is the expected outcome, as after the transient the FOWT simply oscillates around equilibrium.

On the other hand, the standard deviation reported in Table 4.20 appears to be significantly higher for the rigid floater case.

Table 4.20: Standard deviation of tower top acceleration for constant wind of the flexible floater and of the different designs relative to the flexible floater. All values were taken after a transient of 100 seconds.

wsp [m/s]	**Flexible** [mm/s^2]	**Rigid**	**Short**	**Fine**	**Coarse**	**Dual**	**Improved**
				[%]			
4	2.66	-53.35	-1.66	-0.95	-1.00	-0.99	-0.65
6	5.53	-48.17	-0.85	-0.31	-0.34	-0.32	-0.15
8	7.69	-47.32	-0.73	-0.22	-0.24	-0.22	-0.08
10	6.09	-31.72	-2.43	-0.16	-0.18	0.26	0.82
12	6.47	-37.12	1.40	4.04	4.05	4.26	4.36
14	9.00	-21.06	1.37	2.18	2.22	2.38	2.22
16	9.64	-16.40	1.49	1.31	1.42	1.69	1.15
18	11.82	-4.09	2.14	1.20	1.37	1.71	0.86
20	14.27	6.77	2.31	1.16	1.37	1.80	0.71
22	17.30	14.51	2.54	1.20	1.42	1.90	0.74
24	21.66	17.82	2.28	0.86	1.07	1.52	0.39

The overall standard deviation of the tower top acceleration is relatively small, with a max value of 21.66 mm/s^2. The different flexible element designs show a clear improvement compared to the rigid floater design, decreasing the max difference from 53.35 % to 4.36 %. Especially at low wind speeds the flexible element designs perform better. The Improved design shows the best performance at low and high wind speeds. The Dual design had a similar MAC number (MAC=0.9999) to the Coarse and Fine design (MAC = 0.9995), and they all have a similar match of tower top acceleration standard deviation, indicating that a higher MAC number results in a better match. In line with this, the Short design is the overall worst performing design, except for operation at rated wind speed. The Fine design performs better than the Coarse design implying that the standard deviation of tower top acceleration for designs is better captured with higher segmentation.

section A.13 investigates the results of the different designs in more detail on the example of a mean wind speed of 10 m/s.

Turbulent Wind

In the next step the different designs are compared under turbulent wind speeds. Again, the results indicates a mean acceleration of 0 m/s^2, as the floater solely oscillates around its new equilibrium position after the transient.

The standard deviation of tower top acceleration for different wind speeds is summarised in Table 4.21, as well as the absolute maximum in Table 4.22.

Table 4.21: Standard deviation of tower top acceleration for turbulent wind of the flexible floater and of the different designs relative to the flexible floater. All values were taken after a transient of 100 seconds.

wsp [m/s]	**Flexible** [mm/s^2]	**Rigid**	**Short**	**Fine** [%]	**Coarse**	**Dual**	**Improved**
4	66.99	-36.72	-6.53	-4.91	-5.16	-5.60	-4.24
6	91.99	-37.55	-6.60	-5.39	-5.58	-5.84	-4.88
8	107.64	-24.55	-4.58	-3.69	-3.78	-3.79	-3.29
10	134.83	-11.07	-1.83	-1.65	-1.58	-1.17	-1.42
12	200.10	10.84	-1.99	-1.86	-1.72	-1.05	-1.63
14	191.30	15.03	-2.35	-2.43	-2.27	-1.59	-2.28
16	240.80	18.90	-1.89	-2.06	-1.82	-0.90	-2.02
18	238.02	14.74	-2.31	-2.32	-2.13	-1.32	-2.20
20	279.37	16.88	-5.09	-4.78	-4.71	-4.29	-4.58

Table 4.22: Absolute maximum of tower top acceleration of the flexible floater and of the different designs relative to the flexible floater for different mean wind speeds.

wsp [m/s]	**Flexible** [mm/s^2]	**Rigid**	**Short**	**Fine** [%]	**Coarse**	**Dual**	**Improved**
4	265.30	-17.93	-4.74	-5.39	-5.49	-5.71	-5.48
6	352.05	-48.42	-8.68	-8.46	-8.67	-9.37	-8.41
8	459.89	-8.17	-0.13	1.35	1.29	1.21	1.08
10	557.97	-24.93	-0.23	3.93	3.99	4.74	5.12
12	754.83	15.29	-0.64	1.66	1.62	1.81	1.19
14	840.60	27.41	2.46	4.28	4.48	5.42	4.91
16	932.95	18.08	-2.96	0.06	0.24	0.95	0.14
18	994.97	10.18	-6.07	-3.19	-3.13	-2.41	-1.87
20	1031.64	13.36	-9.62	-8.10	-8.11	-7.39	-6.70

Again, a significant improvement from the rigid floater design to the flexible element designs is observed when comparing the standard deviations. The relative difference is reduced from up to 37.55 % down to 6.6 % for the worst result. The differences between the flexible element designs are more significant than in previous cases. The Short design is the overall worst performing especially at low wind speeds. The differences between the other designs with same length and almost identical MAC number show no clear pattern. At low wind speeds, for example, the Improved design is best performing, whereas at rated and higher wind speeds the Dual design shows the lowest deviations from the flexible design. The Fine flexible element design performs better than the Coarse at low wind speed but worse at above rated wind speeds.

The absolute maximum shows big differences between flexible floater design and the flexible element designs for high wind speeds. Even though, all cases still outperform the rigid floater design the improvement is less significant. The Short design for example shows a difference of 9.62 % at 20 m/s wind speed, compared to the rigid floater design with 13 %. However, the rigid floater design underpredicts the acceleration, whereas the flexible element design overestimates it. The Short design performs best again around rated wind speed. The other designs show random fluctuations over the wind speeds, which is expected to stem from the randomness of the turbulence for each wind speed seed. Out of the four 10 m long designs the Fine and Coarse design are closest to the flexible floater design, but at high wind speeds they are outperformed by the Dual and Improved design, with the Improved design as best performing at high wind speeds. Due to the amount of variations over wind speeds and between the results no clear pattern is identified that relates a match in MAC number with the capability of replicating the flexible floater design.

A time series with a mean wind speed of 10 m/s is shown as an example in section A.14.

Regular Waves

Looking at the standard deviations presented in Table 4.23 the increased sensitivity of the flexible floater due to the double counting of heave motion can be identified for all wave configurations. The flexible element designs are all in the same range which is different from the rigid floater design. The Dual and Improved design show only minor differences over all wave conditions, similar to the Fine and Coarse design, with the Short design showing bigger differences to the other design. Even though there is no clear reference the similarities potentially stem from the similar MAC numbers

between the pairs.

Table 4.23: Standard deviation of tower top acceleration for regular waves of the different designs. All values were taken after a transient of 100 seconds.

H [m]	**T** [s]	**Flexible**	**Rigid**	**Short**	**Fine**	**Coarse**	**Dual**	**Improved**
				[mm/s^2]				
1.10	8.52	65.59	48.12	47.76	47.82	47.83	47.86	47.87
1.18	8.31	75.07	55.31	54.75	54.86	54.86	54.93	54.94
1.32	8.01	94.93	69.50	68.56	68.75	68.76	68.86	68.88
1.54	7.65	123.50	86.42	85.12	85.37	85.39	85.54	85.56
1.84	7.44	157.86	107.66	106.00	106.33	106.35	106.53	106.56
2.19	7.46	184.19	125.61	123.66	124.04	124.06	124.28	124.31
2.60	7.61	214.41	149.98	147.72	148.16	148.19	148.44	148.48
3.06	8.05	217.25	158.75	156.63	157.04	157.07	157.31	157.34
3.62	8.52	216.44	158.85	157.64	157.85	157.86	157.99	158.00
4.03	8.99	217.47	152.45	152.32	152.28	152.28	152.27	152.26
4.52	9.45	247.27	156.41	157.47	157.16	157.15	156.99	156.97

Additionally, an example time series and spectrum of sea state conditions with significant wave height of 1.54 meters and 7.66 seconds peak period are shown and discussed in section A.15.

Irregular Waves

The standard deviation and absolute maximum of tower top acceleration for the different wind speeds as well as an example time series and spectrum are summarized in section A.16. The values for the flexible floater design are as expected significantly larger than for the other designs. The standard deviation and absolute maximum of all flexible element designs show only minor differences, that do not allow for any conclusions on the impact of the MAC number on the capability of capturing the tower top acceleration.

Design Load Case 1.1

The time series of the tower top acceleration under DLC conditions with mean wind speed of 12 m/s, significant wave height of 1.84 m and peak period of 7.44 s is shown in Figure 4.15. As expected the time series shows differences between the flexible floater design and the other designs. But upon closer inspection differences can also be spotted between the different flexible element designs. Looking at the spectrum of the time series in Figure 4.15 the difference between the flexible floater design and the others is identified to stem from within the wave frequency range, whereas the differences between the flexible element designs appear to be most significant in the frequency range of the tower natural frequencies. Hence, specific focus is put on these two frequency ranges.

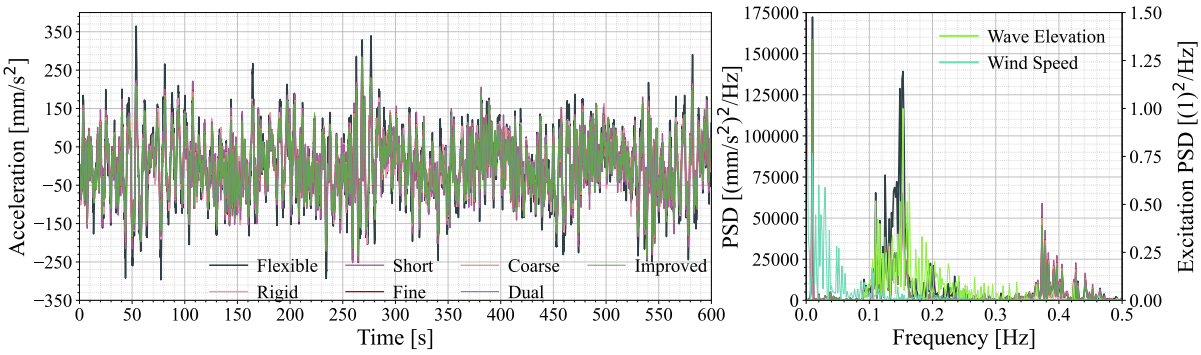

Figure 4.15: Time series and spectrum of tower top acceleration for DLC with wsp = 12 m/s, Hs = 1.84 m and Tp = 7.44 s.

Figure 4.16a clearly shows higher peaks of more energy content for the flexible floater design, indicating larger excitation. The reason for this is the in subsection 3.1.6 discussed double counting of heave excitation. This limits the possibilities to compare the different designs with the flexible floater design as reference model. Instead the focus is shifted on comparing the flexible element designs with each other. Figure 4.16b shows differences between the energy contents of the different designs despite there tower first bending frequency being the same. It is hence expected, that the differences, that are also observed over different wind speeds as shown in Table 4.24 and Table 4.25 are due to the difference in the tower first bending mode shape.

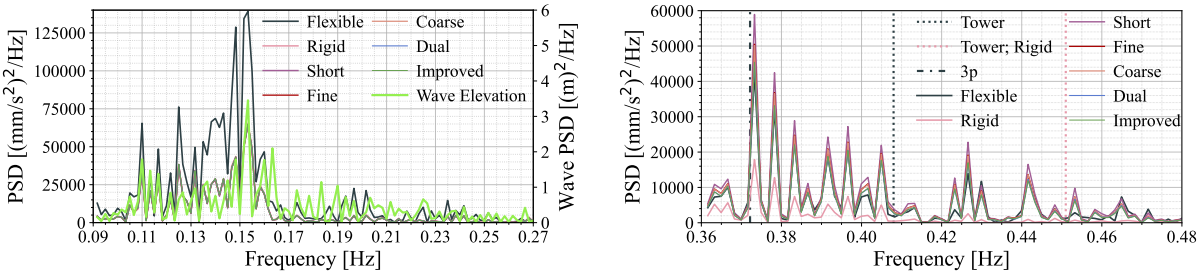

(a) Spectrum of tower top acceleration for DLC with wsp = 12 m/s, Hs = 1.84 m and Tp = 7.44 s with focus on wave frequency range.

(b) Spectrum of tower top acceleration for DLC with wsp = 12 m/s, Hs = 1.84 m and Tp = 7.44 s with focus on tower first bending frequency.

Figure 4.16: Spectrum of tower top acceleration for constant wind of 10 m/s.

Table 4.24: Standard deviation of tower top acceleration for DLCs of the different designs. All values were taken after a transient of 100 seconds.

wsp [m/s]	**Hs** [m]	**T** [s]	**Flexible**	**Rigid**	**Short**	**Fine**	**Coarse**	**Dual**	**Improved**
					[mm/s^2]				
4	1.10	8.52	57.26	41.81	39.24	38.62	38.63	38.54	38.49
6	1.18	8.31	62.59	47.62	44.23	43.10	43.11	42.96	42.90
8	1.32	8.01	69.38	51.36	48.93	47.72	47.73	47.61	47.61
10	1.54	7.65	76.76	55.15	55.01	52.98	52.99	52.87	53.06
12	1.84	7.44	95.99	67.92	76.10	72.40	72.36	71.66	71.92
14	2.19	7.46	106.93	70.95	77.21	74.07	74.04	73.51	73.78
16	2.60	7.61	140.05	94.07	101.23	97.60	97.55	96.86	97.19
18	3.06	8.05	163.36	111.32	117.44	114.26	114.23	113.54	113.78
20	3.62	8.52	186.80	127.38	134.17	130.25	130.25	129.63	129.76

The two tables above also show the differences between the different flexible element designs. Even though it can't be assessed which design is performing best and by which margin (because of the faulty behaviour of the reference model) the results reported in Table 4.24 and Table 4.25 give some insight on the behaviour of the flexible element designs compared to each other. The mean values of the Fine and Coarse design are almost identical for all wind speeds, indicating that the amount of segments does not influence the mean result. The Dual and Improved design show similar mean values. Their MAC number is also identical indicating that a similar MAC number results in a close mean tower top acceleration. The Short design, on the other hand, is the only flexible element design that shows significant differences. The results are comparatively higher for all wind speeds. This difference is most likely to stem from the smaller MAC number and hence less accurate match of tower first bending mode shape.

The absolute max values reported in Table 4.25 show variation for the different designs that do not show any clear patterns. With the lack of a reference it is hence not possible to draw any conclusions on the impact of MAC number on the performance.

Table 4.25: Absolute maximum of tower top acceleration for DLCs of the different designs. All values were taken after a transient of 100 seconds..

wsp [m/s]	**Hs** [m]	**T** [s]	**Flexible**	**Rigid**	**Short**	**Fine**	**Coarse**	**Dual**	**Improved**
					[mm/s^2]				
4	1.10	8.52	205.62	134.99	147.76	138.65	138.74	138.21	138.42
6	1.18	8.31	187.90	149.11	145.28	137.42	137.01	132.59	131.68
8	1.32	8.01	230.30	193.46	154.44	146.51	147.59	150.56	152.25
10	1.54	7.65	234.11	165.83	194.42	175.75	176.21	172.50	172.99
12	1.84	7.44	364.76	229.03	266.22	264.83	268.98	278.20	284.88
14	2.19	7.46	340.27	232.43	240.24	213.94	214.37	226.52	228.40
16	2.60	7.61	529.17	344.57	380.24	374.65	376.42	382.42	383.59
18	3.06	8.05	465.63	373.28	384.36	359.77	359.33	360.55	362.34
20	3.62	8.52	706.02	429.86	450.66	424.97	426.14	418.15	419.40

4.3.4 Influence of Tower Mode Shape Deviation on Tower Top Rotation (C4 Q)

The rotational position of the tower top and root is interesting as it defines the angle of the RNA and floater. The angle of the RNA is of special interest for Siemens Gamesa, as it is often a design limiting factor. Mean and standard deviation are mainly compared.

In the course of comparing the results it was found that there is no difference between the relative top and root angle. The difference in height simply results in a relative increase. Furthermore, the mean values of all designs relative to the flexible floater design are less than 0.06 % over all environmental conditions. This leads to the decision to instead focus on only the tower top rotation and its standard deviation.

The tower top rotation is given in degrees. An angle of zero degrees corresponds to an upright tower. Positive rotation around global y-axis (Figure 3.3), so in positive pitch direction also corresponds to positive tower top node rotation.

Constant wind

The standard deviation of all designs is relatively low with 0.137°. In the case of constant wind with no dynamics, except for the transient, this is expected. The relative difference of the different designs compared to the flexible floater design show a clear improvement for the flexible element designs over the rigid floater design. The worst match of the flexible element designs is found at rated wind speed. Other than that it is found that the four 10 m designs with similar MAC number are outperforming the Short design at low and higher wind speeds, whereas the Short design is performing best around rated wind speed.

Table 4.26: Standard deviation of tower top rotation for constant wind of flexible floater and of the different designs relative to the flexible floater. All values were taken after a transient of 100 seconds.

wsp [m/s]	**Flexible** [°]	**Rigid**	**Short**	**Fine** [%]	**Coarse**	**Dual**	**Improved**
4	0.041	1.384	-0.482	-0.448	-0.442	-0.440	-0.475
6	0.091	1.766	-0.327	-0.182	-0.175	-0.179	-0.222
8	0.121	1.860	-0.618	-0.376	-0.369	-0.369	-0.416
10	0.092	1.222	-0.766	-0.084	-0.077	-0.067	-0.105
12	0.078	1.386	1.253	3.645	3.650	3.660	3.641
14	0.119	1.624	0.219	0.931	0.936	0.947	0.932
16	0.113	0.959	-0.522	-0.220	-0.215	-0.228	-0.268
18	0.122	0.078	-0.611	-0.252	-0.248	-0.258	-0.276
20	0.129	-0.072	-0.577	0.006	0.007	-0.004	-0.010
22	0.134	0.067	-0.560	0.203	0.204	0.192	0.183
24	0.134	0.202	-0.510	0.606	0.607	0.596	0.583

Turbulent Wind

Already at low wind speeds the standard deviation in case of turbulent wind is higher than for constant wind, as can be seen in Table 4.27. This is due to the added turbulence. Similar to the case with constant wind implementing any flexible element already improves the results from the rigid floater design. The biggest difference is not found at rated wind speed, but for a mean wind speed

of 18 m/s. The standard deviation of the 600 second wind train was calculated for all wind speeds, and was found to be highest at 18 m/s. However, the difference is small and hence not expected to be the sole reason for the observed increased difference in standard deviation. In case of turbulent wind the Short flexible element design is the overall best performing design. Other than that no clear dependencies are identified.

Table 4.27: Standard deviation of tower top rotation for turbulent wind of flexible floater and of the different designs relative to the flexible floater. All values were taken after a transient of 100 seconds.

wsp [m/s]	**Flexible** [°]	**Rigid**	**Short**	**Fine** [%]	**Coarse**	**Dual**	**Improved**
4	0.378	3.000	-0.286	-0.351	-0.339	-0.310	-0.367
6	0.628	4.633	-0.018	-0.218	-0.204	-0.233	-0.337
8	0.824	3.159	-0.281	-0.386	-0.376	-0.369	-0.430
10	0.746	1.939	-0.480	-0.606	-0.598	-0.596	-0.650
12	0.880	2.423	-0.283	-0.130	-0.121	-0.115	-0.160
14	0.615	2.602	-0.213	-0.271	-0.263	-0.239	-0.268
16	0.552	1.855	-0.549	-0.740	-0.729	-0.713	-0.775
18	0.424	1.688	-0.960	-2.420	-2.410	-2.377	-2.424
20	0.646	1.848	-0.216	-0.136	-0.125	-0.091	-0.140

Regular and Irregular Waves

The influence of regular as well as irregular waves on the standard deviation of the tower top rotation is small. The flexible element designs have the same standard deviation as the rigid floater case for most environmental conditions. Solely, the flexible floater design differs, due to the wrongly increased heave excitation. The tables containing the standard deviation for the regular and irregular wave conditions are shown in Table A.10 and Table A.11. No further insights can be drawn from the figures.

Design Load Case 1.1

The inclusion of turbulent wind and hence aerodynamic damping, additionally to the irregular waves, decreases the error of the flexible model. As a result, the standard deviation shown in Table A.12 shows similar results for all cases. All flexible element designs are still identical up to the second digit after the comma, and only differ from the flexible and rigid floater design for higher wind speeds. This leads to the conclusion that the tower top rotation is not significantly influenced by the fact whether the floater is rigid or not, and that the inclusion of any flexible element further decreases the difference. No influence of the MAC number on the tower top rotation under DLC can be concluded.

Chapter 5

Conclusion

After the presentation and discussion of the result of the different phases, a final conclusion will follow. This includes a summary of the answers to the different research questions in section 5.1, as well as a reflection on the research goal in section 5.2. Lastly a recommendation is given on how to apply the findings in section 5.3 before giving an outlook on future work in section 5.4.

5.1 Research Questions

The research questions are again split into the three different phases. The research questions have been answered throughout the thesis work, with some of them already discussed in the methodology chapter. Hence, they are summarised, and final conclusions are drawn.

5.1.1 Phase A: Flexible and Rigid Floater

Phase A deals with the creation of the fully flexible and fully rigid floater, effects observed during this process and the difference in mode shape and natural frequency between the two models.

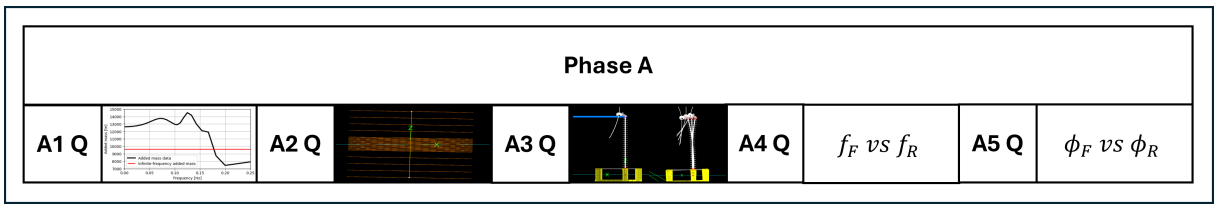

Figure 5.1: Phase A research question overview.

A1 Q: Investigation of Added Mass in Modal Analysis

The inclusion of added mass in the modal analysis approach as well as the influence on the rigid body motions was discussed in subsection 3.1.2. OrcaFlex can't use a frequency-dependent added mass matrix and hence simply assumes the added mass to be zero if a frequency-dependent added mass matrix is provided. Choosing to take a constant added mass of the infinite frequency added mass resulted in an improvement of the rigid body motions. However, the correct approach is to implement the added mass of each degree of freedom at its rigid body frequency. Without knowledge about the frequency of the rigid body motion, this requires the use of an iterative process.

The three different approaches assume different values for the constant added mass, allowing for conclusions on the impact of the added mass on the rigid body motions. With no added mass, the rigid body frequencies were found to be too high. Comparing this finding with Equation 2.4 this observation is confirmed. Using the infinite frequency added mass increases amount of added mass compared to the previous case. As a result, lower frequencies were calculated. Eventually, using the individual added mass approach the amount of added mass was increased even further and hence resulted in an additional decrease of the natural frequency. The individual added mass approach is closest to the reference values and also the typical approach.

A2 Q: Impact of Line Segmentation near SWL in OrcaFlex

The amount of segments used near SWL was found to impact the OrcaFlex results. The reason for this is expected to be that the initial trim angle of the floater results in the line elements being not "wall-sided" bodies. This altered the waterplane area calculation, resulting in a different volume, which eventually influenced the rigid body motions as noted in the model.

Increasing the number of elements yielded more accurate results. However, a high number of segments made convergence in the dynamic analysis more difficult. Hence, a trade-off between accuracy and computational effort had to be found. This was achieved by assuming rigid side columns. This allowed for more accurate calculation of the submerged volume whilst keeping the computational effort low but also avoid influencing the tower mode significantly, as the side columns are not directly connected to the tower.

A3 Q: Compare Methods to Identify Tower Modes in the Multibody System Floating Offshore Wind Turbine

Three different methods were proposed to allow for a more clearly defined identification of tower mode shapes for FOWT. While the method of simplifying less important flexible components like blades and mooring lines reduced the number of modes and hence allowed for a clear identification of the tower modes, the simplified model was not further used for two reasons. The first and most important reason is that a flexible element configuration that results in a match of tower first natural frequency for the simplified model did not likewise resulted in a match of tower first bending frequency for the complex model. Secondly, the low-fidelity simplified model had assumptions that influenced the tower modes more than expected, which, in combination with the first limitation, led to the decision to not further improve this approach.

The other two approaches were successfully implemented and also used to independently calculate the tower first bending frequencies of different models, allowing to compare the methods to each other. The methods identified the same first tower first bending frequencies, with a relative difference below 2.5%. This shows good agreement between the methods in terms of accuracy. The main difference between the two is the computational effort and capability of being automated.

While the decay test is intuitive and well explained in literature, it is computationally more heavy and requires manual identification of the tower modes by inspecting the spectrum. The modal mass method, on the other hand, is very fast and was also able to be automated. Specifically for the identification of tower natural frequencies for the flexible element designs, this was very advantageous, as it allowed the creation of many different designs. The clear disadvantage of this method is that it is not discussed in literature except for the "strain energy" approach, which is similar but not the same. Hence, the final designs' tower first bending frequencies were validated by additionally performing a decay test.

A4 Q: Differences in Tower Natural Frequency between Fully Flexible Floater Model and Fully Rigid Floater Model

Comparing the tower's first bending natural frequencies of the fully flexible and fully rigid floater model an increase in the tower's natural frequency from 0.408 Hz for the flexible floater to 0.451 Hz for the rigid floater was observed. This increase was also found in literature and is expected to stem from the increased stiffness when using a rigid floater instead of a flexible substructure.

A5 Q: Differences in Tower Mode Shape between Fully Flexible Floater Model and Fully Rigid Floater Model

The difference in the tower's first bending mode shape is mainly traced down to rigid body motions at the tower root. The rigid floater design performs more rotational and lateral displacement than the flexible floater. An approach to explaining this is that the flexible floater can store energy in kinetic form and in the form of strain energy through bending of the floater. The rigid floater, on the other hand, only allows for storing energy in the form of kinetic energy. Hence, the rigid body motions are more excessive for the rigid floater design. This also impacts the mode shape near tower root and the position of the antinode, as seen in Figure 4.3.

5.1.2 Phase B: Flexible Element Design Study

Different flexible element designs were created using the modal mass method in a *while* loop until a match in the tower's first bending natural frequency was achieved. The different designs changed different parameters in order to get a better understanding of their impact on the tower's first bending mode shape. A final conclusion on the results of these different designs is given in the following sections.

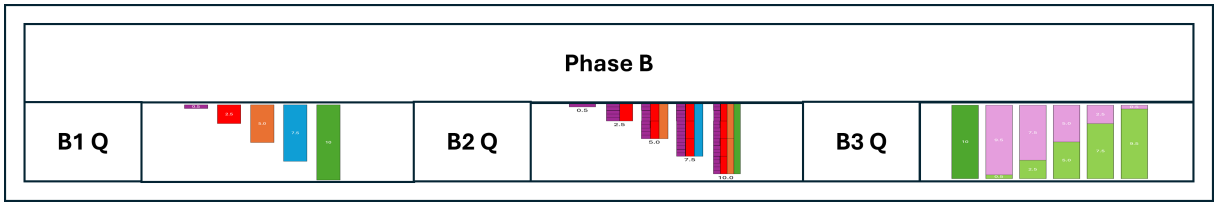

Figure 5.2: Phase B research question overview.

B1 Q: Influence of Flexible Element Length on the Tower Mode Shape

Investigating the effect of the flexible element length, it was found that a longer flexible element increases the MAC number and hence results in a better match of the first tower bending mode shape.

The use of the smallest flexible element already changes the first tower bending mode shape significantly by reducing the amount of transversal and rotational displacement of the tower root. This is expected to stem from the ability to store strain energy in addition to kinetic energy. The longer the flexible element, the more strain energy can be stored.

The flexible element length is limited by the distance to the SWL. When the flexible element is below, SWL it will alter the submerged volume, which in fact will change the FOWTs properties.

B2 Q: Influence of Flexible Element Segmentation on the Tower Mode Shape

Next, the impact of the number of segments used to model the flexible element on the tower mode shape was investigated. It was found that even though an increased number of segments creates a better match of the flexible element and floater mode shape, it has little to no influence on the tower mode shape. This leads to the assumption that not the flexible elements' capabilities of capturing the flexible floater shape are important but the capability of allowing for bending and hence strain energy.

B3 Q: Influence of Flexible Element Composition on the Tower Mode Shape

Lastly, multiple combinations of two flexible elements with different Young's modulus were tested. As a result, it was found that those combinations perform best where the Young's modulus of the flexible element that is directly connected to the tower matches the Young's modulus of the flexible floater. This conclusion was under the condition that the flexible element has the same dimensions as the centre column of the floaters' centre column, so also an identical second moment of area (I).

With this knowledge, an improved version consisting of two flexible elements and a total length of 10 m was created. The Young's modulus of the part directly connected to the tower was set to match the flexible floaters Young's modulus. This Improved design resulted in a near perfect match, indicating that the influence of the different parameters on the tower's first bending mode shape was correctly understood and applied.

5.1.3 Phase C: Effect of Tower Mode Shape Deviation

The last research questions investigated the influence of the differences in the mode shape on the tower dynamics in time domain under varied environmental conditions. The different parameters that were looked at are the tower bending moment at root, tower top acceleration and rotation of tower top and bottom node.

Phase C							
C1 Q	P	**C2 Q**	M_y	**C3 Q**	$\ddot{x}$	**C4 Q**	φ_T, φ_B

Figure 5.3: Phase C research question overview.

C1 Q: Influence of Tower Mode Shape Deviation on Decay Test

The comparison of the decay test results show a match between the flexible floater design and the different flexible element designs below 3% for standard deviation and below 0.2 % for the mean values compared to 12.37% and 1.29% for the rigid case. This confirms a successful tuning of the flexible element parameters. Furthermore, tuning the flexible element to match the tower's first natural frequency not only results in a match of that frequency but also other, coupled tower modes around the tower's first bending frequency.

Investigating the mean and standard deviation of the decay test after a transient of 100 seconds shows good agreement for all flexible element designs with the flexible floater design, especially in

contrast to the rigid floater design. This shows an overall improvement of the model accuracy over a rigid floater design. The differences between the flexible elements are minor, indicating that the differences in MAC number in a range of ± 0.002 have little influence on the results of a free tower decay test.

No differences were identified in terms of mean results of turbine performance. Neither for the flexible element designs nor for the rigid floater design.

C2 Q - Influence of Tower Mode Shape Deviation on Tower Bending

The tower bending at the root was compared under different environmental conditions in order to assess the capabilities of the different flexible element designs to capture the flexible floater designs' behaviour.

The flexible element designs' spectra of the bending moment time series show the same alignment of response peaks as the flexible floater designs. The rigid floater design shows response at different frequencies due to the different tower first bending frequencies. The flexible elements response is successfully shifted for all designs. The differences between the designs are notable in the different amplitudes of the response peaks and hence the different standard deviations.

Comparing the mean and standard deviation over different environmental conditions, the general finding is that the flexible element designs show clear improvement other than the rigid floater design. The differences between the various flexible element designs and hence the differently high MAC numbers are overall small. The results indicate a trend that favours the Short design for wind speeds around rated and, on the other hand, designs with a high MAC number for higher and lower wind speeds. The comparison of the Fine and Coarse design shows slight favour for the Fine design, indicating an increased accuracy with a higher number of segments.

C3 Q - Influence of Tower Mode Shape Deviation on Tower Acceleration

Under constant wind the tower top acceleration shows similar results as in the case of tower bending. All flexible element designs achieve a better match than the rigid floater design. Again, the Short case is performing best around rated wind speed, whereas the other designs are performing better at low and high wind speeds.

For turbulent wind, the match with the flexible floater case is less accurate but still significantly outperforms the rigid floater design. For all models a deviation from the flexible floater model results is observed for higher and lower wind speeds.

Testing with DLC, groups of flexible element designs are identified, with the Short design as an outlier from the others. Due to a missing reliable reference case, it cannot be concluded which group is more accurate, but it can be assumed that the differences in MAC number cause the formation of different groups.

The observed bigger differences between flexible element designs and flexible floater design are expected to stem from the fact that the tower acceleration is more dependent on higher modes (Feng et al., 2012). The flexible element was not tuned for a match of higher-order modes and is hence matching them possibly less accurately.

C4 Q - Influence of Tower Mode Shape Deviation on Tower Top Rotation

Comparing the results of the tower top and root rotation, it was found that the top and root rotations are relatively identical. Furthermore, the mean values are close and hence not further investigated,

focusing solely on the tower top rotations' standard deviation and absolute maximum.

At constant wind, the Short design was matching the flexible floater design best at rated, whereas the others showed better results at low and high wind speeds. Under turbulent wind conditions, on the other hand, the Short design is overall the best performing, despite having the lowest MAC number.

In general it is concluded that the influence of the floater flexibility on tower top node rotation is small. Hence, the impact of the mode shape match is also small and not significant.

5.2 Research Goal

The overall research goal is to achieve **Improved Tower Structural Dynamics for a Floating Wind Turbine with a Rigid Substructure**. With the different research questions answered, the overall initial research goal can be discussed and concluded to what extent that goal was reached.

The main advantage of using a rigid floater over a flexible one is the computational effort. All designs' simulation times are measured for a DLC with 16 m/s mean wind speed, 2.60 m significant wave height and a peak period of 7.61 s and reported in Table 5.1.

The flexible floater design requires 180 minutes to finish the simulation. Using a fully rigid floater instead takes 60 minutes. This reduction of 120 minutes results in a three times faster computation of the results, showing the clear time advantage of being less computationally heavy. For the typically high number of simulations for the validation of designs, this difference can quickly add up.

Table 5.1: Simulation time of the different designs for DLC with wsp = 16 m/s, Hs = 2.6 m and Tp = 7.64 s.

-	**Flexible**	**Rigid**	**Short**	**Fine**	**Coarse**	**Dual**	**Improved**
Simulation time [min]	180	60	55	55	60	55	58

Table 5.1 additionally reports the simulation time for the flexible floater designs. The goal is to maintain this advantage of reduced simulation time whilst increasing the accuracy of capturing the tower dynamics. The simulation times of the different flexible element designs, reported in Table 5.1, are indeed significantly lower than of the flexible floater design and comparable to the rigid floater design. The variations in required simulation time between the designs are expected to stem form performance differences of the computer.

In order to also guarantee an increase in accuracy, multiple flexible element design with different parameters and matches of the mode shape have been created. When it comes to generating the best match possible of the mode shapes, it was found that the following aspects are most important:

- Increasing the length of the flexible element increases the MAC number.
- The MAC is insensitive to the number of segments.
- A Young's modulus close to the Young's modulus of tower and centre column (200 GPa) for the segment connected to the tower increases the MAC number.

Small differences between the mode shapes of the different designs are found, with the worst design having a MAC number of 0.996. These small differences in MAC number indicate that using any flexible element design with a matching first tower natural frequency already improves the tower first mode shape.

The tower dynamics of these designs have been investigated by looking at the tower root bending moment, tower top acceleration and tower top rotation under different environmental conditions. All results indicate an improvement for every flexible element design when compared to the rigid floater design. This shows that using any flexible element configuration already helps a lot to improve the time domain result. The tower's first natural frequency is successfully shifted for all designs. This yields a good match of the spectra peak position and mostly also the magnitude of peaks.

Comparison of the flexible element designs with each other under constant and turbulent wind conditions indicates the following relation between MAC number and match of results:

- The higher the MAC number the better the match of tower bending moment at root, tower top acceleration and rotation, for low and high wind speeds.
- The Short design performs best around rated wind speed.
- A larger number of segments results in a slight increase in performance despite a similar match of the mode shape.

Under regular and irregular waves, it is more difficult to compare the designs, as the reference model is not reliable under these conditions. Nevertheless, the flexible element designs are compared to each other, indicating that the small differences in mode shape again have a minor impact on the tower dynamics.

These improvements are not that significant for the tower top acceleration, especially for higher wind speeds. Nevertheless, the results are improved and give a better match of the tower top accelerations' absolute max of at least 3.5%. The reason for this less significant match is expected to stem from the fact that the flexible element was tuned to match the tower's first mode shape, whereas the acceleration mainly depends on higher-order modes.

Ultimately, it can be concluded that the goal to achieve **Improved Tower Structural Dynamics for a Floating Wind Turbine with a Rigid Substructure**. The advantage of using a rigid floater is maintained by having lower computational effort and hence lower simulation times. Additionally, it was shown that using any flexible element configuration improves the accuracy of the determined tower dynamics compared to a purely rigid floater design.

5.3 Design recommendations

The discussion and conclusions on the design of a flexible element are drawn at the example of the UMaine VolturnUS floater. No further efforts have been made on implementing a flexible element for a different case. Instead, this is stated as a possible study outlook in the future work section. Nevertheless, this section aims to deliver a recommended design guideline for a generic case.

Using a flexible element and tuning its properties such that a match in tower first bending natural frequency is achieved increases the results over a flexible floater. This finding is expected to apply to different FOWTs.

The identified differences in the mode shape match (evaluated through the MAC number) are small. Furthermore, these small differences do not significantly translate into tower dynamics in time domain. Therefore the main goals is to tune the flexible element properties towards a match in tower first bending natural frequency. Nevertheless, a recommended design strategy for the flexible element design is given.

Investigating the sensitivity of the mode shape match over different flexible element lengths, an increasing performance was identified for with increasing length. It is expected that this is also the case for different FOWTs. However, it must be guaranteed that the flexible element is not submerged,

as this would alter the submerged volume and hence the properties of the floater.

The fining that a match in product of Young's modulus and second moment of area between flexible element and centre column of the floater increases the mode shape match is expected to behave as follows. FOWTs with a dominant connection piece to the tower, like in this case the centre column, are expected to show similar reactions. FOWT designs with a less dominant connection piece, that is for example rather short or has many struts as cross connections are expected to behave differently. It is assumed that instead of using the product of Young's modulus and second moment of area an equivalent value for the assembly needs to be determined.

These are the general designs recommendations for other floater designs. A further discussion of limitations and improvements is given in the future work chapter.

5.4 Future Work

Despite achieving the overall goal, there are still improvements due to aspects that haven't been captured within the thesis or captured incorrectly. These possible improvements are explained in the following section.

First of all, the modelling mistake for the flexible floater design identified in subsection 3.1.6 should be resolved in order to create a reliable reference model for wave conditions. A general approach to this is described in the same chapter; however, a clear approach on how to implement this in OrcaFlex is missing. Additionally, the difference due to the missing *other damping* terms should be included for all designs when rerunning the simulations, despite being identified as negligible for the investigated cases. Correcting this mistake allows one to compare the results of the flexible element designs under wave conditions not only to each other but also to a reference case. This could give further insight on which configuration performs best, even though the differences between the designs have already been evaluated as small.

Two additional terms can be addressed in terms of creating the flexible element designs. The first is to try and force a design that results in a worse match of the tower mode shape while still maintaining a match in the tower's first natural frequency. This allows getting a deeper insight into the impact of the tower's first mode shape on the tower dynamics. Additionally, the *while loop* used in the process of creating the flexible element has proven to be an efficient and fast tool, allowing for the creation of many designs with a resulting tower first bending frequency within + 0.01 Hz accuracy. However, it seems that increasing the accuracy could result in better matches, and hence a smaller step size could be considered in the *while loop*.

A possible next step is to apply the learnings from this thesis about designing a flexible element with an as good a match in tower mode shape as possible to a different floater design. Specifically focusing on the conclusion that matching the Young's modulus of the floater part that is connected to the tower (assuming an identical second moment of area) yields good results. This would confirm whether the conclusions are generally applicable or bound to the examined floater type.

One of the discussed approaches to identify the tower's first bending mode was to simplify the model such that the number of flexible elements is reduced allowing to focus on the tower mode shapes. This approach was not fully implemented due to difficulties in simplifying the model and a different focus of the thesis work. Simplifying the model could result in a further method of identifying the tower's first mode and also identify the impact the different components have on the tower modes.

The time domain results showed good agreement between the flexible element designs and the flexible floater design for bending moment and tower top rotation. The same was found for the tower

top acceleration; however, it is less significant. This is expected to stem from the fact that higher-order modes are responsible for capturing the acceleration. The current work solely focuses on the first tower mode. Hence, a further step is to tune the flexible elements not only for the first tower mode but also for higher modes.

Lastly, a further study on different approaches to mimicking the floater flexibility could be tested. One of these approaches would be, for example, a spring element with a certain stiffness. This could further simplify the mode. The spring does not even have to be necessarily linear. Using a spring with non-linear stiffness could potentially allow one to achieve a good result of mode shapes of modes of different orders.

Bibliography

Abdelnour, M., & Zabel, V. (2024). Modal identification of structures with a dynamic behaviour characterised by global and local modes at close frequencies. *Acta Mechanica*, *235*(3), 1471–1491. https://doi.org/10.1007/s00707-023-03598-z

Allen, C., Viscelli, A., Dagher, H., Goupee, A., Gaertner, E., Abbas, N., Hall, M., & Barter, G. (2020, July). *Definition of the UMaine VolturnUS-S Reference Platform Developed for the IEA Wind 15-Megawatt Offshore Reference Wind Turbine* (tech. rep. No. NREL/TP–5000-76773, 1660012, MainId:9434). https://doi.org/10.2172/1660012

Al-Solihat, M. K., & Nahon, M. (2014). Mooring and hydrostatic restoring of offshore floating wind turbine platforms. *2014 Oceans - St. John's*, 1–5. https://doi.org/10.1109/OCEANS.2014.7003269

Arany, L., Bhattacharya, S., Macdonald, J. H., & Hogan, S. J. (2016). Closed form solution of Eigen frequency of monopile supported offshore wind turbines in deeper waters incorporating stiffness of substructure and SSI. *Soil Dynamics and Earthquake Engineering*, *83*, 18–32. https://doi.org/10.1016/j.soildyn.2015.12.011

Bachynski-Polic, E. E. (2021). Lecture note: Assessing the results from decay tests.

Backwell, B., Lee, J., Patel, A., Qiao, L., Nguyen, T., Liang, W., Fang, E., Cheong, J., Tan, W. H., Francisco, A. M., Bui, T. V., Nguyen, T., Fiestas, R., Cox, R., de Lima, J. P., Rabie, H., Ladwa, R., Madan, K., Muchiri, W., … Yamamura, J. (2024). Global Offshore Wind Report 2024.

Benitz, M., Lackner, M., & Schmidt, D. (2015). Hydrodynamics of offshore structures with specific focus on wind energy applications. *Renewable and Sustainable Energy Reviews*, *44*, 692–716. https://doi.org/10.1016/j.rser.2015.01.021

Bir, G., & Jonkman, J. (2008). Modal Dynamics of Large Wind Turbines With Different Support Structures. *Volume 6: Nick Newman Symposium on Marine Hydrodynamics; Yoshida and Maeda Special Symposium on Ocean Space Utilization; Special Symposium on Offshore Renewable Energy*, 669–679. https://doi.org/10.1115/OMAE2008-57446

Borg, M., & Collu, M. (2015). A comparison between the dynamics of horizontal and vertical axis offshore floating wind turbines. *Philosophical Transactions of the Royal Society A: Mathematical, Physical and Engineering Sciences*, *373*(2035), 20140076. https://doi.org/10.1098/rsta.2014.0076

Brown, D. T. (2005). Chapter 8 - mooring systems. In S. K. CHAKRABARTI (Ed.), *Handbook of offshore engineering* (pp. 663–708). Elsevier. https://doi.org/https://doi.org/10.1016/B978-0-08-044381-2.50015-1

Butterfield, S., Solavounos, P., & Jonkman, J. (2007). Engineering Challenges for Floating Offshore Wind Turbines.

Commission, I. E. (2019). IEC 61400-1 Wind energy generation systems - Part 1: Design requirements.

Cordle, A., & Jonkman, J. (2011). State of the Art in Floating Wind Turbine Design Tools.

Engebretsen, E., Haslum, H., & Aagaard, O. (2020). Distributed Potential Theory and its Application for Spar-Type Floating Offshore Wind Turbines. *Volume 1: Offshore Technology*, V001T01A062. https://doi.org/10.1115/OMAE2020-18284

Eriksen, R. (2022). ENERGY TRANSITION OUTLOOK 2022.

Faltinsen, O. M. (1999). *Sea loads on ships and offshore structures* (1. paperback ed., repr., transferred to digital printing). Cambridge University Press.

Feng, R., Yan, G., & Ge, J. (2012). Effects of high modes on the wind-induced response of super high-rise buildings. *Earthquake Engineering and Engineering Vibration*, *11*(3), 427–434. https://doi.org/10.1007/s11803-012-0132-2

Fossen, T. I. (2011). *HANDBOOK OF MARINE CRAFT HYDRODYNAMICS AND MOTION CONTROL* (First Edition). John Wiley & Sons, Ltd.

Gaertner, E., Rinker, J., Sethuraman, L., Zahle, F., Anderson, B., Barter, G., Abbas, N., Meng, F., Bortolotti, P., Skrzypinski, W., Scott, G., Feil, R., Bredmose, H., Dykes, K., Shields, M., Allen, C., & Viselli, A. (2020). Definition of the IEA 15-Megawatt Offshore Reference Wind. https://www.nrel.gov/docs/fy20osti/75698.pdf

Gao, S., Zhang, L., Shi, W., Wang, W., Wang, B., & Li, X. (2024). Dynamic Analysis of a 10 MW Floating Offshore Wind Turbine Considering the Tower and Platform Flexibility. *Journal of Ocean University of China*, *23*(2), 358–370. https://doi.org/10.1007/s11802-024-5604-2

Gavin, H. P. (2012). Review of Strain Energy Methods and Introduction to Stiffness Matrix Methods of Structural Analysis.

Harger, A., Carmo, L. H. S., Gay Neto, A., Simos, A. N., Franzini, G. R., & Vieira, G. H. R. (2023). Modal Analysis of 15 MW Semi-Submersible Floating Wind Turbine: Investigation on the Main Influences in Natural Vibration. *Wind*, *3*(4), 548–566. https://doi.org/10.3390/wind3040031

Hsu, C.-G. (2019, July). *Substructure Models for Dynamic Analysis of Floating Wind Turbines and the Effect of Hull Flexibility* [Master's thesis, Norwegian University of Science and Technology / TU Delft]. http://refhub.elsevier.com/S0951-8339(22)00025-9/sb30

Iijima, K., Srinivasamurthy, S., & Fujikubo, M. (2016). Structural modeling for flexible floating offshore wind turbine: Flexible model vs rigid model. *2016 Techno-Ocean (Techno-Ocean)*, 280–283. https://doi.org/10.1109/Techno-Ocean.2016.7890662

International Renewable Energy Agency (IRENA). (2016). Floating Foundations: A Game Changer for Offshore Wind Power.

IRENA. (2023). *World Energy Transitions Outlook 2023: 1.5°C Pathway*. https://www.irena.org/Publications/2023/Jun/World-Energy-Transitions-Outlook-2023

Jahani, K., Langlois, R. G., & Afagh, F. F. (2022). Structural dynamics of offshore Wind Turbines: A review. *Ocean Engineering*, *251*, 111136. https://doi.org/10.1016/j.oceaneng.2022.111136

Jonkman, J. M. (2009). Dynamics of offshore floating wind turbines—model development and verification. *Wind Energy*, *12*(5), 459–492. https://doi.org/10.1002/we.347

Kiriparan, B., Jayasinghe, J. A. S. C., & Dissanayake, U. I. (2021). Comparative Study of the Wind Codes: An Application to Forty-Six Storied Wall-Frame Structure. *Engineer: Journal of the Institution of Engineers, Sri Lanka*, *54*(4), 37. https://doi.org/10.4038/engineer.v54i4.7469

Leimeister, M. (2022). *Reliability-Based Optimization of Floating Wind Turbine Support Structures*. Springer International Publishing. https://doi.org/10.1007/978-3-030-96889-2

Li, H., Gao, Z., Bachynski-Polić, E. E., Zhao, Y., & Fiskvik, S. (2023). Effect of floater flexibility on global dynamic responses of a 15-MW semi-submersible floating wind turbine. *Ocean Engineering*, *286*, 115584. https://doi.org/10.1016/j.oceaneng.2023.115584

Liu, Y., & Ishihara, T. (2020). Numerical Study on Sectional Loads and Structural Optimization of an Elastic Semi-Submersible Floating Platform. *Energies 2021*, 14, 182.

Mann, J. (1994). The spatial structure of neutral atmospheric surface-layer turbulence. *Journal of Fluid Mechanics*, *273*, 141–168. https://doi.org/10.1017/S0022112094001886

Muskulus, M. (2023). Dynamic response to irregular loadings.

Nieto, M., Elsayed, M., & Walch, D. (2018). Modal Participation Factors And Their Potential Applications In Aerospace: A Review. *Progress in Canadian Mechanical Engineering*. https://doi.org/10.25071/10315/35254

Nybø, A., Nielsen, F., & Godvik, M. (2021). Analysis of turbulence models fitted to site, and their impact on the response of a bottom-fixed wind turbine. *Journal of Physics: Conference Series*, *2018*(1), 012028. https://doi.org/10.1088/1742-6596/2018/1/012028

Pastor, M., Binda, M., & Harčarik, T. (2012). Modal Assurance Criterion. *Procedia Engineering*, *48*, 543–548. https://doi.org/10.1016/j.proeng.2012.09.551

Ran, X., Leroy, V., & Bachynski-Polić, E. E. (2023). Hydroelastic response of a flexible spar floating wind turbine: Numerical modelling and validation. *Ocean Engineering*, *286*, 115635. https://doi.org/10.1016/j.oceaneng.2023.115635

Ross, A., & McKinnon, G. (2018). Orcina Project 1405 Wind Turbine Validation Report.

Sarpkaya, T., & Isaacson, M. (1982). Mechanics of Wave Forces on Offshore Structures. *Journal of Applied Mechanics*, *49*(2), 466–467. https://doi.org/10.1115/1.3162189

Shen, J. Y., Sharpe, L., & Taylor, L. W. (1993). A strain-energy criterion for recognition of identified modes of continuous structural models. *Mechanics Research Communications*, *20*(6), 507–518. https://doi.org/10.1016/0093-6413(93)90011-C

Sizova, S., Maillot, E., Moreau, S., & Féron, M. (2022). Influence of the Semi-Submersible Platform Flexibility on the Dynamic Response of the Wind Turbine. *Volume 8: Ocean Renewable Energy*, V008T09A028. https://doi.org/10.1115/OMAE2022-79124

Soares-Ramos, E. P., De Oliveira-Assis, L., Sarrias-Mena, R., & Fernández-Ramírez, L. M. (2020). Current status and future trends of offshore wind power in Europe. *Energy*, *202*, 117787. https://doi.org/10.1016/j.energy.2020.117787

Subbulakshmi, A., Verma, M., Keerthana, M., Sasmal, S., Harikrishna, P., & Kapuria, S. (2022). Recent advances in experimental and numerical methods for dynamic analysis of floating offshore wind turbines — An integrated review. *Renewable and Sustainable Energy Reviews*, *164*, 112525. https://doi.org/10.1016/j.rser.2022.112525

Van Der Tempel, J., & Molenaar, D.-P. (2002). Wind Turbine Structural Dynamics – A Review of the Principles for Modern Power Generation, Onshore and Offshore. *Wind Engineering*, *26*(4), 211–222. https://doi.org/10.1260/030952402321039412

Wu, X., Hu, Y., Li, Y., Yang, J., Duan, L., Wang, T., Adcock, T., Jiang, Z., Gao, Z., Lin, Z., Borthwick, A., & Liao, S. (2019). Foundations of offshore wind turbines: A review. *Renewable and Sustainable Energy Reviews*, *104*, 379–393. https://doi.org/10.1016/j.rser.2019.01.012

Yamaguchi, A., Danupon, S., & Ishihara, T. (2022). Numerical Prediction of Tower Loading of Floating Offshore Wind Turbine Considering Effects of Wind and Wave. *Energies 2022*, 15. https://doi.org/https://doi.org/10.3390/en15072313

Appendix A

Additional Material

A.1 Use of AI Tools in Thesis Development

Various AI tools have been used in the thesis. As the capabilities and reliability of AI's are limited it was not used as a source of knowledge or for the creation of new code. Instead, the AI tools have been utilised as supporting tools. The following tools have been used for the explained cases:

- Optimizing plot layouts in Python using ChatGPT
- Create subfigures and fill out tables with new data in Overleaf using ChatGPT
- Grammar and spell checking of the text using QuillBot

An additional form on the usage of AI tools provided by NTNU is included on the next page.

NTNU

Declaration of AI aids and tools

Have any AI-based aids or tools been used in the creation of this report?

No ✓ Yes

If yes: please specify the aid/tool and area of use below.

Text

✓ **Spell checking.** Are parts of the text checked by: Grammarly, Ginger, Grammarbot, LanguageTool, ProWritingAid, Sapling, Trinka AI or similar tools?

Text-generation. Are parts of the text generated by: ChatGPT, GrammarlyGO, Copy.AI, WordAi, WriteSonic, Jasper, Simplified, Rytr or similar tools?

Writing assistance. Are one or more of the report's ideas or approach suggested by: ChatGPT, Google Bard, Bing chat, YouChat or similar tools?

If no, sign document. If yes, use of text aids/tools apply to this report -please specify usage here:

Grammar and spell checking of the text using QuillBot.

Codes and algorithms

✓ **Programming assistance.** Are parts of the codes/algorithms that i) appear directly in the report or ii)have been used to produce results such as figures, tables or numerical values been generated by: GitHub Copilot, CodeGPT, Google Codey/Studio Bot, Replit Ghostwriter, Amazon CodeWhisperer, GPTEngineer, ChatGPT, Google Bard or other tools.

If yes, use of programming assistance aid/tools apply to this report - please specify usage here:

Optimizing plot layouts in Python using ChatGPT

Images and figures

Image generation. Are one or more of the reports images/figures generated by: Midjourney, Jasper, WriteSonic, Stability AI, Dall-E or similar tools?

If yes, use of image generator aids/tools apply to this report – please specify usage here:

Other AI aids or tools. Have you used other types of AI aids or tools in the creation of this report?
If yes, please specify usage here:

reate subfigures and fill out tables with new data in Overleaf using ChatGPT

✓ I am familiar with NTNU's regulations on artificial intelligence. I declare that any use of AI aids or tools are explicitly stated i) directly in the report or ii) in this declaration form.

Friedrich Feisch / 30.06.25 / Delft

Signature/Date/Place

A.2 Component properties

Table A.1: Centre column input parameters for *OrcaFlex*.

Inner diameter	10 m
Outer diameter	9.91 m
Mass per lid	27.93 $\times 10^3$ kg
Mass connector piece	100 $\times 10^3$ kg

Table A.2: Arm input parameters for *OrcaFlex*.

Inner diameter	10 m
Outer diameter	9.91 m
Arm length	40.5 m
Mass per meter	14.55 kg/m
Bending stiffness around local x-axis	7.75×10^{12} Nm^2
Bending stiffness around local y-axis	3.22×10^{12} Nm^2
Axial stiffness	$349,38 \times 10^9$ N

Table A.3: Side column input parameters for *OrcaFlex*.

Inner diameter	12.5 m
Outer diameter	12.41 m
Mass per lid	43.64 $\times 10^3$ kg
Additional volume per side column	367.89 m^3

Table A.4: Struts input parameters for *OrcaFlex*.

Inner diameter	0.91 m
Outer diameter	0.82 m
Mass per lid	43.64 $\times 10^3$ kg
Additional volume per side column	367.89 m^3

A.3 Tower mass matrix

In order to identify the tower modes using the approach explained in section 3.1.7 the tower mass matrix needs to be defined. OrcaFlex does not give direct access to the mass matrix and hence, the tower mass matrix is also not available. The mass matrix is rebuild using Equation A.1 for a lumped node. This is done for each tower mode and they are combined into a global mass matrix.

$$\begin{bmatrix} m & 0 & 0 & 0 & zm & -ym \\ 0 & m & 0 & -zm & 0 & xm \\ 0 & 0 & m & ym & -xm & 0 \\ 0 & -zm & ym & J_{xx}+m(y^2+z^2) & J_{xy}-mxy & J_{xz}-mxz \\ zm & 0 & -xm & J_{xy}-mxy & J_{yy}+m(x^2+z^2) & J_{yz}-myz \\ -ym & xm & 0 & J_{xz}-mxz & J_{yz}-myz & J_{zz}+m(x^2+y^2) \end{bmatrix} \tag{A.1}$$

m is the mass of that node, which is calculated using m_{bar} and the half the length of the segment below and above each node. No parallel axis theorem needs to be applied, as the mass is already localized at the node itself. Hence, x, y and z are all zero. Only the moment of inertia for a hollow cylinder around its different axis needs to be determined, which is found to be:

$$I_{xx} = I_{yy} = \frac{1}{4} * m_{Node} * (r^2_{Node,Outer} + r^2_{Node,Inner}) + \frac{1}{12} * m_{Node} * l^2_{Segement} \tag{A.2}$$

$$I_{zz} = \frac{1}{2} * m_{Node} * (r^2_{Node,Outer} + r^2_{Node,Inner}) \tag{A.3}$$

The resulting tower mass matrix was validated by adding the mass for each node and comparing it to the total tower mass. An exact match was found. Additionally, a simple model was set-up in OrcaFlex, where the tower is the only element and is clamped at the bottom. The mode shape vectors are extracted, and together with the tower mass matrix the modal mass is calculated according to Equation 2.7. The results are compared to the modal mass reported by OrcaFlex, and differences up to a max difference of 7.6% were found. A table containing the quotient between the calculated modal mass and reported modal mass for different modes is reported in Figure A.1. Deviations below 1.2 % were found for axial bending, where solely translational displacement is taking place, confirming the correctness of the entries in the mass matrix related to translation movements. The results for bending and torsional modes are not as similar indicating that some inertia terms are not completely identical. However, overall good agreement was found validating the mass matrix.

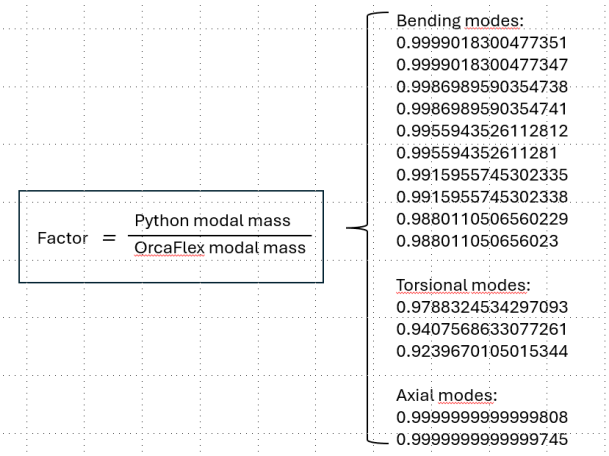

Figure A.1: Mass matrix validation using modal mass.

A.4 Simplified model

The simplified model method explained in section 3.1.7 requires to replace all flexible components that are not of interest with rigid bodies. In the case of this thesis the noise stems from the blades and mooring lines. Hence, they are replaced by rigid components that capture mass, CoG and moment of inertia in a mass point. Such a mass point is modelled in OrcaFlex through a *6D buoy type*.

The blades properties are defined within the *turbine type*. They are replaced by a *6D buoy type* with identical mass, CoG and moment of inertia. These properties are simply determined by using the *compound property* tool in OrcaFlex. The properties of the *6D buoy* replacement are summarized in Table A.5.

Table A.5: *6D buoy* rigid blades data.

Mass [t]	**Mass moments of inertia [tm^2]**			**CoG [m]**		
	x	**y**	**z**	**x**	**y**	**z**
274.6	175.1×10^3	175.1×10^3	346.8×10^3	0	0	-1.6

Replacing the mooring lines is more challenging, as they not only contribute with their mass but also their stiffness. The mass is again captured by adding a *6D buoy* with identical mass, CoG and moment of inertia. Not the total mass of the mooring lines is considered for this, but only the part that is not resting on sea bed. In static equilibrium that is 330 m of the total 850 m. The properties of the *6D buoy* replacement that summarises mass, inertia and CoG are summarized in Table A.6.

Table A.6: *6D buoy* rigid mooring lines data.

Mass [t]	**Mass moments of inertia [tm^2]**			**CoG [m]**		
	x	**y**	**z**	**x**	**y**	**z**
1746.8	207×10^6	207×10^6	405.2×10^6	0	0	-171.4

The mooring stiffness acting on the floater is reported in OrcaFlex as a **6x6** matrix (Equation A.4). This stiffness matrix is captured by including *link types*. They are mass less springs and can be set to have a constant stiffness. Three springs are attached at each fairlead. One for each translational Degree of Freedom. The stiffness of the springs is calculated by dividing the corresponding entry of the Equation A.4 by three. The rotational DoF and coupled terms are assumed to be captured correctly, since fairlead position and stiffness in each translational direction are identical. Figure A.2 shows the setup with rigid floater, blades and mooring lines. A detailed derivation of the stiffness matrix for the simplified low fidelity model is provided below.

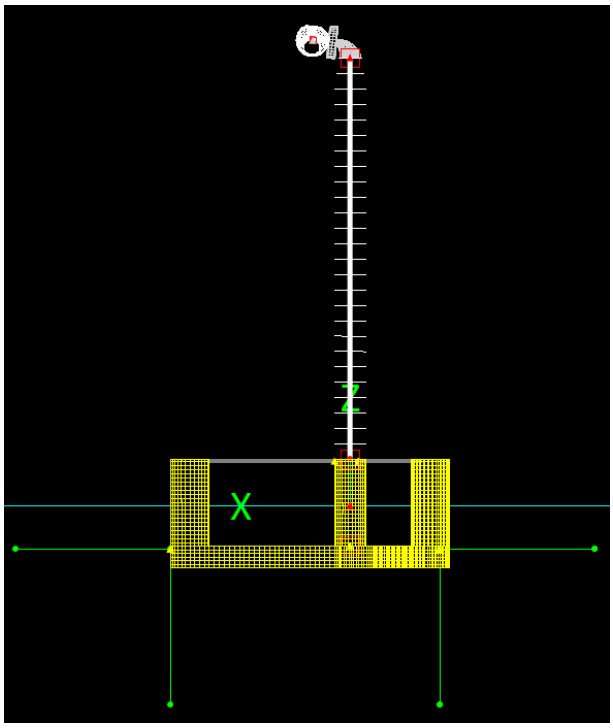

Figure A.2: Simplified model RRR: Rigid floater, Rigid blades and Rigid mooring lines.

Mooring stiffness matrix reported from OrcaFlex. In contrast to the stiffness matrix from Al-Solihat and Nahon, 2014 more values are non-zero, indicating more coupling between different DoF.

$$\begin{bmatrix} 77.9461 & 0.0098 & 1.0384 & -0.9541 & 1091.6419 & 0.4420 \\ 0.0088 & 79.0276 & 0.0133 & -1220.0299 & 0.9273 & -32.5038 \\ 0.8823 & 0.0129 & 63.7742 & -1.6614 & 115.5672 & -0.0100 \\ -0.9554 & -1226.4092 & -1.6513 & -1.9686 \times 10^{6} & -53.2441 & 1.2164 \times 10^{5} \\ 1088.8041 & 0.9545 & 113.4501 & -54.3886 & -1.9741 \times 10^{6} & 1687.9598 \\ 0.4066 & -21.4538 & 0.0377 & 3694.0444 & 55.7900 & 2.8115 \times 10^{5} \end{bmatrix} \tag{A.4}$$

The stiffness matrix can be, as explained section 2.3 split into four **3x3** blocks. Simplifying the output from OrcaFlex by only keeping those values inside each block that are larger than 1/10 of the max value in that block, one gets the following matrix:

$$\begin{bmatrix} 77.95 & 0 & 0 & 0 & 1091.64 & 0 \\ 0 & 79.03 & 0 & -1220.03 & 0 & 0 \\ 0 & 0 & 63.77 & 0 & 0 & 0 \\ 0 & -1226.41 & 0 & -1.97 \times 10^{6} & 0 & 0 \\ 1088.80 & 0 & 0 & 0 & -1.97 \times 10^{6} & 0 \\ 0 & 0 & 0 & 0 & 0 & 2.81 \times 10^{5} \end{bmatrix} \tag{A.5}$$

This matrix resembles the theory form Al-Solihat and Nahon, 2014.

The units are identical for each **3x3** block and are shown in the additional matrix below.

$$\begin{bmatrix} \frac{\text{kN}}{\text{m}} & \frac{\text{kN}}{\text{rad}} \\ \frac{\text{kNm}}{\text{m}} & \frac{\text{kNm}}{\text{rad}} \end{bmatrix} \tag{A.6}$$

The new simplified mooring system is build by replacing each mooring line with a set of three mooring lines, one for each translational DoF. The position of the fairlead stays identical. The following figure shows the set-up from side view and top view. It includes the spring replacements and the most important dimensions. The Roman letters define the leg number, whereas the Arabic numbers define the DoF. The origin of the coordinate system is at the centre of the floater at SWL.

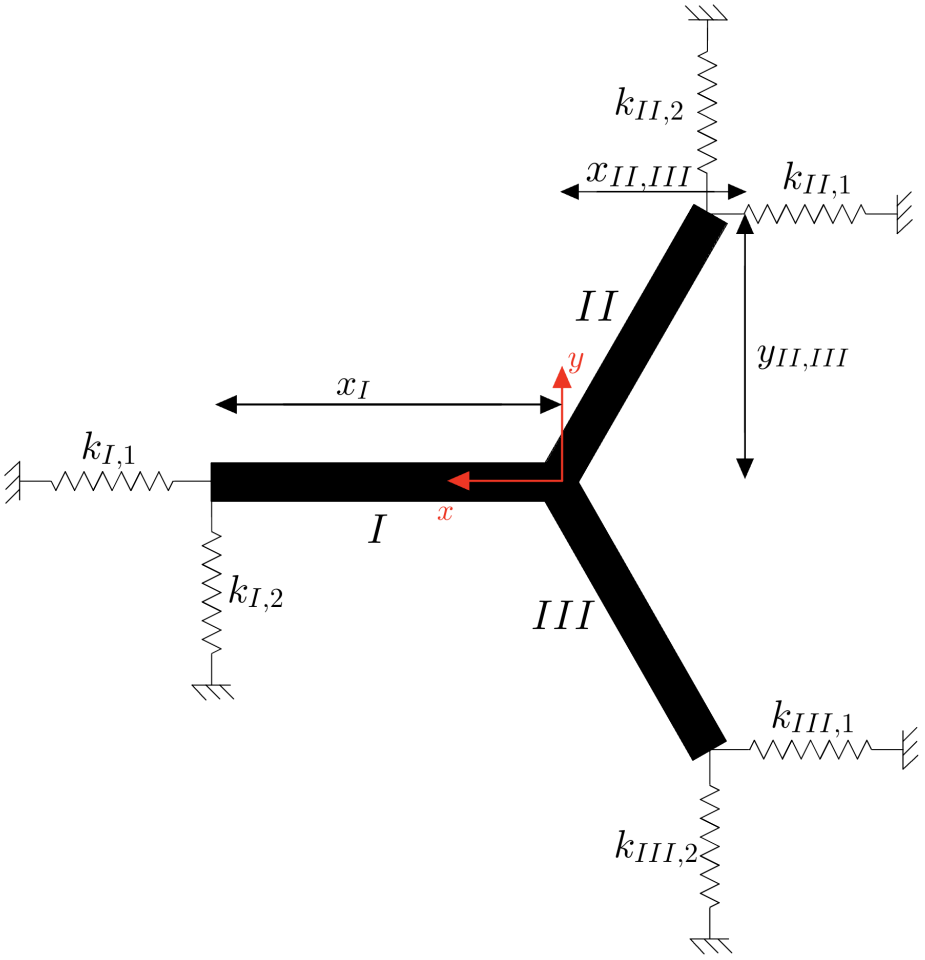

Figure A.3: Schematic top view of floater showing springs.

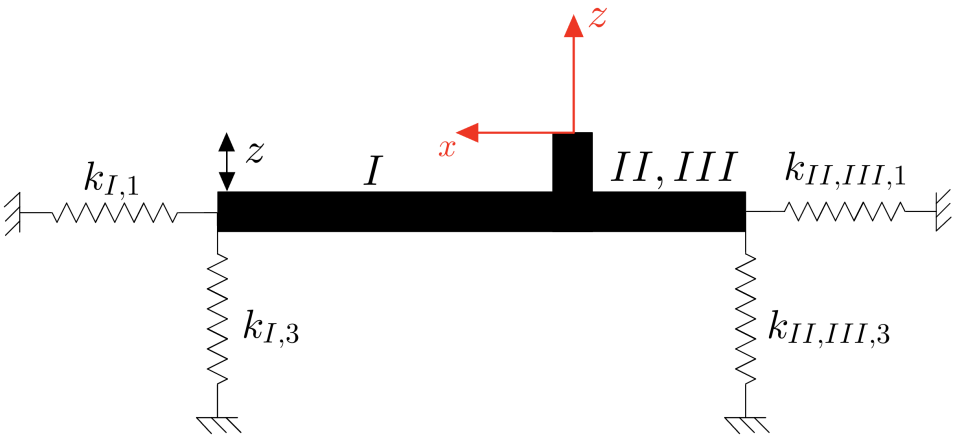

Figure A.4: Schematic side view of floater showing springs.

The values for the variables are defined as:

$$\begin{aligned} k_{I,1} = k_{II,1} = k_{III,1} = k_1 &= 25.98 \frac{\text{kN}}{\text{m}} \\ k_{I,2} = k_{II,2} = k_{III,2} = k_2 &= 26.34 \frac{\text{kN}}{\text{m}} \\ k_{I,3} = k_{II,3} = k_{III,3} = k_3 &= 21.26 \frac{\text{kN}}{\text{m}} \\ x_I &= 58\text{m} \\ x_{II,III} &= 29\text{m} = 2 \cdot x_I \\ y_{II,III} &= 50.23\text{m} \\ z &= 14\text{m} \end{aligned} \tag{A.7}$$

Starting point is the general stiffness matrix for a system with 6 DoF:

$$\begin{bmatrix} k_{11} & k_{12} & k_{13} & k_{14} & k_{15} & k_{16} \\ k_{21} & k_{22} & k_{23} & k_{24} & k_{25} & k_{26} \\ k_{31} & k_{32} & k_{33} & k_{34} & k_{35} & k_{36} \\ k_{41} & k_{42} & k_{43} & k_{44} & k_{45} & k_{46} \\ k_{51} & k_{52} & k_{53} & k_{54} & k_{55} & k_{56} \\ k_{61} & k_{62} & k_{63} & k_{64} & k_{65} & k_{66} \end{bmatrix} \tag{A.8}$$

Assuming a symmetric matrix the following equations are found for the single entries:

$$
\begin{aligned}
k_{11} &\approx 3k_1 \\
k_{12} = k_{21} &\approx 0 \\
k_{13} = k_{31} &\approx 0 \\
k_{14} = k_{41} &\approx 0 \\
k_{15} = k_{51} &\approx 3k_1 z \\
k_{16} = k_{61} &\approx k_1 y_{II,III} - k_1 y_{II,III} = 0 \\
k_{22} &\approx 3k_2 \\
k_{23} = k_{32} &\approx 0 \\
k_{24} &\approx 3k_2 z \\
k_{25} = k_{52} &\approx 0 \\
k_{26} = k_{62} &\approx k_2 x_I - (k_2 + k_2) x_{II,III} \\
&= k_2 (x_I - 2x_{II,III}) = 0 \\
k_{33} &\approx 3k_3 \\
k_{34} = k_{43} &\approx k_3 y_{II,III} - k_3 y_{II,III} = 0 \\
k_{35} = k_{53} &\approx k_3 x_I - (k_3 + k_3) x_{II,III} \\
&= k_3 (x_I - 2x_{II,III}) = 0
\end{aligned}
\tag{A.9}
$$

In order to get the rotational stiffness terms correct the following two graphics are added, showing the floater in a displaced position:

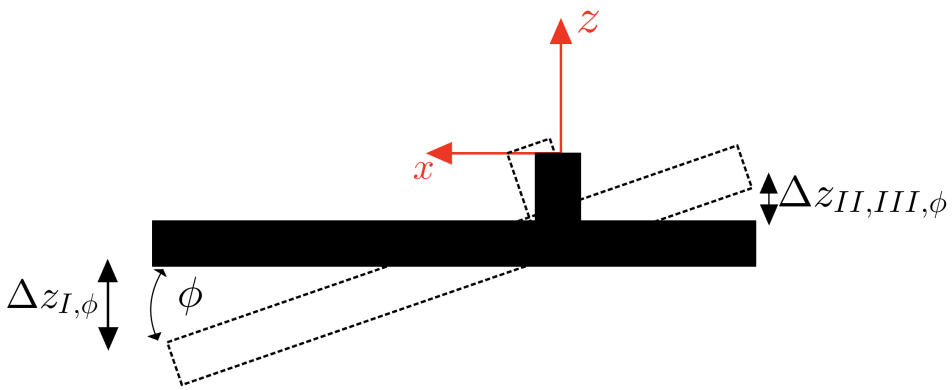

Figure A.5: Schematic side view of floater in displaced state.

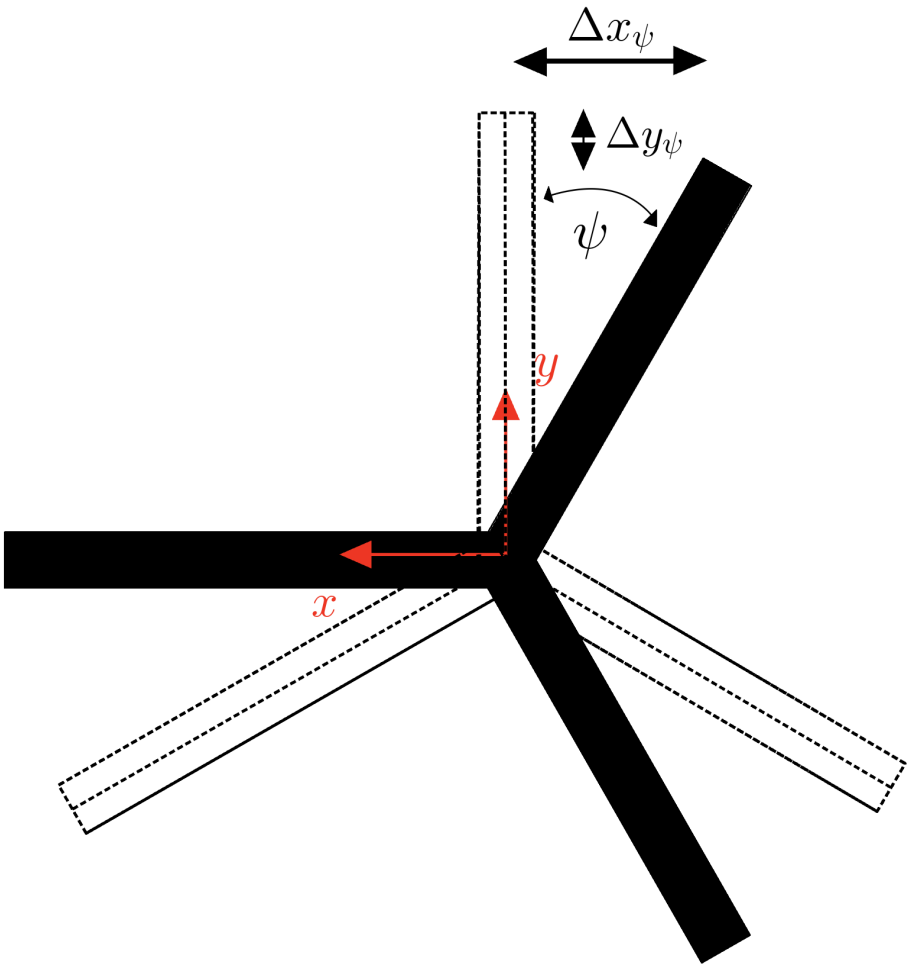

Figure A.6: Schematic top view of floater in displaced state.

This gives the rotational terms as:

$$
\begin{aligned}
k_{44} &= \Delta z_{II,III,\theta}(k_3 + k_3) y_{II,III} \\
&= 2\Delta z_{II,III,\theta} k_3 y_{II,III}^2 \sin(\theta) \\
&\quad \text{with} \\
&\qquad \Delta z_{II,III,\theta} = y_{II,III} \sin(\theta) \\
k_{45} &= k_{54} \approx 0 \\
k_{46} &= k_{64} \approx 0 \\
k_{55} &= \Delta z_{I,\phi} k_3 x_I + \Delta z_{II,III,\phi}(k_3 + k_3) x_{II,III} \\
&= k_3 \sin(\phi)(x_I^2 + 2x_{II,III}^2) \\
&\quad \text{with} \\
&\qquad \Delta z_{I,\phi} = x_I \sin(\phi) \\
&\qquad \Delta z_{II,III,\phi} = x_{II,III} \sin(\phi) \\
k_{66} &= 3k_1 \Delta x_\psi - 3k_2 \Delta y_{II,III,\psi} \\
&\quad \text{with} \\
&\qquad \Delta x_\psi = x_I \sin(\psi) \\
&\qquad \Delta y_{II,III,\psi} = x_I \cos(\psi) - y_{I,II}
\end{aligned}
\tag{A.10}
$$

A.5 Comparison of tower natural frequency with literature using similar model set up.

In principle all papers use the same floater; however, modifications have been performed in the case of this thesis, and different assumptions are made. The different tower first bending natural frequencies are reported in Table A.7.

Table A.7: Tower first bending natural frequency of flexible floater compared to rigid floater case and different studies.

	Flexible Floater	Rigid Floater
Thesis	0.408 Hz	0.451 Hz
Pre-Thesis (Decay)	0.37 Hz	0.444 Hz
Harger et al., 2023	0.429 Hz	0.462 Hz
Li et al., 2023	0.38 Hz	0.41 Hz

Looking at the results from Table A.7 many different results are evident. The margin by which the tower's first bending natural frequency increases is in the same range for all cases, with slightly more increase for the thesis and pre-thesis.

Firstly, the difference between thesis and pre-thesis must be addressed. One big problem with the pre-thesis was that *modal analysis* tool from OrcaFlex was used wrong, resulting in an added mass of zero. This has a big impact on the tower's first bending natural frequency, according to Harger et al., 2023. Hence, only the results from the decay test are reported in Table A.7. Working in the time domain, the decay test includes the added mass.

Additionally to this, other flaws have been found in the pre-thesis that were adjusted in this

thesis. One of these is the accuracy of the flexible floater's CoG, CoB, displaced volume and line segmentation to match the rigid body motions. These differences are identified as sources for the observed differences in tower first bending natural frequency between the flexible designs.

The rigid floater design, on the other hand, is provided by OrcaFlex in both cases. However, the inertia of the rigid floater was decreased for this thesis to get a match between the flexible and rigid model. According to Harger et al., 2023 the inertia is a key contributor to the tower's first bending natural frequency. They observe an increase in tower natural frequency with a decrease in inertia. Hence, this decrease in moment of inertia explains the slight increase in tower natural frequency.

Compared to Harger et al., 2023 the thesis results show a lower tower first bending natural frequency for both designs, flexible and rigid. The biggest difference between Harger et al., 2023 and this thesis is the assumption of a rigid Rotor-Nacelle Assembly (RNA) that could possibly explain the difference.

Lastly, the difference between the thesis and Li et al., 2023 is discussed. The values found in Li et al., 2023 are lower than the ones found in the thesis. The inertia of the UMaine floater was lowered for this thesis, as previously mentioned. Recalling, the effect of a lower inertia resulting in an increase of tower natural frequency from Harger et al., 2023 this difference could potentially explain the difference, even though the magnitude of the change is not easily detectable.

A.6 Segment Length Mode Shapes

Following presents the mode shape results over the amount of segments for 2.5 m, 5.0 m and 7.5 m total length.

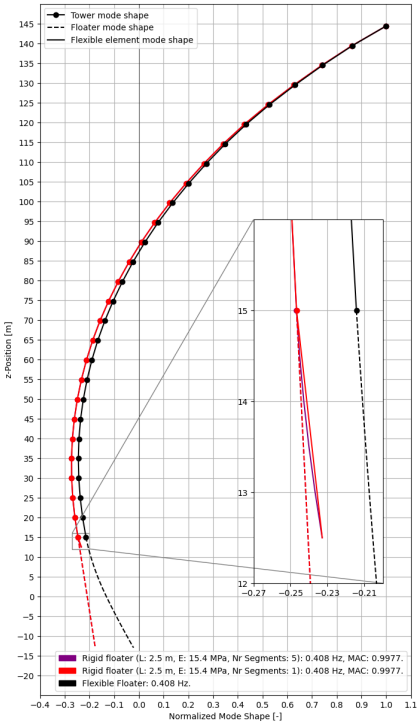

(a) Mode shape variation over segment variation for a total length of 2.5 m.

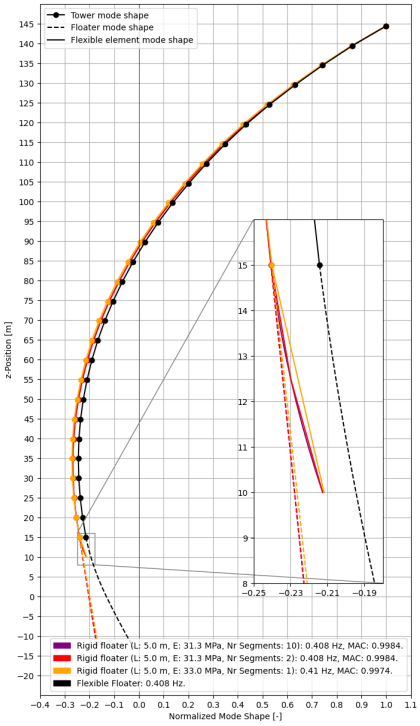

(b) Mode shape variation over segment variation for a total length of 5.0 m.

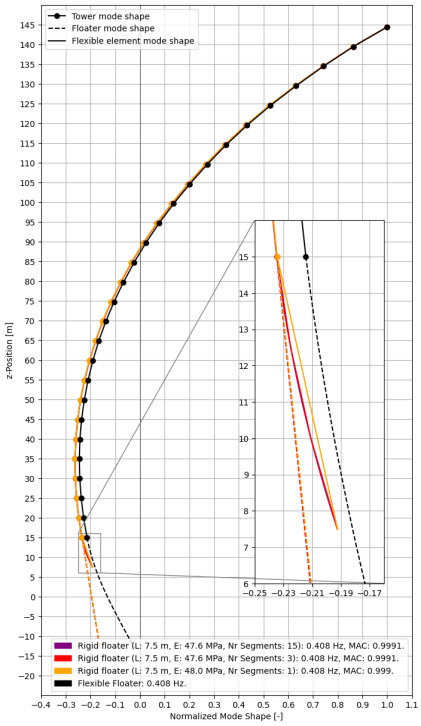

(c) Mode shape variation over segment variation for a total length of 7.5 m.

Figure A.7: Mode shape variation over segment length for different total lengths.

A.7 Element Composition Mode Shapes

Following presents the mode shape results of the soft hard configurations for 2.5 m, 5.0 m and 7.5 m total length.

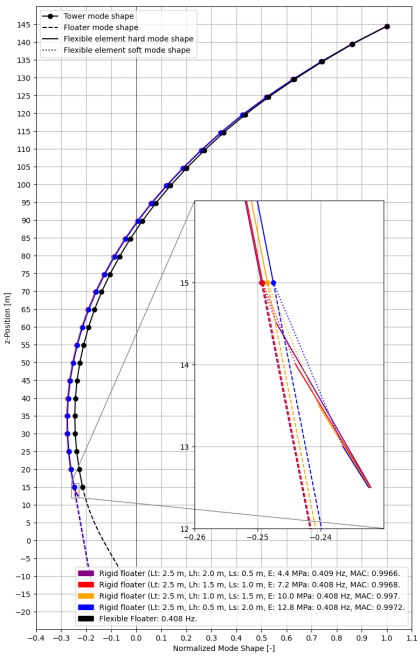

(a) Mode shape variation over soft hard ratio for a total length of 2.5 m.

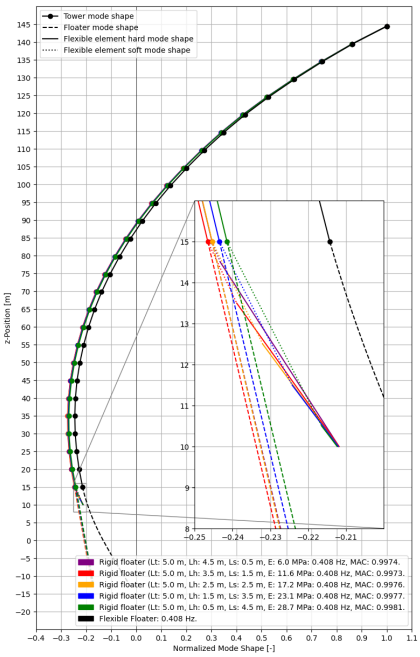

(b) Mode shape variation over soft hard ratio for a total length of 5.0 m.

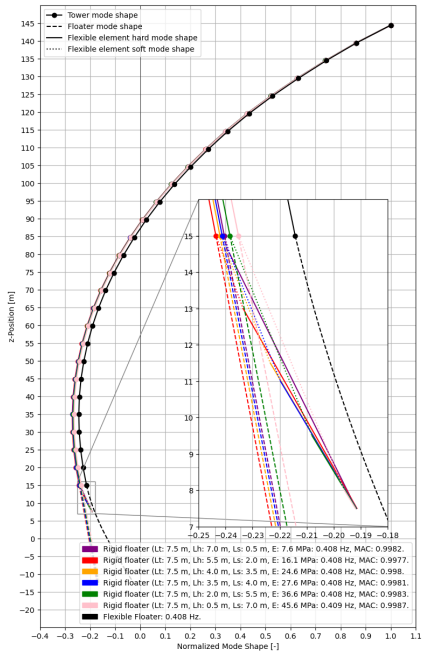

(c) Mode shape variation over soft hard ratio for a total length of 7.5 m.

Figure A.8: Mode shape variation over hard stiff ratio for different total lengths.

Following presents the mode shape results of the hard soft configurations for 2.5 m, 5.0 m and 7.5 m total length.

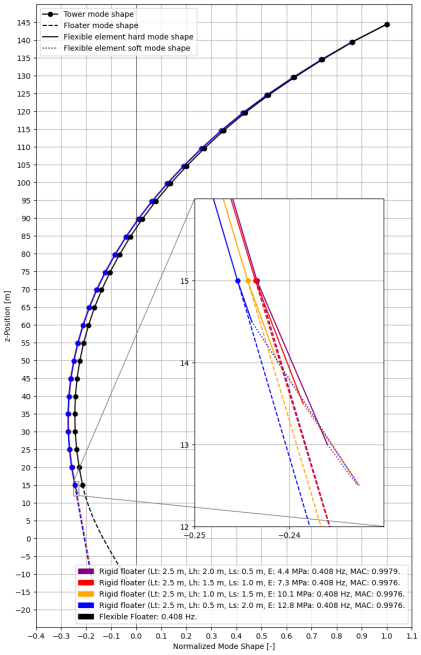

(a) Mode shape variation over hard soft ratio for a total length of 2.5 m.

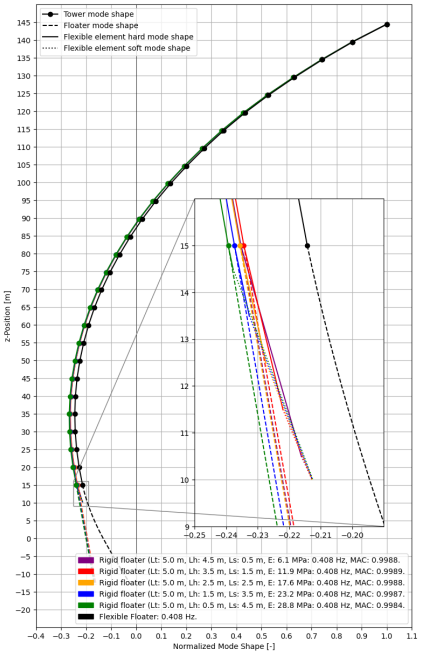

(b) Mode shape variation over hard soft ratio for a total length of 5.0 m.

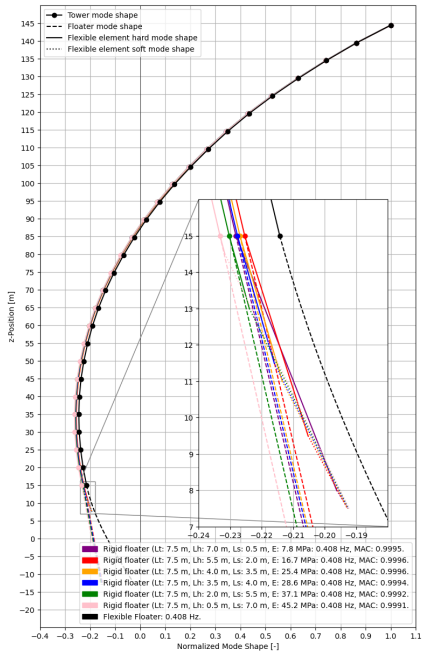

(c) Mode shape variation over hard soft ratio for a total length of 7.5 m.

Figure A.9: Mode shape variation over hard stiff ratio for different total lengths.

A.8 Turbine performance

The most representative turbine performance parameters have been decided to be the platform surge and pitch, as well as mean power production and mean thrust force. The goal of looking at these parameters is to check whether the implementation of the flexible element alters any turbine performance parameters under constant wind. Mean values are chosen in order to neglect any dynamics for now. The plots showing these results are presented in Figure A.10.

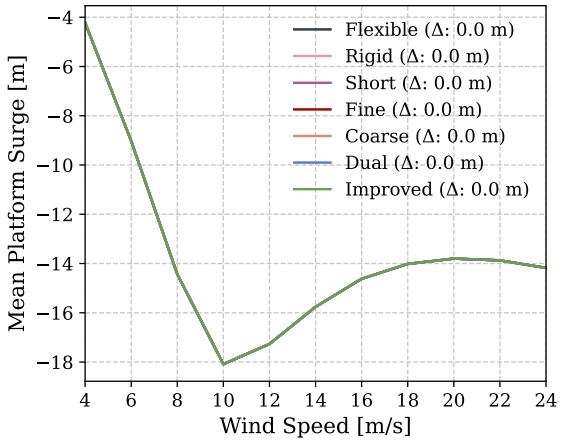

(a) Mean surge of platform over wind speeds from cut-in to cut-out.

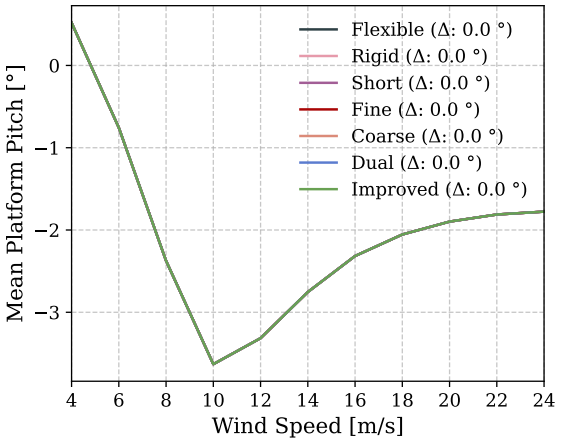

(b) Mean pitch of platform over wind speeds from cut-in to cut-out.

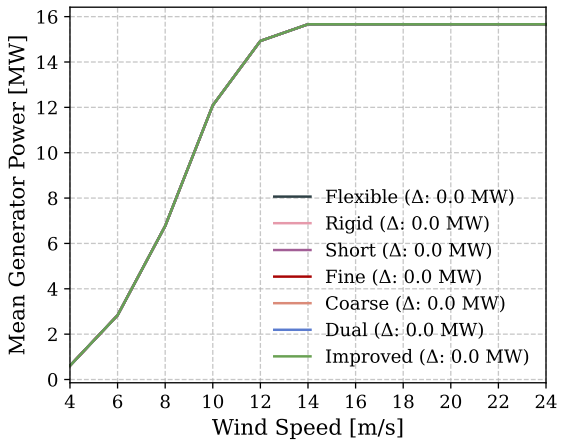

(c) Mean generator power over wind speeds from cut-in to cut-out.

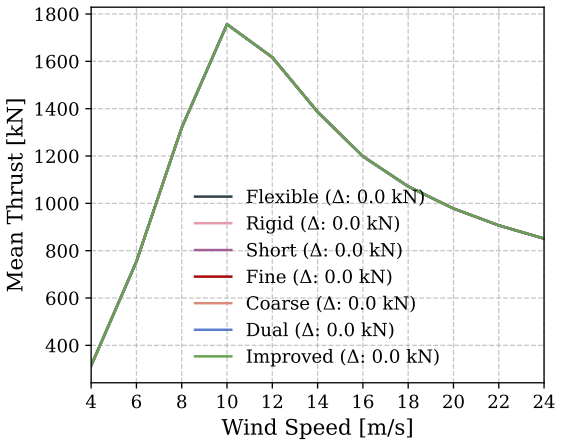

(d) Mean thrust over wind speeds from cut-in to cut-out.

Figure A.10: Mean platform responses and power across wind speeds from cut-in to cut-out. Δ represents the difference between design and flexible floater design as reference.

Only one curve is visible in each plot, as the curves are all overlapping, indicating good agreement. This indication is further investigated by using the flexible design as a reference, and the mean values of the different designs are subtracted from it.

For all designs, even the rigid floater, no deviations from the flexible floater design can be seen. This shows that the flexible element was implemented such that it does not interfere with the turbine performance under constant wind conditions.

A.9 Tower bending at root under turbulent wind

The results of the flexible element design under turbulent wind are compared more closely at the example of a mean wind speed of 20 m/s.

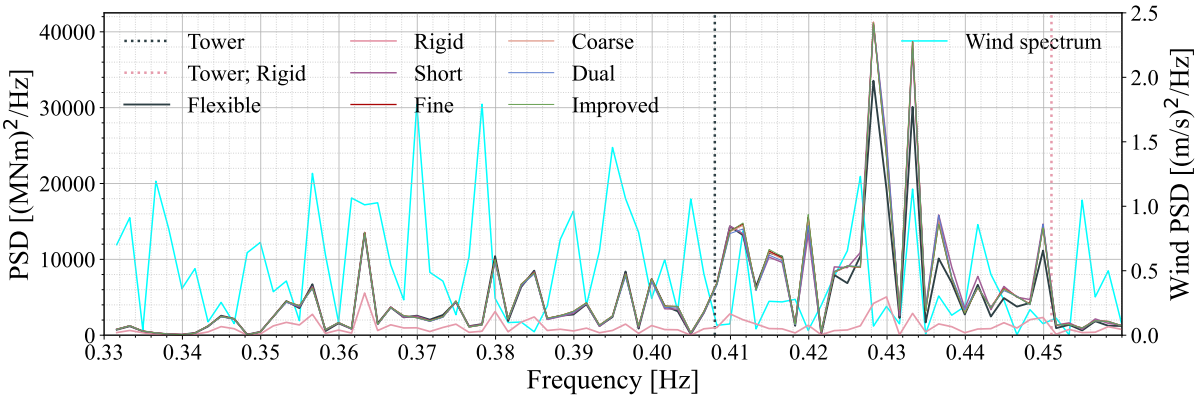

Figure A.11: Spectrum of tower bending for turbulent wind with a mean wind speed of 20 m/s with focus on tower first bending natural frequency, including excitation spectrum.

Figure A.11 shows many peaks with a lot of energy. The rigid floater design's peaks are clearly lower than the flexible floater design ones. This explains the lower overall standard deviation.

The designs using a flexible element follow the peaks of the flexible floater design in general. The wind spectrum has low energy contents at tower natural frequency of the flexible designs. At 0.41 Hz a peak can be seen in the wind spectrum and also excitation of the tower bending, due to the close distance to the tower's first bending natural frequency. All designs using a flexible element match the flexible floater design well for this case.

Two further peaks are observed in the wind spectrum around 0.43 Hz, resulting in peaks of the bending moment. Both these big peaks, as well as the smaller ones around them, are overpredicted by the flexible element designs. This higher excitation explains the bigger standard deviation compared to the flexible floater. The Improved design shows peaks of higher amplitude in the frequency range from 0.41 Hz to 0.42 Hz. These peaks are responsible for the higher standard deviation reported in Table 4.13.

A.10 Tower bending at root under regular waves

The difference in tower bending for the flexible floater design is also visible in the spectrum, where a larger peak at the pitch natural frequency and, in general, at lower frequencies is observed. Being related to the pitch motion, it was decided to investigate the time series and spectrum of the pitch motion, which is shown in Figure A.13.

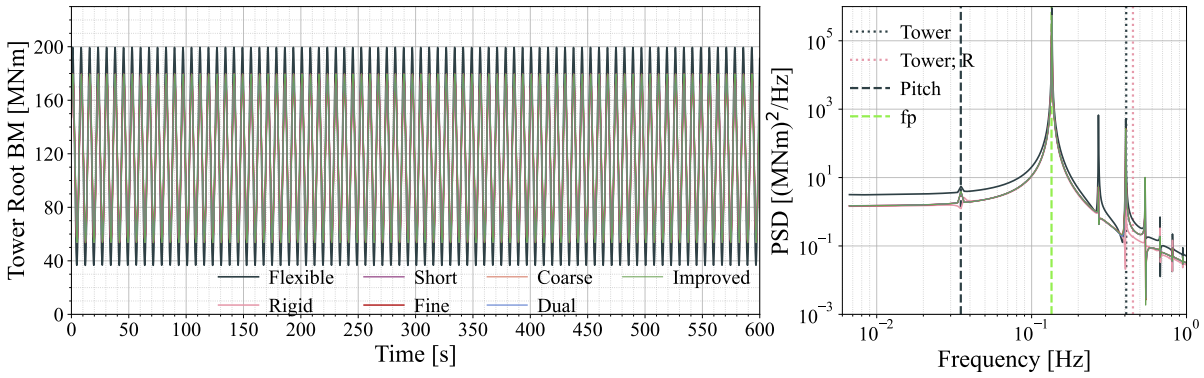

Figure A.12: Time series and spectrum in log-log scale of tower bending at root for regular waves of Hs = 1.84 m and T = 7.44 s.

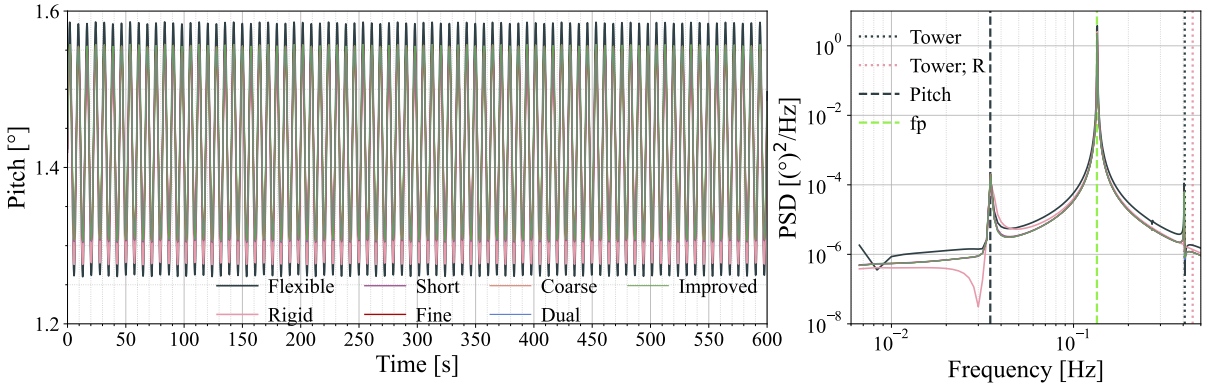

Figure A.13: Time series and spectrum in log-log scale of platform pitch for regular waves of Hs = 1.84 m and T = 7.44 s.

A.11 Tower bending at root under irregular waves

The time series and spectrum of pitch motion of the different designs resulting from an irregular wave with significant wave height of 1.18 m and peak period of 8.31 s are looked at in Figure A.14. A significant difference can be seen in the pitch motion of up to 0.25°. The PSD also shows an increased amount of energy at the pitch natural frequency.

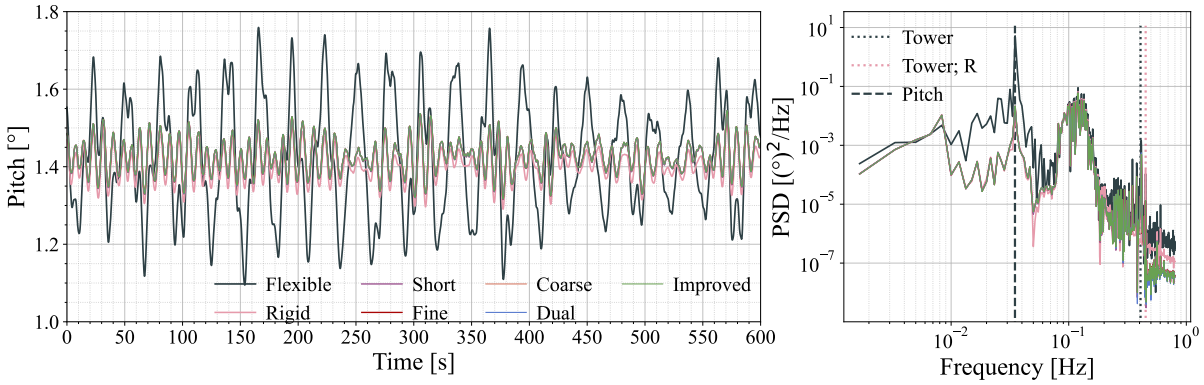

Figure A.14: Time series of platform pitch and corresponding spectrum in log-log scale for irregular waves of Hs = 1.18 m and T = 8.31 s.

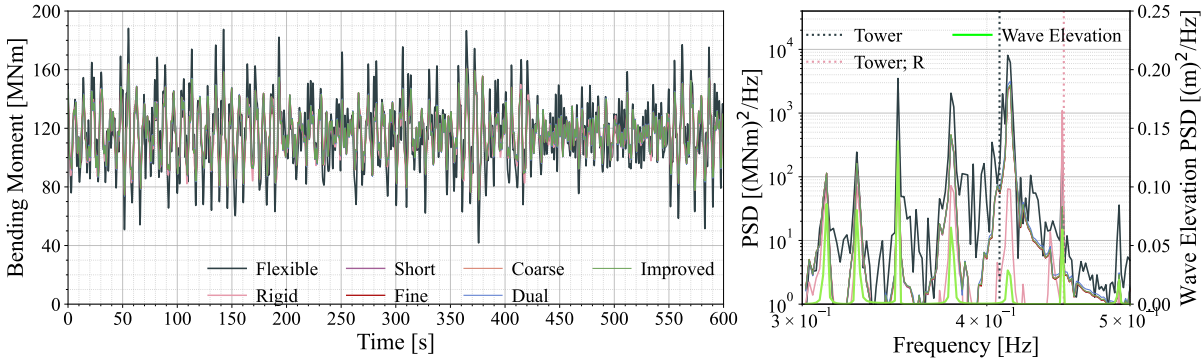

Figure A.15: Time series of platform pitch and corresponding spectrum for irregular waves of Hs = 1.18 m and T = 8.31 s.

The time series of the bending in Figure A.15 shows larger peaks for the flexible design, which is expected to stem from the increased pitch motion. The mean values, on the other hand, appear comparable.

Additionally, to the designs' excitation, the wave spectrum, is shown in Figure A.15. All designs except for the rigid floater design show a clear peak at 0.4125 Hz, which is close to the tower's first bending natural frequency and aligns with a peak of energy content in the wave spectrum. This shows that the flexible element designs successfully capture the excitation at the tower's first bending natural frequency, which is not captured by the rigid floater design. On the other hand, the rigid floater design shows a peak at 0.45 Hz, as both energy contents in the wave exist and the tower's first bending frequency of the rigid floater is close.

The bigger amplitude of the flexible floater design in time domain are also visible as higher peaks in the PSD in Figure A.15. The peaks are visible whenever there is energy content in the wave spectrum. This highlight the source of excitation through the waves. The observation that the flexible floater design shows higher peaks stems from the unintentionally increased excitation in heave motion (subsection 3.1.6).

A.12 Tower bending at root under DLC

The pitch motion is looked at for a mean wind speed of 12 m/s, significant wave height of 1.84 m and wave peak period of 7.44 seconds. The time series and spectrum are shown in Figure A.16.

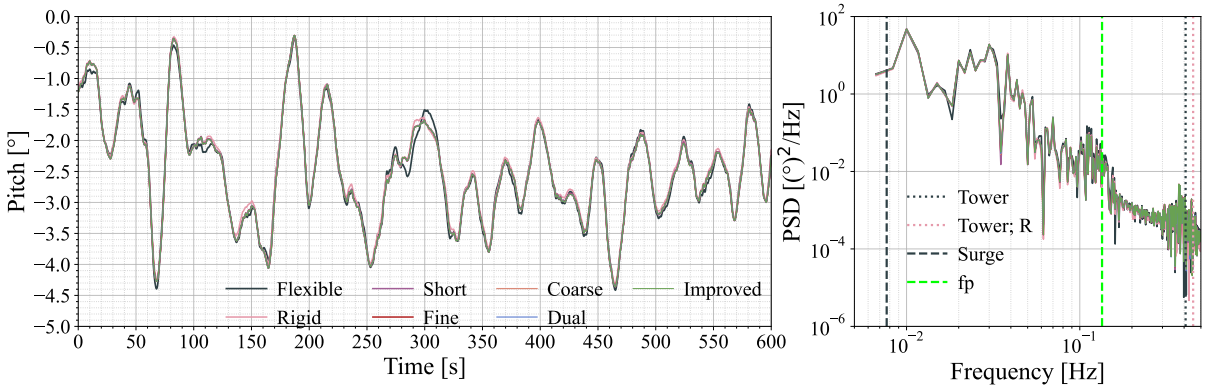

Figure A.16: Time series and spectrum in log-log scale of platform pitch for DLC with mean wind speed of 12 m/s, waves of Hs = 1.18 m and Tp = 8.31 s.

The difference in pitch motion between the different designs, especially the flexible floater design, is significantly less than for the wave-only cases. The spectrum also shows more similarities, indicating more identical excitations of the different designs. This is expected to stem from the additional wind and its introduced aerodynamic damping. This reduces the sensitivity towards wave loads that caused the diverging results between the flexible floater and flexible element designs.

A.13 Tower acceleration at top under constant wind

As an example the time series and spectrum of the tower top acceleration for a constant wind of 10 m/s is shown in Figure A.17.

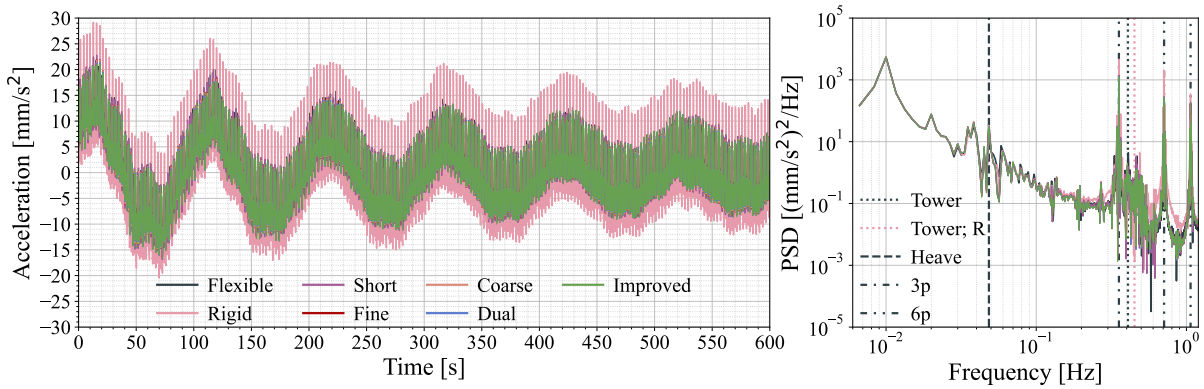

Figure A.17: Time series and spectrum of tower top acceleration for constant wind of 10 m/s.

The standard deviation shown in the spectrum shows higher energy contents for the rigid floater design. As it has already been the case for the bending moment, the rigid floater case shows higher

excitation around 6P, which is closer to the rigid floater tower natural frequency than to the flexible floater towers' natural frequency. The different floater designs appear to match the spectrum of the flexible floater design reasonably well. This is closer investigated by focusing on the spectrum on the range of heave rigid body motion and of the tower first bending natural frequency, as shown in Figure A.18.

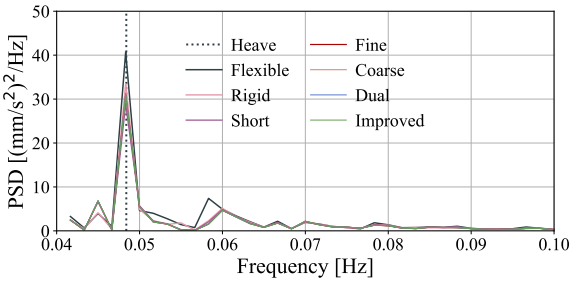

(a) Spectrum of tower top acceleration for constant wind of 10 m/s with focus on heave frequency.

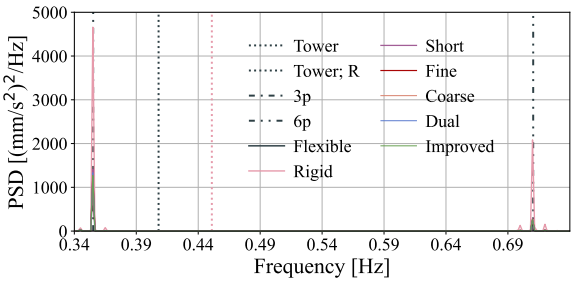

(b) Spectrum of tower top acceleration for constant wind of 10 m/s with focus on tower frequencies.

Figure A.18: Spectrum of tower top acceleration for constant wind of 10 m/s.

The peak at heave freqeuncy in Figure A.18a shows higher energy content for the flexible floater case. Despite the lack of wave excitation, which directly influences the heave motion, the heave motion is more strongly impacted for the flexible floater due to the double counting. Comparing the magnitude of the peak in Figure A.18a to Figure A.17 it can be seen that the overall influence of this peak is negligible, and hence the influence of double counting is not significant.

The spectrum in Figure A.18b around the tower's first bending natural frequency shows two clear peaks. One at 3P, the other one at 6P. All flexible element designs show better agreement with the flexible floater design than the rigid floater design. It is surprising, however, that the energy contents of the rigid floater is higher at both, 3P and 6P even though the tower first bending frequency of the flexible floater design is closer to 3P.

A.14 Tower acceleration at top under turbulent wind

The time series of tower top acceleration and the resulting spectrum are shown in Figure A.19.

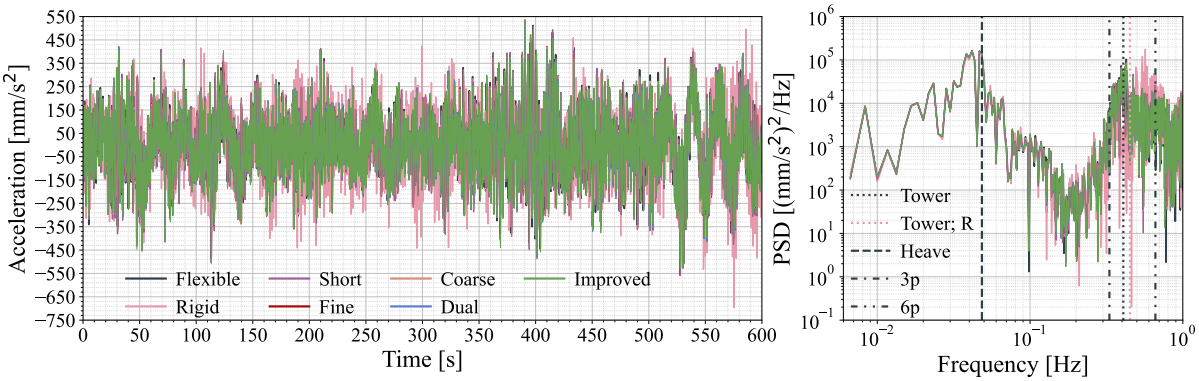

Figure A.19: Time series and spectrum of tower top acceleration for turbulent wind of 10 m/s mean.

No big difference is visible at heave natural frequency, implying that the unintentionally increased response in heave is less significant for turbulent wind conditions. The differences between designs using the flexible element and the rigid floater design at tower natural frequencies are more significant, though, explaining the difference in magnitude seen in the time domain. Figure A.20 focuses on that specific frequency range.

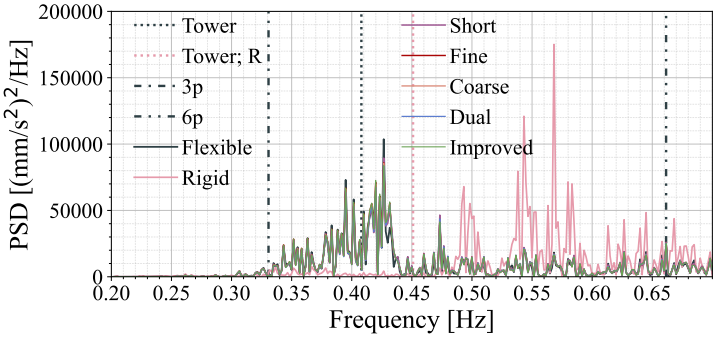

Figure A.20: Spectrum of tower top acceleration for turbulent wind with mean of 10 m/s with focus on heave frequency.

The flexible element designs, as well as the flexible floater design, show a peak around the tower's natural frequency, which is most likely excited by the 3P frequency. The rigid floater shows no significant energy content at this frequency. The peak for the rigid floater is between the rigid floater tower first bending frequency and the 6P frequency, showing that the response depends on excitation frequency and the structures' natural frequency.

A.15 Tower acceleration at top under regular waves

A time series of the tower top acceleration of the different designs is shown in Figure A.21, as well as the corresponding spectrum in log-log scale.

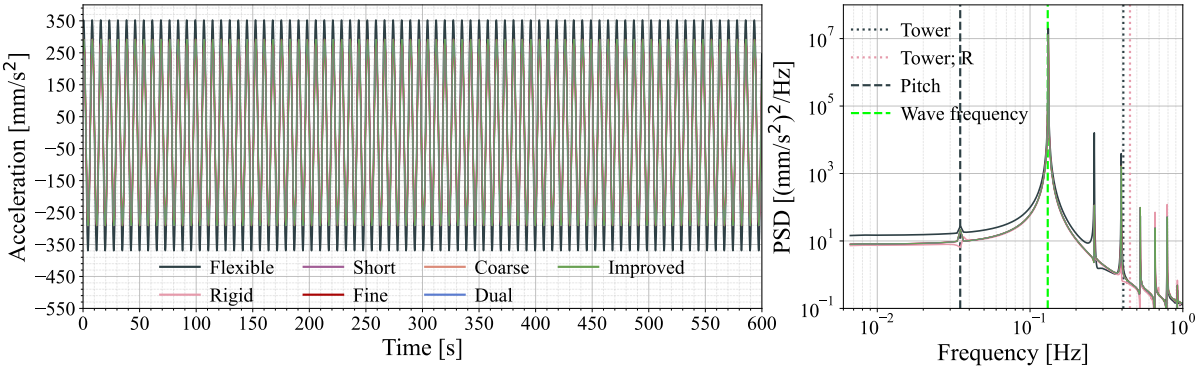

Figure A.21: Time series and spectrum of tower top under regular waves with H = 1.54 m and T = 7.66 s.

The time series in Figure A.21 again indicates the influence of double counting the heave motion for the flexible floater, identified and assed in subsection 3.1.6 and also observed previously. The

increased amplitude of acceleration of the flexible floater seen in time series is also identified by higher energy contents of the flexible floater design at exactly pitch natural period and around it. The spectrum of all designs show peaks at the wave frequency and its multiples, showing that the dependency of tower top acceleration is correctly captured by the flexible element designs. However, due to the mistake in the reference design no conclusions can be drawn on which design is most accurate.

A.16 Tower acceleration at top under irregular waves

The time series of the tower top acceleration for an irregular sea state with Hs = 1.54 m and Tp = 7.66 s in Figure A.22 shows the increased excitation at rigid body motion and in the wave frequency range for the flexible floater design.

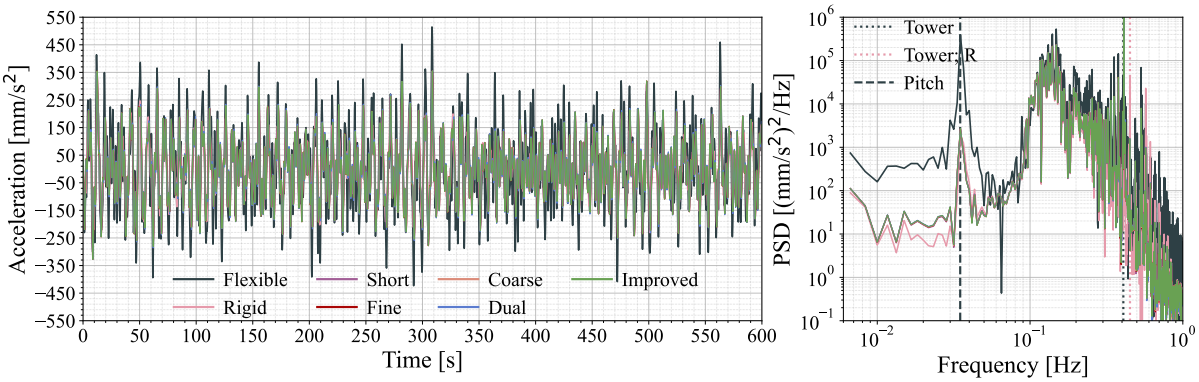

Figure A.22: Time series and spectrum of tower top acceleration for irregular waves with Hs = 1.54 m and Tp = 7.66 s.

The differences at wave frequency range and also around tower first bending natural frequency are highlighted in Figure A.23. Here it can be seen that the flexible floater design shows more energy content at wave excitation frequency. The flexible floater design and flexible element designs show a peak around 0.41 Hz, which is due to wave excitation near the tower first bending frequency of these design.

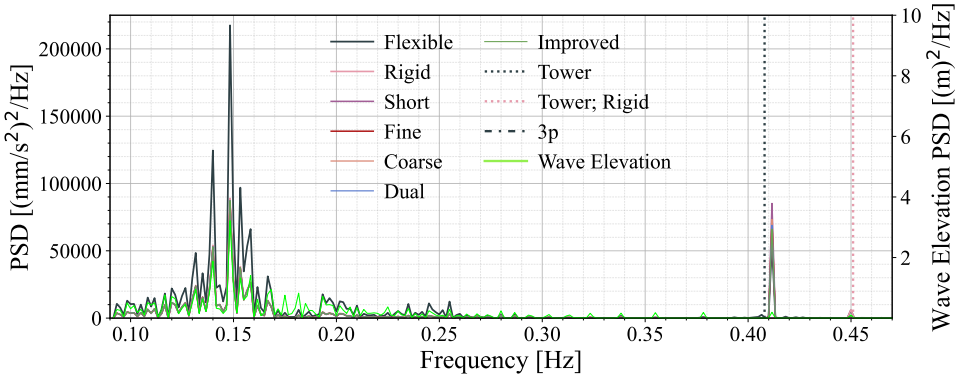

Figure A.23: Spectrum of tower top acceleration for irregular waves with Hs = 1.54 m and Tp = 7.66 s with focus on wave frequency range and tower natural frequency range.

Following tale shows the standard deviation and absolute values over different wind speeds.

Table A.8: Standard deviation of tower top acceleration for irregular waves of the different designs. All values were taken after a transient of 100 seconds.

Hs [m]	**Tp** [s]	**Flexible**	**Rigid**	**Short**	**Fine**	**Coarse**	**Dual**	**Improved**
				[mm/s^2]				
1.10	8.52	109.81	72.83	77.34	77.53	77.46	77.26	77.55
1.18	8.31	120.57	76.65	83.50	83.51	83.63	84.17	83.67
1.32	8.01	127.79	81.83	87.47	87.58	87.54	87.45	87.61
1.54	7.65	153.04	88.48	109.22	109.37	109.63	110.65	109.81
1.84	7.44	182.89	101.14	109.94	110.11	110.11	110.22	110.22
2.19	7.46	216.25	118.61	129.34	129.50	129.53	129.76	129.65
2.60	7.61	282.02	163.22	182.09	182.72	182.61	182.33	182.96
3.06	8.05	323.98	214.12	228.68	228.98	229.01	229.29	229.21
3.62	8.52	399.14	264.56	279.18	279.46	279.49	279.68	279.67
4.03	8.99	407.46	286.83	300.83	301.26	301.15	300.86	301.38
4.52	9.45	450.40	314.88	328.99	329.30	329.27	329.27	329.45

Table A.9: Absolute maximum of tower top acceleration for irregular waves of the different designs. All values were taken after a transient of 100 seconds.

Hs [m]	**Tp** [s]	**Flexible**	**Rigid**	**Short**	**Fine**	**Coarse**	**Dual**	**Improved**
				[mm/s^2]				
1.10	8.52	361.12	211.55	250.26	251.14	250.77	249.54	251.16
1.18	8.31	389.59	221.20	262.02	261.84	262.52	265.54	262.65
1.32	8.01	412.40	218.18	268.67	268.78	268.73	268.55	268.78
1.54	7.65	514.68	277.68	353.23	354.72	354.76	354.93	355.54
1.84	7.44	817.49	334.64	384.62	386.57	386.61	387.61	387.77
2.19	7.46	936.46	394.15	449.82	452.12	452.43	454.66	453.88
2.60	7.61	972.44	603.86	654.28	659.67	656.84	647.07	659.19
3.06	8.05	1050.25	695.79	725.69	727.29	726.39	722.38	726.88
3.62	8.52	1354.89	877.75	943.03	945.65	945.46	945.14	947.08
4.03	8.99	1347.96	964.20	957.54	957.89	958.31	959.55	958.53
4.52	9.45	1634.50	1034.47	1134.18	1132.96	1134.15	1138.24	1133.97

A.17 Tower rotation at top under regular waves

Table A.10: Standard deviation of tower top rotation for regular waves of the different designs. All values were taken after a transient of 100 seconds.

H [m]	**T** [s]	**Flexible**	**Rigid**	**Short**	**Fine**	**Coarse**	**Dual**	**Improved**
				[mm/s^2]				
1.10	8.52	0.15	0.13	0.13	0.13	0.13	0.13	0.13
1.18	8.31	0.16	0.13	0.13	0.13	0.13	0.13	0.13
1.32	8.01	0.17	0.14	0.14	0.14	0.14	0.14	0.14
1.54	7.65	0.17	0.13	0.14	0.14	0.14	0.14	0.14
1.84	7.44	0.18	0.14	0.14	0.14	0.14	0.14	0.14
2.19	7.46	0.21	0.16	0.17	0.17	0.17	0.17	0.17
2.60	7.61	0.29	0.22	0.23	0.23	0.23	0.23	0.23
3.06	8.05	0.39	0.31	0.32	0.32	0.32	0.32	0.32
3.62	8.52	0.50	0.41	0.43	0.42	0.42	0.42	0.42
4.03	8.99	0.55	0.47	0.48	0.47	0.47	0.47	0.47
4.52	9.45	0.57	0.51	0.52	0.52	0.52	0.52	0.52

A.18 Tower rotation at top under irregular waves

Table A.11: Standard deviation of tower top rotation for irregular waves of the different designs. All values were taken after a transient of 100 seconds.

Hs [m]	**Tp** [s]	**Flexible**	**Rigid**	**Short**	**Fine**	**Coarse**	**Dual**	**Improved**
				[mm/s^2]				
1.10	8.52	0.14	0.06	0.06	0.06	0.06	0.06	0.06
1.18	8.31	0.16	0.06	0.06	0.06	0.06	0.06	0.06
1.32	8.01	0.17	0.06	0.06	0.06	0.06	0.06	0.06
1.54	7.65	0.34	0.07	0.07	0.07	0.07	0.07	0.07
1.84	7.44	0.31	0.08	0.08	0.08	0.08	0.08	0.08
2.19	7.46	0.41	0.10	0.10	0.10	0.10	0.10	0.10
2.60	7.61	0.62	0.13	0.13	0.13	0.13	0.13	0.13
3.06	8.05	0.55	0.16	0.17	0.17	0.17	0.17	0.17
3.62	8.52	0.59	0.22	0.23	0.23	0.23	0.23	0.23
4.03	8.99	0.93	0.26	0.27	0.27	0.27	0.27	0.27
4.52	9.45	1.08	0.33	0.34	0.34	0.34	0.33	0.33

A.19 Tower rotation at top under DLC

Table A.12: Standard deviation of tower top rotation for DLCs of the different designs. All values were taken after a transient of 100 seconds.

wsp [m/s]	**Hs** [m]	**T** [s]	**Flexible**	**Rigid**	**Short**	**Fine**	**Coarse**	**Dual**	**Improved**
					[mm/s^2]				
4	1.10	8.52	0.38	0.37	0.38	0.38	0.38	0.38	0.38
6	1.18	8.31	0.63	0.60	0.63	0.63	0.63	0.63	0.63
8	1.32	8.01	0.83	0.80	0.83	0.83	0.83	0.83	0.83
10	1.54	7.65	0.76	0.74	0.76	0.76	0.76	0.76	0.76
12	1.84	7.44	0.88	0.86	0.88	0.88	0.88	0.88	0.88
14	2.19	7.46	0.63	0.61	0.62	0.62	0.62	0.62	0.62
16	2.60	7.61	0.59	0.54	0.56	0.56	0.56	0.56	0.56
18	3.06	8.05	0.50	0.44	0.45	0.46	0.46	0.46	0.46
20	3.62	8.52	0.72	0.64	0.65	0.65	0.65	0.65	0.65